Title
Cosmological Simulations of Self-Interacting Dark Matter: A Study of Gravothermal Collapse in Low-Mass Galaxies

ISBN
9798293825820

Author
Silverman, Maya

Publication Date
2025-09-10

UNIVERSITY OF CALIFORNIA,
IRVINE

Cosmological Simulations of Self-Interacting Dark Matter: A Study of Gravothermal Collapse in Low-Mass Galaxies

DISSERTATION

submitted in partial satisfaction of the requirements
for the degree of

DOCTOR OF PHILOSOPHY

in Physics

by

Maya Silverman

Dissertation Committee:
Professor Manoj Kaplinghat, Chair
Professor Kevork Abazajian
Professor Simona Murgia

2025

DEDICATION

To my family, given and chosen.

TABLE OF CONTENTS

LIST OF FIGURES

LIST OF TABLES

ACKNOWLEDGMENTS

I am incredibly thankful to all who have supported me throughout graduate school.

Thank you to Manoj Kaplinghat, my advisor, for trusting me with some of the most interesting projects, always holding me to high expectations, and helping me achieve my goals. Thank you to the whole research group, especially Tyler Smith, Michael Ryan, and Igor Palubski, for the countless working and debugging sessions. Thank you to my committee members, Kevork Abazajian and Simona Murgia, for your time and support.

Thank you to my East Coast research group. Thank you Mariangela Lisanti, Lina Necib, and Robyn Sanderson for your research mentorship and for the computational resources to run the simulations of my dreams. Thank you Abdelaziz Hussein and Arpit Arora for the many hours of support as I learned to run these simulations.

Thank you to the friends I made along the way. Thank you to Courtney Klein for being the best office mate and bringing life into our window-less office. Thank you Patrick Staudt, Helena Garcia-Escuerdo, Vidya Venkatesan, Patricia Fofie, and all who stopped by my office to say hi and remind me that community exists. Thank you to my acroyoga and climbing community for keeping me sane and teaching me how to fly. Thank you to Aries Magaña and Daniela Gonzalez for always cheering me on.

Most importantly, thank you to my family for your unwavering love and support. Special thank you to my mom for helping me stay grounded, and to my dad for helping me work through all the curve balls.

Chapters 3, 4, and 6 of this thesis are an adaptation of the material as it appears in the Monthly Notices of the Royal Astronomical Society, Volume 518, No. 2, November 2022, used with permission from the Oxford University Press. The coauthors listed in this publication are James S. Bullock, Manoj Kaplinghat, Victor H. Robles, and Mauro Valli. Professor Manoj Kaplinghat supervised the research that forms the basis for this thesis.

Chapters 5, 6, 7, and 8 of this thesis are an adaptation of the material as it will be submitted to the Astrophysical Journal, with expected publication in late 2025-early 2026. The coauthors listed in this publication are Abdelaziz Hussein, Arpit Arora, Manoj Kaplinghat, Mariangela Lisanti, Lina Necib, and Robyn Sanderson. Professor Manoj Kaplinghat supervised the research that forms the basis for this thesis.

Chapter 9 of this thesis is reprint of the material as it appears in the Astronomy Education Journal, Volume 4, No. 1, December 2024, used with permission from The Astronomy Education Journal. The coauthors listed in this publication are Aomawa L. Shields, Jessica N. Howard, Vidya Venkatesan, and Kiana Whitfield. Professor Aomawa L. Shields supervised the research that forms the basis for Chapter 9 of this thesis.

This work was supported in part by the University of California Presidents Pre-Professoriate Fellowship.

VITA

Maya Silverman

EDUCATION

Doctor of Philosophy in Physics and Astronomy **2025**
University of California, Irvine *Irvine, CA*

Master of Science in Physics and Astronomy **2022**
University of California, Irvine *Irvine, CA*

Bachelor of Science in Physics **2019**
University of California, Santa Cruz *Santa Cruz, CA*

RESEARCH EXPERIENCE

Graduate Student Researcher **2021-2025**
University of California, Irvine *Irvine, California*

TEACHING EXPERIENCE

Teaching Assistant **2019-2024**
University of California, Irvine *Irvine, California*

Learning Assistant **2017-2018**
University of California, Santa Cruz *Santa Cruz, California*

FIRST AUTHOR REFEREED JOURNAL PUBLICATIONS

Mergers Matter: Gravothermal Collapse in Low-Mass Halos with Self-Interacting Dark Matter — **In Preparation**
Astrophysical Journal

Rising Stargirls: Benefits of a Creative Arts-Based Approach to Astronomy Education for Middle-School Girls from Underrepresented Groups — **2024**
Astronomy Education Journal

Motivations for a Large Self-Interacting Dark Matter Cross-Section from Milky Way Satellites — **2022**
Monthly Notices of the Royal Astronomical Society

CONTRIBUTING AUTHOR REFEREED JOURNAL PUBLICATIONS

Lessons from HAWC Pulsar Wind Nebulae Observations: The Diffusion Constant is not a Constant; Pulsars Remain the Likeliest Sources of the Anomalous Positron Fraction; Cosmic Rays are Trapped for Long Periods of Time in Pockets of Inefficient Diffusion — **2018**
Stefano Profumo, et al., Physical Review D

Irradiation of Materials with Short, Intense Ion pulses at NDCX-II. — **Aug 2017**
Peter A. Seidl, et al., Laser and Particle Beams

ABSTRACT OF THE DISSERTATION

Cosmological Simulations of Self-Interacting Dark Matter:
A Study of Gravothermal Collapse in Low-Mass Galaxies

By

Maya Silverman

Doctor of Philosophy in Physics

University of California, Irvine, 2025

Professor Manoj Kaplinghat, Chair

Dark matter drives structure formation of the universe from the largest to smallest scales, yet we lack a complete understanding of its fundamental nature. Self-interacting dark matter, a compelling alternative to cold dark matter, is well motivated by particle physics and impacts the density profiles of dark matter halos, particularly at the centers of low-mass ($\sim 10^{10}$ $M_{\odot}$) halos. I use novel cosmological simulations of low-mass halos in SIDM models with moderate ($1-5$ cm^2/g) to large ($30-140$ cm^2/g) self-interaction cross-sections to analyze the gravothermal evolution of subhalos and isolated halos. I find that moderate cross-sections are not sufficient to produce subhalos with core densities large enough to host the densest Milky Way dwarf spheroidal galaxies. This motivates larger cross-sections that induce gravothermal collapse in such systems. When simulating isolated halos with large cross-sections in cosmological environments, I find that while some halos undergo gravothermal collapse, others experience a delay in gravothermal collapse, driven by mergers. How massive and radial a merger is, and also how frequent mergers are affect the time it takes a halo to reach gravothermal collapse. These findings indicate that accounting for mergers is essential when modeling gravothermal collapse in low-mass halos, since they influence constraints on the SIDM parameter space. This work will impact future research on self-interacting dark matter models, allowing for more robust predictions of dark sector models.

Chapter 1

An Introduction to Self-Interacting Dark Matter

Dark Matter (DM) continues to be one of the most prevalent mysteries of the Universe. Since the first indication of the presence of DM, just under a century ago, astrophysicists have made great strides in understanding the abundance and distribution of DM within the Universe and its gravitational effects on visible matter. However, we have yet to converge on the fundamental nature of DM. Assuming DM is a particle (as is all other matter that we know of), its fundamental nature includes the DM particle mass, how strongly DM particles interact with each other (besides via gravity), and how strongly (if at all) DM interacts with the Standard Model (SM)—the portion of matter that we understand far better. My research focuses on an observable combination of the first two quantities: the cross section of self-interactions divided by the DM particle mass: σ/m. The aim this thesis is to explore DM models with varying σ/m—using cosmological simulations to determine if they reproduce astrophysical structures and open the doors to exciting particle physics theories.

1.1 Dark Matter on Cosmological Scales

In 1933 Fritz Zwicky described a kind of *dunkle Materie* that was not visible the way stars, gas, and dust were, but that was necessary to explain the velocity of galaxies within the Coma cluster (Zwicky, 1933, 1937). The existence of this same phenomenon within galaxies was observed rigorously by Vera Rubin in 1970 (Rubin & Ford, 1970). Newtonian dynamics dictates that the circular velocity around a galaxy (modeled as a homogeneous sphere) decreases with radius, r, as $r^{-1/2}$. However, Rubin observed that the circular velocity of gas at the edge of galaxies remained constant with radius (Rubin & Ford, 1970). The difference between expected and observed rotation curves shows that galaxies form in the centers of DM halos (Freeman, 1970). These gravitational impacts allow us to calculate the density of DM in galaxies and galaxy clusters.

The total density of DM in the universe can also be measured, albeit through a slightly more complex calculation, revealing that DM makes up about 25% of the energy density of the universe and baryons (where we use the word "baryon" to describe all visible matter) make up an additional 5% (Planck Collaboration et al., 2016). The remaining 70% of the energy density is attributed to dark energy, an equally intriguing topic that will not be covered in this thesis. Together dark energy, represented by Λ; a model of DM that is non-relativistic, called Cold Dark Matter (CDM); and baryonic matter form the three major components of the standard model of cosmology, ΛCDM.

ΛCDM has been the most successful model at explaining the structure formation of the universe (Bahcall et al., 1999). A key prediction of ΛCDM is hierarchical structure formation—small DM halos collapse first and merge to form more massive halos. Using this model, simulations of structure formation are able to reproduce the large-scale structure of the universe, forming incredibly accurate galaxy clusters linked together via the cosmic web (Springel et al., 2006). ΛCDM also provides an extremely accurate fit to the Cosmic Microwave Background (CMB)—the earliest direct electromagnetic signal we have of the universe. Small temperature variations in the otherwise isotropic CMB show early clustering of matter, highly influenced by DM. From the angular anisotropies one can calculate the matter power spectrum, for which ΛCDM predictions match observations (Tegmark et al., 2004; Percival et al., 2007). While we understand DM well on large-scales, its behavior on small scales (within low-mass galaxies) and at the smallest scales (its particle nature) remains uncertain. Chapter 2 discusses DM within low-mass (defined as $M \sim 10^{10}$ $M_\odot$) galaxies and Section 1.2 discusses DM at the particle level.

1.2 Particle Dark Matter

Although we have yet to measure the DM particle as precisely as we have its cosmological abundance, we can place limits on its interactions and mass. DM interactions with the SM can be constrained by the lack of direct detection. Telescopes have not directly detected DM and particle colliders have not produced DM, limiting the DM to SM interactions to be weak at best. DM interactions with its own type, called self-interactions, can be constrained via gravitational lensing of the DM around galaxy clusters (Meneghetti et al., 2001; Miralda-Escude, 2002). Self-interactions impact the shape and structure of DM particles within cluster halos, as discussed in greater detail in Section 1.3. This structure is observable via strong lensing (Natarajan et al., 2024), which has constrained the self-interaction cross section over DM mass to be ≤ 0.1 cm^2/g (Andrade et al., 2019) at cluster scales. A deeper discussion of self-interaction cross sections and popular models is provided in Section 1.2.2. Finally, the mass of the DM particle can be constrained by the size of the smallest observed DM structures. DM halos have been observed around low-mass galaxies with structures on the scale of a kiloparsec (kpc). Thus, the DM de Broglie wavelength must be smaller than this, corresponding to a mass $\geq 10^{-22}$ eV (Hu et al., 2000).

Throughout this thesis, I focus on the self-interaction cross section divided by the DM particle mass (σ/m). This is an observable quantity because the impact of self-interactions on DM structure is set by the frequency of scattering events. The rate of scattering events is set by:

$$\Gamma = n_{\rm DM}\ \sigma\ v = \rho_{\rm DM}\ \frac{\sigma}{m_{\rm DM}}\ v \tag{1.1}$$

where $n_{\rm DM}$ is the number density of DM particles, σ is the self-interaction cross section, and v is the relative velocity of interacting particles. Number density can be rewritten as $n_{\rm DM} = \rho_{\rm DM}/m_{\rm DM}$ where $\rho_{\rm DM}$ is the density of DM and $m_{\rm DM}$ is the mass of the DM particle. When this is substituted into Equation 1.1, as is done in the right side, one can isolate $\sigma/m_{\rm DM}$ (hereafter referred to as "cross section") as the only quantity that is not observable since density and relative velocity can be inferred via gravity. In the rest of this Section, I will describe two interesting DM models: one which limits the cross section to be zero (called cold dark matter), and one which allows for a non-zero cross section (called self-interacting dark matter).

1.2.1 Cold Dark Matter

Cold dark matter (CDM) is the paradigm DM model that I introduced above as part of the standard cosmology, ΛCDM. CDM is cold, meaning that in the early universe, when structure formation began, CDM particles were moving much slower than the speed of light. CDM is also collisionless, meaning that there are no self-interactions between CDM particles. Throughout this work we frequently compare self-interacting dark matter to CDM to highlight where the CDM model is still a better match to observations, where the two models are indistinguishable, and where self-interacting dark matter is a better match to observations.

1.2.2 Self-Interacting Dark Matter

DM particles that can scatter of one another are referred to as self-interacting dark matter (SIDM; Spergel & Steinhardt 2000; Firmani et al. 2000). Throughout this thesis, self-interactions are assumed to be elastic $2 \rightarrow 2$ scattering events, although inelastic, multi-component SIDM has also been explored (Arkani-Hamed et al., 2009; Schutz & Slatyer, 2015). Since the scattering rate, as described by Equation 1.1, is dependent on the DM density, SIDM largely impacts halo cores, which have large densities, while the outer regions of DM halos remain largely unchanged from CDM. To impact the centers of low-mass galaxies, the cross section must be $\sigma/m \geq 1$ cm^2/g (see e.g. Spergel & Steinhardt 2000; Dave et al. 2001; Colin et al. 2002; Vogelsberger et al. 2012; Rocha et al. 2013; Zavala et al. 2013; Vogelsberger et al. 2014; Fitts et al. 2019).

An SIDM model that impacts low-mass halos and is consistent with constraints from galaxy clusters ($\sigma/m \leq 0.1$ cm^2/g) must be dependent on the relative velocities of interacting particles (Kaplinghat et al., 2016). The relative velocity of interacting particles depends on the mass of the DM halo: lower mass halos have smaller relative velocities than massive halos. Velocity-dependent SIDM (vdSIDM) arises generically in new DM models with dark sectors (Feng et al., 2009; Loeb & Weiner, 2011; Tulin & Yu, 2018).

One of the most well motivated vdSIDM models includes a light mediator through which DM particles interact (Feng et al., 2009; Tulin & Yu, 2018). Such self-interactions are described by the Yukawa potential (Yukawa, 1955):

$$V(r) = \pm \frac{\alpha_\chi}{r} \, e^{-m_\phi r} \tag{1.2}$$

where χ represents the fermionic DM particle, ϕ represents the light mediator, and α_χ is the dark fine structure constant. The differential cross section, using the Born approximation, for Rutherford-like scattering is (Yang & Yu, 2022):

$$\frac{d\sigma}{d\cos\theta} = \frac{\sigma_0 w^4}{2[w^2 + v^2 \sin^2(\theta/2)]^2} \tag{1.3}$$

where w is a characteristic velocity scale below which the cross section becomes isotropic and $\sigma \approx \sigma_0$ (Robertson et al., 2017). When integrated over the angular distribution, the total cross section becomes (Yang & Yu, 2022):

$$\sigma_{\rm tot} = \frac{\sigma_0}{1 + (v/w)^2}. \tag{1.4}$$

In N-body simulations, it is inefficient to frequently scatter DM particles along the forward (and backward) direction where momentum transfer is negligible. A viscosity cross section has bee shown to reproduce the effects of DM while suppressing scattering in the forward direction (Tulin et al., 2013). The viscosity cross section is defined as (Yang & Yu, 2022):

$$\sigma_V = \frac{3}{2}\int d\cos\theta \sin^2\theta \frac{d\sigma}{d\cos\theta}. \tag{1.5}$$

For Rutherford scattering this gives (Yang & Yu, 2022):

$$\sigma_V = \frac{6\sigma_0 w^6}{v^6}\left[\left(2 + \frac{v^2}{w^2}\right)\ln\left(1 + \frac{v^2}{w^2}\right) - \frac{2v^2}{w^2}\right]. \tag{1.6}$$

In the limit where $v \gg w$, $\sigma_V \sim 1/v^4$. Similar cross sections can be calculated for Moller scattering, another well motivated DM with velocity-dependent scattering (Yang & Yu, 2022).

The vdSIDM cross section implemented in this work is an approximation of Rutherford and

Moller scattering that exhibits similar behavior at the small- and large-v limits:

$$\sigma = \frac{\sigma_0}{1 + (v/w)^4}. \tag{1.7}$$

Other simulations have been run with different cross section implementations which are better fit to a variety of particle DM models (Robertson et al., 2017; Kahlhoefer et al., 2013; Fischer et al., 2021, 2022; Yang & Yu, 2022).

In summary, SIDM is a compelling idea because it arises naturally in particle DM models. In the next section we discuss the impacts that self-interactions have on DM halos.

1.3 Density Evolution

On galactic scales, self-interactions allow for heat transfer within DM halos. Where CDM halos have inefficient heat transfer, SIDM halos transfer heat between outer and inner regions. This energy transfer impacts the distribution of DM particles within the halo, causing the density, velocity dispersion, and circular velocity profiles to evolve. The timescale at which these profiles evolve depends on the total number of scattering events which can be approximated by integrating Γ, defined in Equation 1.1, across time. Thus the evolution depends on time, density, cross section, and relative velocity. The next few sections describe three main stages of the halo evolution process, depicted in Figure 1.1. This illustrative example is a cosmological Zoom simulation of a $\sim 10^{10}$ $M_\odot$ halo run with four DM models: CDM (black), $\sigma/m = 30$ cm^2/g (blue), $\sigma/m = 70$ cm^2/g (green), and $\sigma/m = 140$ cm^2/g (red).

As I show in Chapter 7 the evolution of DM halos in cosmological settings is more complex than the stages I outline below. I use these stages to illustrate the idealized evolution, which I discuss in more detail throughout this thesis.

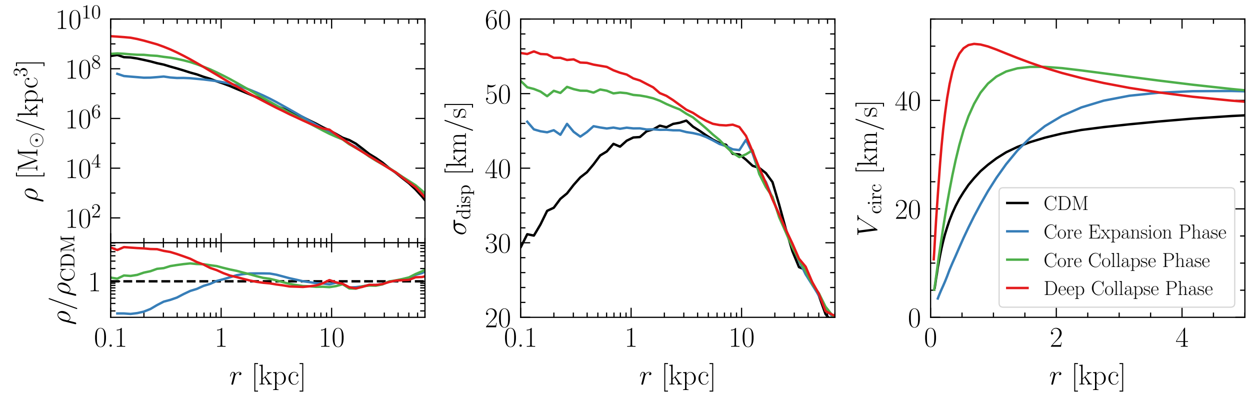

Figure 1.1: Density (left), velocity dispersion (center), and inner circular velocity (right) profiles of halos in four different stages along the SIDM halo evolution process. These profiles are from cosmological Zoom simulations of a $\sim 10^{10}$ M$_\odot$ halo with four DM models: CDM (black), $\sigma/m = 30$ cm^2/g (blue), $\sigma/m = 70$ cm^2/g (green), and $\sigma/m = 140$ cm^2/g (red).

1.3.1 Stage 1: The Navarro-Frenk-White Profile

We start this story at the limit where no self-interaction scattering events have occurred—synonymous with the CDM scenario. DM halos have been well studied within the CDM paradigm, particularly in DM-only scenarios. When in dynamical equilibrium, CDM halos adopt a near universal Navarro-Frenk-White (NFW; Navarro et al. 1997) density profile. The NFW density profile is defined as (Navarro et al., 1996b):

$$\rho(r) = \frac{\rho_s}{\left(\frac{r}{r_s}\right)\left(1+\frac{r}{r_s}\right)^2} \tag{1.8}$$

with scale parameters ρ_s and r_s. At small radii, the density goes as $\rho(r) \propto r^{-1}$, creating a "cuspy" central density that continues to increase in density at smaller radii. At large radii, the density goes as $\rho(r) \propto r^{-3}$. The transition between these slopes is smooth and the scale radius is the radius where $d\log\rho/d\log r = -2$. The left panel of Figure 1.1 shows the NFW density profile in black.

The middle and right panels of Figure 1.1 show the velocity dispersion, $\sigma_{\rm disp}$, and circular velocity, $V_{\rm circ}$ of a CDM halo in black. Velocity dispersion is the variability of a particle's velocity away from the mean velocity at that radius, calculated as $\sigma_{\rm disp} = \sqrt{\sigma_{\rm x}^2 + \sigma_{\rm y}^2 + \sigma_{\rm z}^2}$ where $\sigma_{\rm x}^2 = \langle (V_{\rm x,i} - \langle V_{\rm x} \rangle)^2 \rangle$. Here $V_{\rm x,i}$ is the velocity in the x direction of each particle, i. The velocity dispersion is correlated to the temperature of DM particles as $T = v^2\ m_{\rm DM}$. The NFW velocity dispersion (and thus, temperature) is small in the center, rises to a maximum at moderate radii, and decreases at large radii. Circular velocity is given by Newtonian gravity as $V_{\rm circ} = \sqrt{GM/r}$ where M is the enclosed mass within radius r.

1.3.2 Stage 2: Core Expansion

When DM particles begin to self-scatter, the halo enters the core expansion phase. Let's start with the evolution of the velocity dispersion profile. Now that DM particles scatter, heat is transferred from the hotter region at moderate radii to the colder region at small radii. This heat transfer increases the velocity dispersion of particles at small radii, as shown by the blue line in the middle panel of Figure 1.1. The constant velocity dispersion at small and moderate radii is called an isothermal core.

As the velocity dispersion in the central region increases, particles in this region gain kinetic energy and orbit at larger radii. This decreases the density at small radii. The left panel of Figure 1.1 shows that the density in the core expansion phase, shown by the blue line, has about 1/10 the density of the CDM halo at 0.1 kpc. This decreased central density introduces a "cored" profile that has a constant density core at small radii out to ~ 1 kpc. The size of the core can be defined as the radius where the density falls to 1/2 of the central density. The circular velocity in the core expansion phase has a shallower slope than the CDM halo because of the low-density core.

1.3.3 Stage 3: Gravothermal Collapse

Once the halo has an isothermal core, heat may flow outward as well as inward. However, when heat flows from inner to outer regions of the halo, particles in the inner region lose kinetic energy and orbit at smaller radii. This increases the density at small radii, which increases the temperature of the dense core. With no method to decrease the temperature of the core, this becomes a runaway process: heat goes out, the core loses kinetic energy and condenses to smaller radii, the core density increases along with the core temperature.

The green line in Figure 6.2 depicts a halo that is early in the gravothermal collapse phase such that its central density is equal to the density of the CDM halo at 0.1 kpc. The left panel shows a density profile that has a constant density core that extends to ~ 0.5 kpc. The middle panel shows a velocity dispersion profile that has a slightly negative slope in the inner region. The right panel shows a circular velocity profile that rises steeper than the CDM model, due to the increased mass in the halo core.

Since this is a runaway process, we also show a halo that is deep in the gravothermal collapse phase. The red line depicts a halo that has ~ 5 times the density of the CDM halo at 0.1 kpc. This halo has a constant density core that extends only to ~ 0.2 kpc. The middle panel shows a larger central velocity dispersion with a more negative slope. The right panel shows that the halo deep in the collapse phase has the steepest circular velocity profile within 1 kpc.

The process that I outlined in these three stages can be described by a set of four gravothermal evolution equations that relate density, mass, luminosity, and velocity dispersion (Lynden-Bell & Eggleton, 1980; Balberg et al., 2002; Nishikawa et al., 2020; Essig et al., 2019; Outmezguine et al., 2023; Gad-Nasr et al., 2023). In Chapter 6 I introduce an analytic model for gravothermal collapse that approximates SIDM as a fluid and uses the gravothermal equations to evolve a halo from an initial NFW profile.

1.4 The Role of Cosmological Simulations

Analytic and semi-analytic models, as described in the previous section, are valuable tools for understanding the impact of SIDM on idealized systems. However, it is imperative to validate these models by validating them in more realistic systems. N-body and hydrodynamic simulations are valuable tools for studying the impacts of SIDM on galaxy morphology in realistic cosmological scenarios (Hopkins, 2015; Nadler et al., 2025; Rocha et al., 2013; Robertson et al., 2019; Ragagnin et al., 2024).

While it is computationally unrealistic to model galaxies using realistic mass particles, N-body simulations have been shown to accurately model the evolution of DM halos by sampling their phase space distribution with massive "particles." In the simulations presented in this work, the DM "particle" has a mass of $3 \times 10^3 - 10^4$ $M_\odot$. In this approximation we do not expect to simulate particle scattering at the particle physics level, but rather model the average position and velocity of DM, with each simulated particle tracing the bulk dynamics of an ensemble of microscopic particles.

Chapter 2

Inconsistencies between Simulations and Observations at Small Scales

While ΛCDM successfully explains structure formation at the largest scales (Bahcall et al., 1999; Aghanim et al., 2020; Alam et al., 2021), discrepancies between observed galaxies and predictions from CDM simulations (Flores & Primack, 1994; Moore, 1994; Moore et al., 1999; Klypin et al., 1999) cause tensions at low-mass galaxy scales, i.e. "small scales" (see Sales et al. 2022; Bullock & Boylan-Kolchin 2017 for reviews). I introduce the small-scale tensions that are relevant to this thesis and how SIDM impacts them.

2.1 Too-Big-To-Fail

Milky Way (MW) dwarf spheroidal galaxies (dSphs) play a critical role in testing the SIDM scenario because of the wide range of stellar and dark matter (DM) densities observed in these dSphs (Simon, 2019). The predictions for the brightest of the dSphs have been intensely investigated because of the Too-Big-To-Fail (TBTF) problem (Boylan-Kolchin et al., 2011, 2012).

The TBTF problem initially pointed out that the most massive subhalos in CDM simulations that only simulate DM (and not baryonic matter) (Springel et al., 2008; Diemand et al., 2007), hereafter called DM-only (DMO), were too dense to host the brightest observed dSphs (Boylan-Kolchin et al., 2011, 2012). Since these halos were massive enough to form galaxies yet no galaxies with their high densities were observed, the halos were designated as "too big to fail" at forming galaxies (Bullock & Boylan-Kolchin, 2017). Accounting for baryons in CDM simulations decreases the central density of subhalos (Navarro et al., 1996a; Gelato & Sommer-Larsen, 1999; Read & Gilmore, 2005; Pontzen & Governato, 2012), easing the tension between simulations and observations. However, CDM simulations have yet to produce subhalos with low density cores that have consistent orbits to the corresponding dSphs (Kaplinghat et al., 2019).

SIDM offers another method to decrease the density of subhalos since subhalos in the core expansion phase have lower densities than their CDM counterparts (Rocha et al., 2013; Kamada et al., 2017; Ren et al., 2019; Kaplinghat et al., 2019). However, it has become clear from recent investigations that lowering the densities through core expansion with a constant cross section is not sufficient to explain the diversity in densities measured for the classical and ultra-faint MW dSphs (Valli & Yu, 2018; Read et al., 2018; Kim & Peter, 2021; Ebisu et al., 2022). This has prompted investigation into larger cross section values at velocities relevant for MW dSphs such that some of the subhalos would be in the core collapse phase (Nishikawa et al., 2020; Kaplinghat et al., 2019; Zavala et al., 2019; Kahlhoefer et al., 2019; Sameie et al., 2020b; Correa, 2021; Turner et al., 2021; Jiang et al., 2021b; Sameie et al., 2021).

2.2 The Diversity of Central Density Profiles

Two of the small-scale tensions relate to the central densities of low-mass halos. CDM DMO simulations form halos that follow a cuspy, NFW density profile, consistent with observations of low-mass galaxies at the time (Dubinski & Carlberg, 1991; Navarro et al., 1997). The Core-Cusp problem arose when additional low-mass halos were observed to have constant density cores (Flores & Primack, 1994; Moore et al., 1999). The Diversity problem pointed out that halos of the same mass showed an even larger diversity in the inferred density profiles: some cored, some cuspy, and some with even steeper central density profiles than NFW (Kuzio de Naray & McGaugh, 2014; Oman et al., 2015; Relatores et al., 2019; Santos-Santos et al., 2020; Hayashi et al., 2020).

Baryonic feedback has been shown to create cored profiles in CDM halos, potentially alleviating these tensions (Governato et al., 2010; Oh et al., 2011; Oñorbe et al., 2015; Chan et al., 2015; Wetzel et al., 2016; Santos-Santos et al., 2018; Jackson et al., 2024; Koudmani et al., 2025). However, whether feedback can explain the full observed diversity remains in question (Sawala et al., 2010, 2011; Guo et al., 2011). Recently, Klein et al. (2025) point out that galaxies in the FIREbox simulation (Feldmann et al., 2023) do not reproduce the shapes of observed low-mass galaxies in the Galaxy and Mass Assembly survey (Driver et al., 2011) using the baryonic feedback implemented by the Feedback In Realistic Environments (FIRE) project. An additional point to consider is the possible deviation of observed rotation curves from true circular velocity and density profiles, which Sands et al. (2024) highlight in FIRE simulations.

SIDM has emerged as a compelling alternative to CDM because it naturally produces cored profiles without baryonic feedback (Spergel & Steinhardt, 2000; Dave et al., 2001; Colin et al., 2002; Vogelsberger et al., 2012; Rocha et al., 2013; Zavala et al., 2013; Vogelsberger et al., 2014; Fitts et al., 2019). It is well established that a cross section greater than about

1 cm^2/g is required in order to impact halo densities in galaxies (see e.g. Spergel & Steinhardt 2000; Dave et al. 2001; Colin et al. 2002; Vogelsberger et al. 2012; Rocha et al. 2013; Zavala et al. 2013; Vogelsberger et al. 2014; Fitts et al. 2019). When looking at spiral galaxies from the Spitzer Photometry and Accurate Rotation Curves (SPARC) data set (Lelli et al., 2016), Ren et al. (2019) find that SIDM can explain the diversity in rotation curves for $\sigma/m > 3$ cm^2/g utilizing the scatter in the concentration-mass relation for halos and the coupling between baryons and dark matter due to thermalization (Kamada et al., 2017). Using N-body simulations, Sameie et al. (2020a) show that low-mass subhalos in a MW-like potential form cored profiles with $\sigma/m = 1$, 3, and 5 cm^2/g , with core density decreasing with cross section. Robles et al. (2017) come to a similar conclusion for isolated low-mass halos using a hydrodynamic simulation with $\sigma/m = 10$ cm^2/g . However, the full range of observed central densities has not been reproduced, which motivates studying the impact of large cross sections ($\sim 10 - 100$ cm^2/g) on halo evolution in low-mass halos (Valli & Yu, 2018; Slone et al., 2023; Zhang et al., 2024).

2.3 Missing Satellites

The Missing Satellites problem initially highlighted that the number of simulated subhalos far outnumbered observed satellite galaxies of the MW (Kauffmann et al., 1993; Klypin et al., 1999; Moore et al., 1999; D'Onghia & Burkert, 2003). At the time, simulations only included CDM DMO models. Since then, more developed simulations that include baryonic matter as well as novel DM models have been studied (Samuel et al., 2019; Libeskind et al., 2020; Grand et al., 2021). Observational tools have also improved, allowing old, faint, and low surface brightness satellites to be found (McConnachie, 2012; Fritz et al., 2018; Drlica-Wagner et al., 2015, 2020). With these advancements, the Missing Satellites problem has almost been turned on its head: potentially simulating far fewer subhalos than there are observed satellite galaxies (Kim et al., 2018; Graus et al., 2019; Kelley et al., 2019). Thus, it seems that the Missing Satellites problem has drastically changed since its original assessment (Kim & Peter, 2021).

Chapter 3

Simulations of the Milky Way with Moderate Cross Sections

In this Chapter, I introduce two high-resolution zoom-in N-body simulations of Milky Way-mass galaxies and their subhalos. These simulations are run using SIDM with moderate cross sections of 1 cm^2/g (S1) and 5 cm^2/g (S5). The gravitational potential of a baryonic disk and bulge matched to the Milky Way is included, which is critical for getting accurate predictions of the Milky Way and its subhalos. I show that the host halo density profiles in the CDM and SIDM models are comparable to within 30% in regions in which subhalos orbit (> 10 kpc). The density profiles of subhalos are comparable between SIDM models, although those that come close to the host halo (< 50 kpc) are slightly less massive in the S5 simulation. I find no significant difference in the $V_{\max}$ and $r_{\max}$ values of the subhalos in CDM, S1, and S5 simulations. To study the impact of subhalo-host halo SIDM interactions, I calculate the mass lost due to such interactions, and find that subhalos lose, on average, 2% (9%) of their mass in the S1 (S5) simulation.

This chapter is based on research published in the Monthly Notices of the Royal Astronomical

Society. I use "we" throughout to acknowledge the joint contributions of myself (first author) and my co-authors.

3.1 Simulation Methodology

We analyze data from two SIDM cosmological Milky Way mass ($M_{\rm vir} = 10^{12}$ M$_\odot$) halo simulations: one with a self-interaction cross section over dark matter particle mass of $\sigma/m = 1$ cm^2/g (S1), and the other with $\sigma/m = 5$ cm^2/g (S5). In addition, we compare both SIDM models with a corresponding MW halo in a CDM cosmology. The S1 simulation was previously introduced and explored in Robles et al. (2019). The S5 simulation is the same halo as in S1 but with higher cross section. Here we provide the summary of our simulated halos (see Robles et al. (2019) for the simulation details). The MW halos were simulated using the zoom-in technique (Katz & White, 1993; Onorbe et al., 2013) so that the high-resolution region (with dark matter particle mass $m_{\rm DM} \approx 3 \times 10^4$ M$_\odot$ and physical Plummer equivalent softening $\epsilon = 37$ pc) encloses a single MW mass halo within ~ 3 Mpc from the selected halo at $z = 0$. The high-resolution region is part of a cosmological box of length 50 Mpc h^{-1} in a Plank cosmology (Planck Collaboration et al., 2016) with $h = 0.675$, $\Omega_m = 0.3121$, $\Omega_b = 0.0488$, and $\Omega_\Lambda = 0.6879$. The simulations are run using `GIZMO`[1] (Hopkins, 2015), and we use the SIDM implementation in Rocha et al. (2013); Robles et al. (2019). Halos are identified using `Rockstar` (Behroozi et al., 2013) and we use the halo catalogs that we build from the merger trees using `consistent-trees` (Behroozi et al., 2013).

Simulations start at $z = 125$ from the same initial conditions generated using MUSIC (Hahn & Abel, 2011). The SIDM runs are indistinguishable until $z = 3$. Dark matter self interactions are modeled as velocity independent, isotropic, hard-sphere scattering with cross section σ. Velocity dependence and angular dependence likely have measurable effects on

[1] `https://www.tapir.caltech.edu/~phopkins/Site/GIZMO`

halo and subhalo evolution, which is an interesting direction to explore in the future.

One of the missing elements in the predictions of MW dSphs is the impact of the MW's stellar disk on the dSph densities. For highly radial orbits, the disk reduces the internal densities of the subhalos (Brooks & Zolotov, 2014; Kelley et al., 2019) and it brings the cold, collisionless DM (CDM) predictions for the census of the satellites closer to what is observed (Graus et al., 2019). The effects of the disk are amplified for SIDM subhalos with large cores (Sameie et al., 2018), such that a detailed comparison of SIDM models to the observed satellite densities and census is not possible without including the disk. Another missing element has been the lack of a detailed prediction for the ultra-faint satellites because their internal densities are measured at radii of $\sim$ 100 pc or smaller, which is difficult to resolve.

Accounting for the baryonic matter is necessary to infer more realistic predictions for MW satellites. In this work, we account for the gravitational effects of baryonic matter by including disk and bulge potentials following the semi-analytical model in Kelley et al. (2019), initialized at $z = 3$. Hereafter, we will only present results for the CDM and SIDM simulations that include the contribution of the baryonic potentials (unless specified otherwise).

The initial conditions for the simulations, including the baryonic potentials, are described in Kelley et al. (2019) for CDM, and Robles et al. (2019) for SIDM. For the S5 simulation that we introduce in this work, we use the same initial condition as S1 which includes the baryonic potential at $z = 3$. The bulge component is modeled by a Hernquist sphere. The disk and bulge (which we will refer to as just "disk" throughout this paper) are set to agree with observations at $z = 0$. The disk is composed of stars and gas with a stellar radius of $R_* = 2.5$ kpc, stellar height $h_* = 0.35$ kpc, stellar mass $M_* = 4.1 \times 10^{10}$ $M_\odot$, gas radius $R_{\rm gas} = 7$ kpc, gas height $h_{\rm gas} = 0.084$ kpc, and gas mass $M_{\rm gas} = 1.86 \times 10^{10}$ $M_\odot$ at $z = 0$.

This work is focused on one simulated halo with the baryonic disk and bulge tuned to the

MW, so running different halo masses would be useful. The effect of the baryonic potential on host halo shape (Vargya et al., 2021) and star formation rate (Sameie et al., 2021) have been explored in SIDM. In a CDM scenario, Garrison-Kimmel et al. (2017) find that subhalo mass fraction and radial distribution are minimally effected by disk radius, thickness, and shape. Increasing the disk mass by a factor of two only decreases the number of subhalos within 50 kpc by about 20% (Garrison-Kimmel et al., 2017). While this effect may be slightly amplified in an SIDM scenario, we don't expect disk parameters to effect our results, unless disk mass is varied by a factor of at least two.

3.2 Milky Way-Mass Host Halo

In this section we discuss the effects that SIDM has on the host halo. We have chosen to focus on the particle distribution within the host halo and the distribution of subhalo velocities with respect to the host halo. In Section 4.1 we also discuss the subhalo distribution within the host halo compared to observations of MW satellite galaxies.

3.2.1 Density Profile

First, we compare the density profile (ρ), the circular velocity ($V_{\rm circ}$), and velocity dispersion ($\sigma_{\rm disp}$) of the host halo in the CDM and SIDM simulations. We use particle data from each simulation to calculate the current time ($z = 0$) profiles. In Section 3.2.2, we additionally solve for the Navarro-Frenk-White (NFW) (Navarro et al., 1997) density profiles at very early times ($z = 3$) and at $z = 0$. We find that there is negligible difference between the NFW early and late time profile and the particle density profile in the region $r > 10$ kpc. Since the subhalos we investigate in this paper always stay outside 10 kpc, we use the $z = 0$ particle density of the host halo throughout this work.

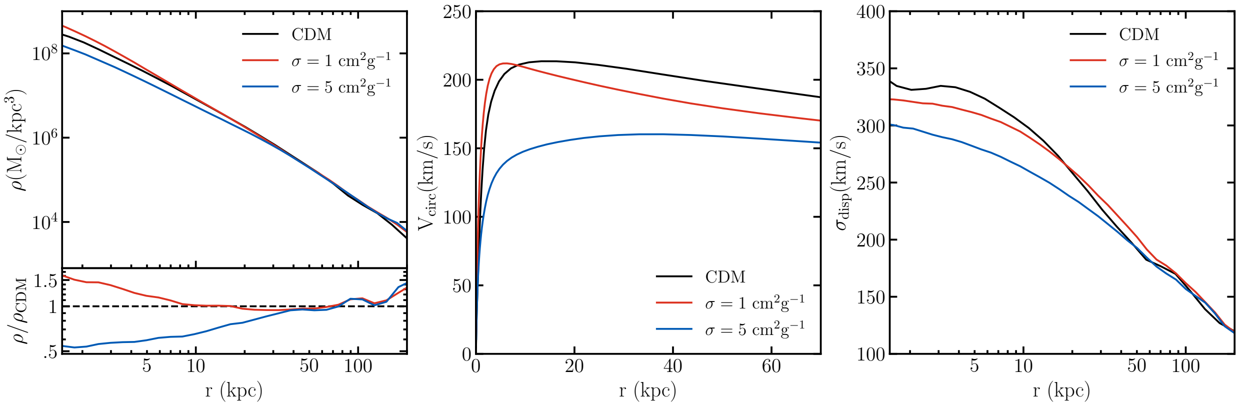

Figure 3.1: Host halo properties at $z = 0$ for CDM (black), $\sigma/m = 1$ cm^2/g (red), and $\sigma/m = 5$ cm^2/g (blue). (*Left*) Dark matter density profile. All three models show similar densities outside 20 kpc and are cuspy in the inner regions. (*Middle*) Dark matter circular velocity profile. The difference in maximum circular velocity attests to the lower central density in S5. (*Right*) Dark mater velocity dispersion. S1 and S5 have thermalized central regions, while CDM rises within the stellar and gas disk ($R_* = 2.5$ kpc at z=0). S5 has a lower density and velocity dispersion within about 20 kpc because of the thermalization process expected with SIDM.

Figure 3.1 shows the DM density profiles of the host halo in CDM, S1, and S5 in the left panel, the circular velocity profiles in the center panel, and the velocity dispersion profiles in the right panel. Density and velocity dispersion are calculated within 40 logarithmically spaced radial bins. Velocity dispersion is calculated as $\sigma_{\rm disp} = \sqrt{\sigma_x^2 + \sigma_y^2 + \sigma_z^2}$ where $\sigma_x^2 = \langle (V_{x,i} - \langle V_x \rangle)^2 \rangle$. Here $V_{x,i}$ is the velocity in the x direction of each particle, i, within the radial range. Circular velocity is given by Newtonian gravity as $\sqrt{GM/r}$ where M is the enclosed mass within radius r.

Both SIDM models follow CDM to $\sim 40\%$ in density outside 10 kpc and $\sim 30\%$ outside 20 kpc, indicating that objects orbiting the host halo in all three simulations spend a majority of their time in areas of similar density. The density profiles of the host halos in all three models have small cores and are rather cuspy. At $r = 1$ kpc, S5 is ~ 0.5 times as dense as CDM, while S1 is ~ 1.5 times as dense as CDM.

In the absence of a baryonic disk, SIDM host halos have been shown to have larger cores and lower central densities (Nadler et al., 2020a). Due to the dependence of the DM density on the baryon gravitational potential (Kaplinghat et al., 2014), SIDM halos are expected to have smaller cores and higher densities when taking the baryonic disk into account. A comparison of S1 and CDM with and without the effects of a baryonic disk is given by Robles et al. (2019).

The middle panel of Figure 3.1 shows that the maximum circular velocity of host halos in CDM and S1 are both just over 200 km/s, while the maximum circular velocity of the host halo in S5 is around 150 km/s. This difference is due to the low central density in the S5 host halo with respect to S1 and CDM.

The right panel of Figure 3.1 shows the velocity dispersion. In the CDM model, the velocity dispersion peaks at about 4 kpc and rises steeply within ~ 2.5 kpc, which corresponds to the radius of the stellar and gas disk. When DM self-interactions are included, velocity dispersion corresponds to temperature. The about constant velocity dispersions at the center of both SIDM models indicate that these regions are isothermal. The hot core and colder outer region leads to gravothermal core collapse in the SIDM host halos, as also noted by Elbert et al. (2018) and Robles et al. (2019). S5 has a slightly lower velocity dispersion at the center of the halo than S1, because with a larger interaction rate, heat transfers to the outer parts of the halo more efficiently.

Thus, in the regions in which subhalos orbit, the host halo density profiles in the CDM, S1, and S5 models are comparable to within 30%. The 50% difference in the host central densities leads to slightly different circular velocity profiles in all three models. The host halos in both SIDM simulations are isothermal, while the CDM halo is not.

3.2.2 Time Dependent Density Profile

While the density profile of the host halo does evolve with time, we use the NFW profiles at early ($z = 3$) and late ($z = 0$) times to show that the change is negligible in regions of highest interest. The subhalos that we examine throughout this paper, as well as most other subhalos in the simulations, do not ever come within 10 kpc of the center of the host halo. Thus, the region of interest is outside 10 kpc.

Figure 3.2 shows the density profiles of the host halo in our S1 (red) and S5 (blue) simulations. Particle data is used to calculate these profiles at $z = 0$ (solid), and parameters from the merger trees are used to estimate NFW density profiles at $z = 0$ (dashed) and $z = 3$ (dotted).

Comparing the density profiles at different redshifts and at 10 kpc, the NFW approximation of the S5 halo has become more dense by about a factor of 1/2, while the S1 halo has remained at the same density. Outside 10 kpc, this difference in the S5 halo decreases to a negligible amount.

Thus, we conclude that the S1 and S5 host halo density profiles throughout all time can be reasonably approximated by their particle density profiles at $z = 0$.

3.2.3 Subhalo Velocity Distribution

To get a better idea of how the host halo affects orbiting subhalos, we look at subhalo characteristics before and at accretion. We use the maximum circular velocity at accretion, $V_{\rm acc}$ and the peak circular velocity, $V_{\rm peak}$ as indicators of mass at these times.

We define accretion as the earliest time at which a subhalo is within the virial radius of the host halo. If a subhalo never comes within $R_{\rm vir}$, accretion is taken to be at $z = 0$. This is a valid approximation because we only look at subhalos that are currently within 300 kpc of

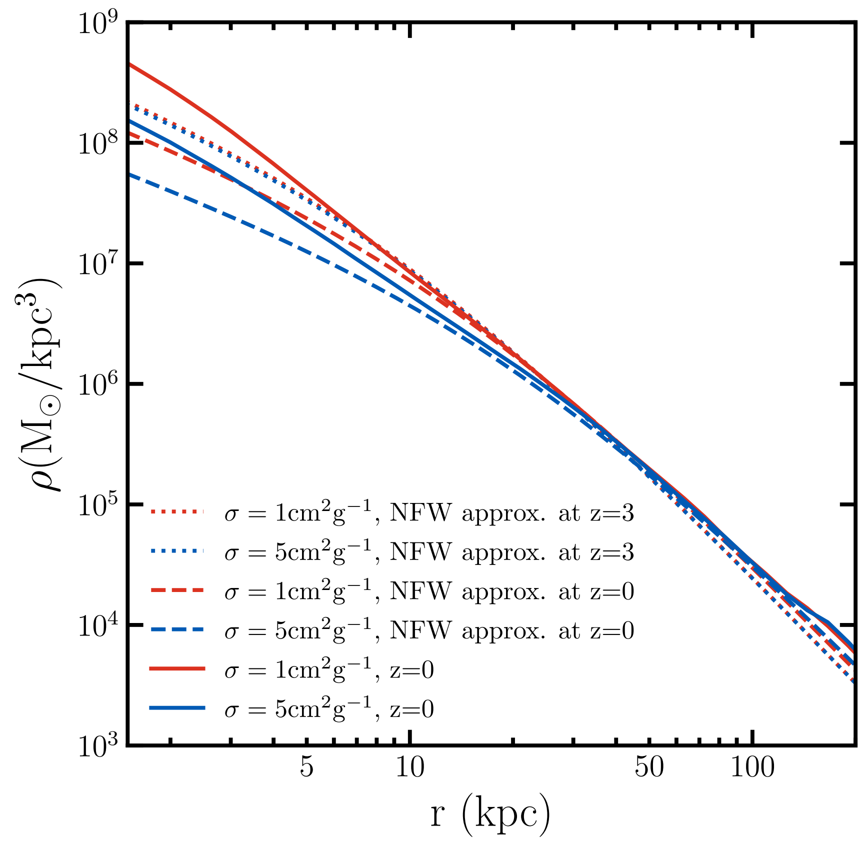

Figure 3.2: Host halo dark matter density. The density is calculated using the particle data, as described in Section 3.2 (solid) and by calculating the approximate NFW profile (dashed). NFW profiles are calculated at $z = 0$ (dashed) and z=3 (dotted) for $\sigma/m = 1$ cm^2/g (red), and $\sigma/m = 5$ cm^2/g (blue).

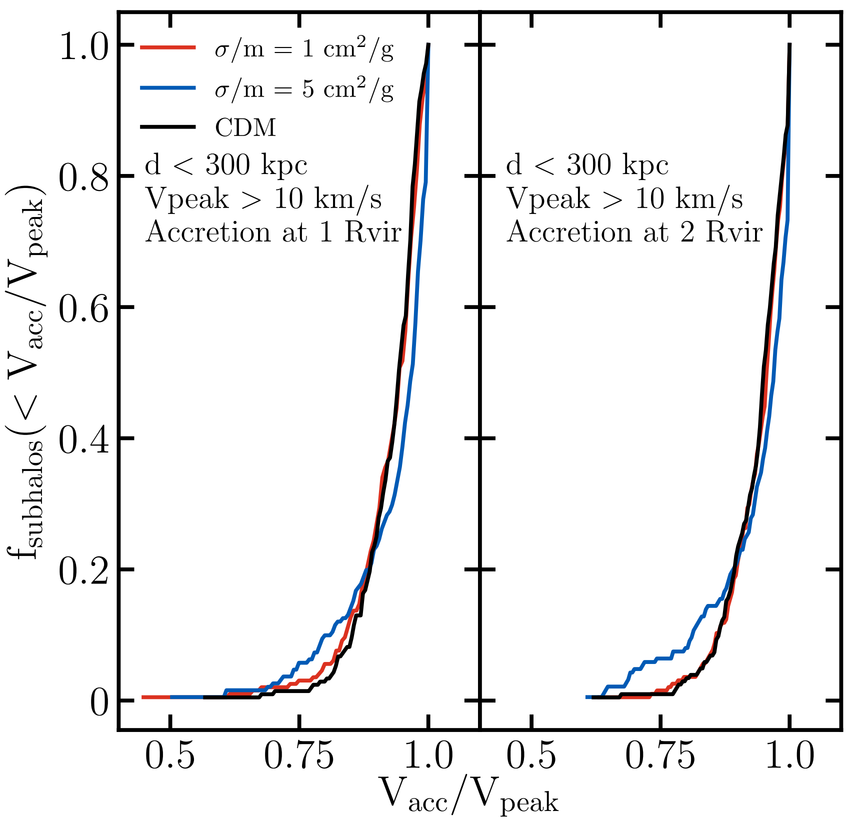

Figure 3.3: Normalized cumulative fraction of the maximum circular velocity at accretion divided by the largest maximum circular velocity of the subhalo before accretion. $f_{\rm subhalos}(< V_{\rm acc}/V_{\rm peak}) = N_{\rm subhalos}(< V_{\rm acc}/V_{\rm peak})/N_{\rm total}$. The left panel shows the histogram when accretion is taken to be at 1 $R_{\rm vir}$ and the right panel shows the histogram when accretion is taken to be at 2 $R_{\rm vir}$.

the host halo, which has a virial radius of about 270 kpc.

$V_{\rm peak}$ is often defined as the largest maximum circular velocity over all time and corresponds closely with subhalo mass. Self interactions as well as tidal stripping cause halos to lose mass while they are inside the virial radius of the host halo, so $V_{\rm peak}$ occurs before the subhalo has been accreted (except for some cases with major mergers). To correct for nonphysical jumps in the $V_{\rm max}$ data, we define $V_{\rm peak}$ as the largest $V_{\rm max}$ before accretion.

The ratio of $V_{\rm acc}$ and $V_{\rm peak}$ describes the change in mass that subhalos experience before entering the host halo.

The left panel of Figure 3.3 shows a cumulative, normalized histogram of the ratio of $V_{\rm acc}$ and $V_{\rm peak}$ for subhalos with $V_{\rm peak} > 10$ km/s . The tail at the low end of $V_{\rm acc}/V_{\rm peak}$ means that some subhalos in both SIDM simulations are losing as much as 50% of their maximum mass before falling into the host halo. S5 has a larger fraction of subhalos that lie in the region $0.6 \leq V_{\rm acc}/V_{\rm peak} \leq 0.8$, but there is no noticeable difference between S1 and S5 below 0.6.

Similarly, Nadler et al. (2020a) observed a trend in the fraction of subhalos at the low end of the $V_{\rm acc}/V_{\rm peak}$ tail that is dependent on self-interaction velocity scale: larger velocity scales lead to a more prominent tail.

At first glance, it seems this trend may be explained by mass loss due to self interactions in the dense region outside the virial radius out to the splashback radius (Diemer & Kravtsov, 2014). For typical MW mass halos, the splashback radius is located at about 1.5 times the virial radius (Adhikari et al., 2014; More et al., 2015). To check this theory, the right panel of Figure 3.3 shows a cumulative, normalized histogram of the ratio of $V_{\rm acc}$ and $V_{\rm peak}$, with accretion defined to be at 2 $R_{\rm vir}$, rather than 1 $R_{\rm vir}$. While the very low end tail $V_{\rm acc}/V_{\rm peak} < 0.6$ disappears in this case, we still see a larger fraction of S5 subhalos in the region $0.6 \leq V_{\rm acc}/V_{\rm peak} \leq 0.8$. We see similar results when looking at subhalos with

$V_{\rm peak} > 4.5$ km/s and $V_{\rm peak} > 15$ km/s .

This is in contrast to what Nadler et al. (2020a) report. They find the difference between SIDM and CDM to decrease when defining accretion at larger radii, while we find that the difference is slightly amplified.

While we do observe that subhalos in the S5 simulation lose more mass than those in the S1 and CDM simulations before accretion, the mass loss we observe is not due to self interactions between host halo and subhalo particles at the infall velocity scale. We are unclear why we find different results than Nadler et al. (2020a), which motivates further discussion. The different results may be due to simulation implementation, a difference in host halo mass, or a difference in cross section (we use a spherically averaged cross section while they use a differential cross section).

Thus, we find a larger normalized fraction of subhalos in the S5 simulation losing more mass before falling into the host halo (defined by $V_{\rm acc}/V_{\rm peak}$). Although this has previously been explained by interactions with the splashback radius, we do not find that this phenomenon decreases when probing mass loss before subhalos reach the splashback radius.

3.3 Low-Mass Subhalos

In this section we discuss the effects that SIDM has on the subhalos within the host halo. We have chosen to look at two quantities: the subhalo density profiles and subhalo $V_{\rm max}$ and $r_{\rm max}$ values. We also compare subhalo circular velocity profiles to MW satellites in Section 4.2.

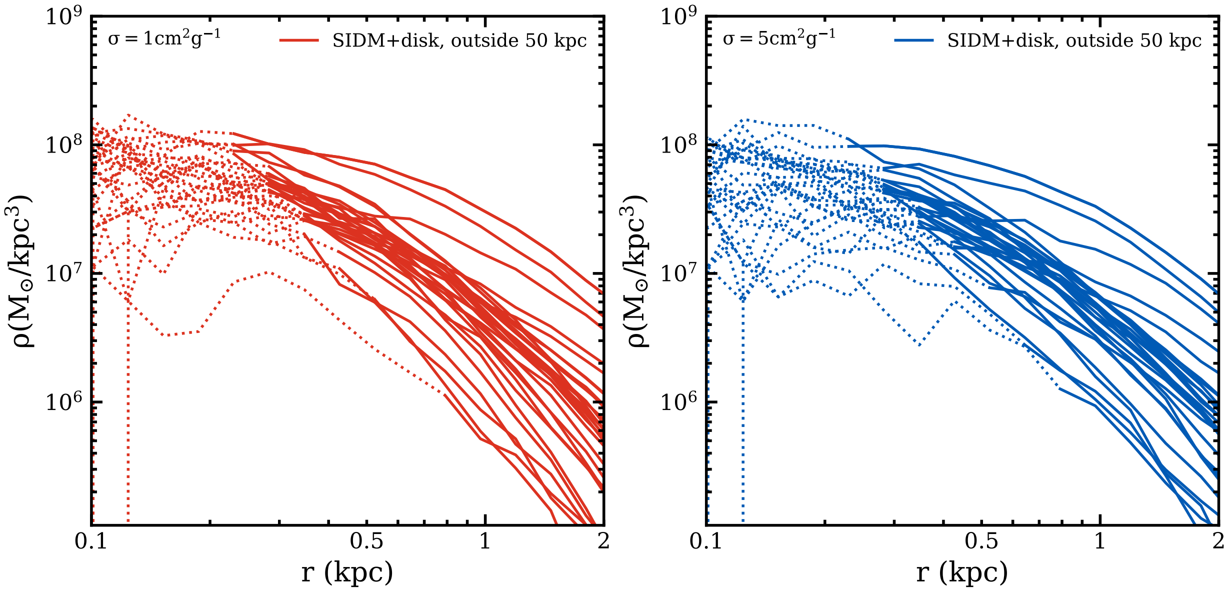

Figure 3.4: Density profiles of the 30 subhalos that are currently between 50 kpc and $R_{\mathrm{vir,host}}$ with largest V_{peak}. Density is calculated as mass per volume in 20 logarithmically spaced bins. Dotted lines indicate radii that enclose less than 200 particles.

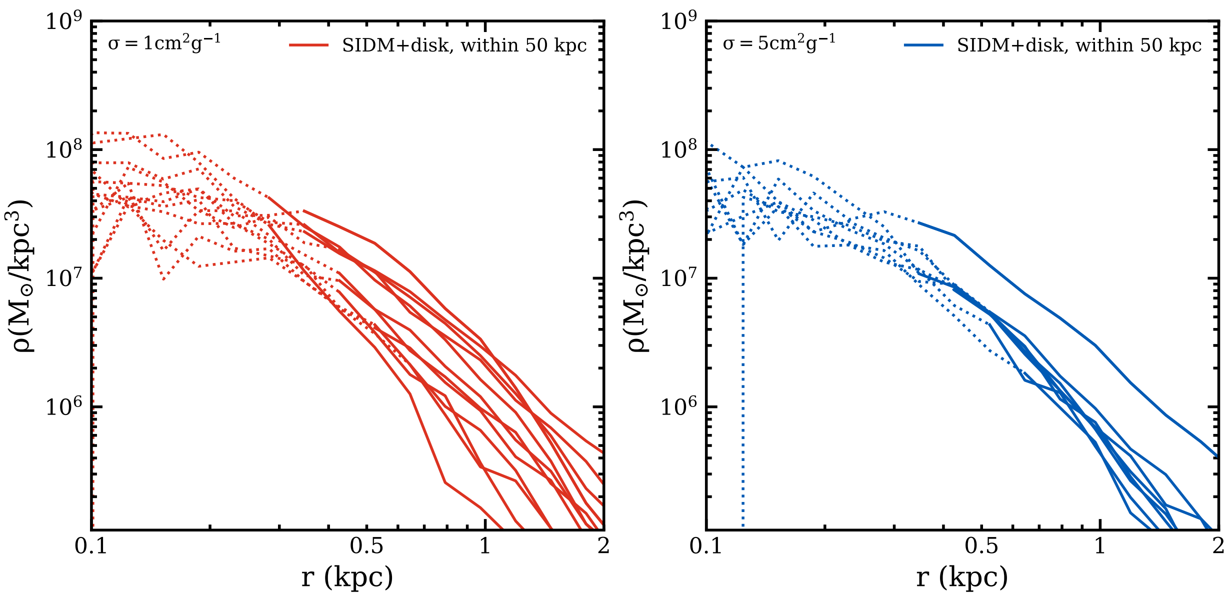

Figure 3.5: Density profiles of all subhalos that are currently within 50 kpc that are resolved at r_{max}. Density is calculated as mass per volume in 20 logarithmically spaced bins. Dotted lines indicate radii that enclose less than 200 particles.

3.3.1 Density Profiles

In this Section we study the $z = 0$ density profiles of subhalos in the SIDM simulations. To ensure that the subhalos we study are resolved, we make a series of resolution cuts based on the number of particles before they fall into the host and at $z = 0$. In our simulations, subhalos are well resolved if $V_{\rm peak} > 4.5$ km/s , which corresponds to a bound mass of about 5×10^6 $M_\odot$ (Robles et al., 2019). Additionally, we only look at subhalos that are resolved at $r_{\rm max}$, which, from convergence studies (Power et al., 2003; Hopkins et al., 2018a) amounts to having ≥ 200 particles within $r_{\rm max}$. We define $r_{\rm max}$ as the radius at which $V_{\rm max}$ occurs. We use this cut because subhalos with fewer particles may undergo significant artificial stripping in the simulation.

Using these resolved subhalos, we further define two populations. The first population of subhalos are currently within 50 kpc of the host center. These inner subhalos have come relatively close to the center of the host halo. The second population of subhalos are currently outside 50 kpc but within the virial radius of the host halo, $R_{\rm vir,host}$. For all MW-mass simulations that we use in this thesis, $R_{\rm vir,host} \approx 270$ kpc. These outer subhalos have likely not come as close to the center of the host halo but are likely bound to the host halo.

We use 50 kpc to separate the two populations to distinguish subhalos that have been through more dense regions of the host halo from those that have not. While the current position of a subhalo does not convey information about the subhalo's history, we find that it sufficiently distinguishes subhalos that have come closer to the host halo from those that have not. In section 4.1.2, we additionally look at the subhalos' pericenters to convey information about their history.

The number of subhalos within 50 kpc with $V_{\rm peak} > 4.5$ km/s and for which $r_{\rm max}$ encloses 200 particles is so low that we are able to look closely at all of these subhalos. In the S1 simulation, we have 12 such subhalos, and in the S5 simulation, we have 8. There are many subhalos outside 50 kpc with $V_{\mathrm{peak}} > 4.5$ km/s and for which r_{max} encloses 200 particles, so we take a closer look at a subset of subhalos within the outer population that have the largest V_{peak}, which corresponds to the most massive subhalos. Being the most massive subhalos, they most likely host massive satellite galaxies, similar to the ones that have been observed in the MW. We compare these subhalos to MW satellite galaxies in Chapter 4. We look at 30 subhalos currently outside 50 kpc in each SIDM simulation. We chose to look at 30 subhalos to roughly replicate the number of observed satellite galaxies.

To look at subhalo characteristics without influence from host halo particles, we distinguish subhalo and host halo particles from one another using their velocity with respect to the velocity of the subhalo, which we denote as the relative velocity. Particles that are bound in the subhalo have relative velocities $\mathcal{O}(10$ km/s), capping at about the maximum circular velocity, V_{max}, of the subhalo. Subhalos are orbiting the host halo at a velocity $\mathcal{O}(100$ km/s), so the relative velocity of the host halo particles will be much larger than the relative velocity of the subhalo particles. When looking at subhalo characteristics, we cut out any particles with $V > 3V_{\mathrm{max,sub}}$, leaving only the subhalo particles. Assuming particles in the subhalo have negligible velocity dispersion, cutting $V > V_{\mathrm{max,sub}}$ removes all subhalo particles. We cut $V > 3V_{\mathrm{max,sub}}$ to account for velocity dispersion.

Figure 3.4 shows the density profiles of the 30 subhalos that are currently between 50 kpc and $R_{\mathrm{vir,host}}$ with largest V_{peak} that are resolved at r_{max}. Figure 3.5 shows the density profiles of all subhalos currently within 50 kpc that are resolved at r_{max}. Density is calculated as mass per volume within 20 logarithmically spaced bins. The dotted lines indicate radii within which there are less than 200 subhalo particles.

We see no difference in the density profiles of S1 and S5 subhalos in the outer region (> 50 kpc). This conclusion is confirmed by Figure 6.1 where we directly compare corresponding subhalos in the S1 and S5 simulations. For subhalos closer to the host (< 50 kpc), we again see no difference in their density profiles, but we do see that S5 halos have slightly less mass, resulting in larger unresolved regions.

Although we are limited by resolution, we are able to suggest that outer subhalos (Figure 3.4) have cores that extend to larger radii than inner subhalos (Figure 3.5). Many of the outer subhalos have cores that extend to about 0.5 kpc while the inner subhalos have cores that extend only to about 0.15 kpc. This observation is further illuminated in Figure 6.3 where we are able to use an isothermal model to extend the density profiles to smaller radii.

Thus, we find that the S1 and S5 subhalos in the outer region of the host halo ($>$ 50 kpc) have comparable density profiles. Subhalos closer to the host ($<$ 50 kpc) have slightly lower masses in the S5 simulation, resulting in larger unresolved regions. In both SIDM models, we suggest that subhalos in the outer regions have more extended cores than those in the inner regions.

3.3.2 Vmax-Rmax Relation

We now take a closer look at the comparison between CDM, S1, and S5. Figure 3.6 shows the maximum circular velocity, $V_{\rm max}$, and radius of maximum circular velocity, $r_{\rm max}$, of all of the subhalos in Figures 3.4 and 3.5, color coded by their pericenters. $V_{\rm max}$ and $r_{\rm max}$ are calculated from the $z = 0$ particle data and pericenter is the subhalo's closest approach to the center of the host halo over all time, calculated using energy and angular momentum conservation, as detailed in Section 4.1.2. We observe a trend that subhalos with smaller pericenters have smaller $r_{\rm max}$ for a given $V_{\rm max}$. A similar trend is also mentioned by Robles & Bullock (2021), who characterize this trend by a power-law fit: $(r_{\rm max}/1{\rm kpc}) = {\rm A}({\rm V}_{\rm max}/10{\rm kms}^{-1})^{1.5}$ where A depends on the pericenter.

We find little difference in the $V_{\rm max}$ and $r_{\rm max}$ values of the S1 and S5 subhalos. To compare this to subhalos in CDM, we plot the power-law fit for all subhalos in the CDM+disk

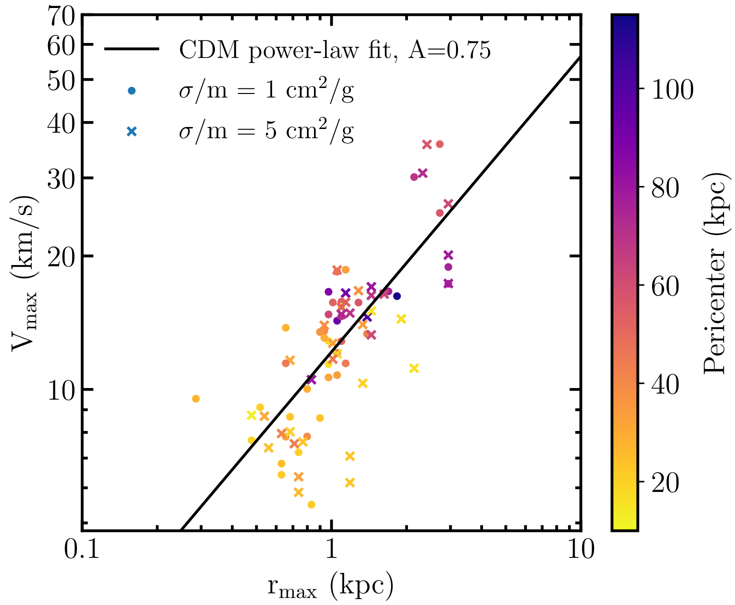

Figure 3.6: The maximum velocity as a function of the radius at maximum velocity at z=0 of the 30 resolved subhalos outside 50 kpc with largest $V_{\rm peak}$ and all resolved subhalos within 50 kpc. The dots and x's represent subhalos in the S1 or S5 simulation, and the color is determined by the pericenter. The black line shows the power-law fit for subhalos in the CDM+disk simulation (Robles & Bullock, 2021).

simulation in black in Figure 3.6. We find that subhalos in CDM and SIDM simulations have similar $V_{\rm max}$ and $r_{\rm max}$ values.

Thus, we find no significant difference in the $V_{\rm max}$ and $r_{\rm max}$ values of the subhalos in CDM, S1, and S5 simulations.

3.3.3 Mass Loss from Milky Way Host-Subhalo Dark Matter Scattering

The simulations that we analyse assume a velocity-independent cross section. However, a more general model of self-interactions includes a velocity dependence such that scattering rate is inversely proportional to velocity (Feng et al., 2009; Loeb & Weiner, 2011; Tulin et al., 2013; Boddy et al., 2014; Kaplinghat et al., 2016; Tulin & Yu, 2018). Thus, scattering

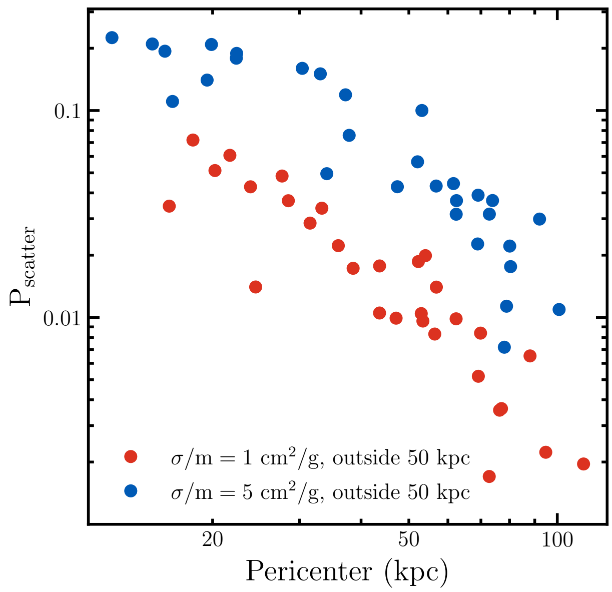

Figure 3.7: Probability that a single subhalo particle will scatter off a host halo particle in the subhalo's lifetime. We show this versus pericenter because subhalos with smaller pericenters traverse more dense regions in the host halo. We show the number of scatters for a particles in the 30 resolved subhalos currently outside 50 kpc with largest $V_{\rm peak}$.

interactions that happen at high relative velocities occur more frequently in our simulation than in a model with velocity-dependence. The highest velocity particle collisions that occur in our simulations are between subhalo and host halo particles as the subhalo orbits the host halo at velocities of order 100 km/s. These scattering events effect the mass and trajectory of the subhalo (Kummer et al., 2017).

First, we explore the measurable effects of the change in the subhalo's trajectory. After the host halo and subhalo particles interact, assuming the interacting particles have a large enough velocity, the host particles will escape the subhalo. The escaping particles decelerate in the subhalo's gravitational field, effectively transferring some of their momentum to the subhalo. Since the scattering particles are generally moving in the opposite direction as the subhalo, this momentum transfer decelerates the subhalo. When an orbiting subhalo decelerates, it moves radially inward towards the host halo. To measure this orbital change, we look at the pericenter of subhalos in our simulation.

As shown in Figure 4.2, CDM has a slightly flatter distribution of pericenters, with fewer subhalos at the peak pericenter and more at the two ends. We see no measurable difference between the pericenters of subhalos in the S1 and S5 simulation, indicating that subhalo-host halo particle interactions have a small effect on the subhalos trajectory for cross sections of 1 and 5 cm^2/g .

To quantify the effects on the mass of a subhalo due to a velocity independent cross section, we calculate the approximate mass lost by a subhalo due to scattering interactions between subhalo and host halo particles.

The interaction rate of a single particle within a subhalo is given by

$$\Gamma = \frac{\sigma}{m}\langle \rho_{\mathrm{host}}(r) V_{\mathrm{rel}}(r) \rangle \tag{3.1}$$

where σ is the cross section, and in our case $\sigma/m = 1$ or 5 cm^2/g , $\rho_{\mathrm{host}}(r)$ is the background density of the host halo at the position of the subhalo and $V_{\mathrm{rel}}(r)$ is the relative velocity between the host halo and the subhalo. We calculate the average density times velocity as:

$$\langle \rho_{\mathrm{host}}(r) V_{\mathrm{rel}}(r) \rangle = \frac{\sum_{\mathrm{i}} m_{\mathrm{i}} \Delta V_{\mathrm{i}}}{\mathcal{V}}. \tag{3.2}$$

Here $\Delta V_{\mathrm{i}} = V_{\mathrm{i}} - V_{\mathrm{subhalo}}$ is the velocity of the particle with respect to the subhalo's velocity. We sum over all particles, i, within a sphere of radius $r = 1$ kpc that have velocity $V_{\mathrm{i}} > 3V_{\mathrm{max,sub}}$. Both V_{subhalo} and $r_{\mathrm{vir,sub}}$, the virial radius of the subhalo, are determined by merger tree data. By excluding all particles that have a velocity less than three times the subhalo maximum circular velocity, we are cutting out the particles that are gravitationally bound to the subhalo. Assuming this cut removes *all* subhalo particles, the density we calculate is that of the host halo at the location of the subhalo. $\mathcal{V}$ represents the volume of the sphere of interest, calculated as $\frac{4}{3}\pi r^3$, where r is taken to be 1 kpc. To check our results, we also calculated the scattering probability using a volume of radius $r = 5$ kpc and we find the same results.

The probability that a single subhalo particle will scatter off a host halo particle is given by integrating equation 3.1 over the subhalo's full orbit. For convenience, we perform the integral from the time a subhalo is accreted into the virial radius of the host until today.

$$P_{\rm scatter} = 1 - \exp(-\int_{t_{\rm acc}}^{t_{\rm today}} \Gamma dt) \approx \int_{t_{\rm acc}}^{t_{\rm today}} \Gamma dt. \tag{3.3}$$

This approximation can be made for small $\int \Gamma dt$.

Figure 3.7 shows the probability of scattering of a particle in a given subhalo from when it first enters the host halo's virial radius until today. We plot this as a function of the pericenter of that subhalo. Shown are the probability that a particle scatters in the 30 subhalos with largest $V_{\rm peak}$ that are located outside 50 kpc from the center of the host halo. This figure shows, as expected, that scattering rate is proportional to density and cross section.

Figure 3.7 shows that our subhalos lose, on average, 2% (9%) of their mass in our S1 (S5) simulation. A subhalo with close pericentric passage, of about 20 kpc, in the S1 simulation will lose at most 7% of its DM particles. The larger cross section in the S5 simulation causes subhalos to lose more mass. A subhalo with close pericentric passage in the S5 simulation loses up to 23% of its mass. While a larger mass loss does make subhalos more likely to undergo tidal stripping, Figure 4.2 shows that pericenter alone does not lead to a significant difference in the number of subhalos that become fully tidally disrupted in the S1 versus the S5 simulations.

A similar analysis was conducted by Nadler et al. (2020a) for subhalos in their dark matter only simulations. They conclude that with an isotropic cross section of 2 $\mathrm{cm^2/g}$, subhalos with pericenters $\lesssim$ 70 kpc can lose about 10% of their infall mass due to host halo-subhalo particle interactions. Comparatively, subhalos with pericenters ≈ 70 kpc in our S1 (S5) simulation lose about 0.8% (4%) of their mass. This difference in mass loss may relate to the fact that we simulate the gravitational effects of a baryonic disk and bulge, while Nadler et al. (2020a) do not. The inclusion of the disk and bulge in MW simulations has been found to destroy subhalos with small pericentric passages.

It is notable that the three subhalos in these populations with smallest pericenters are all in the S5 simulation. To investigate these three subhalos further, we referred to their density profiles. These density profiles do not stand out from those of other subhalos, as is apparent from their $V_{\rm max}$ and $r_{\rm max}$ values. Starting with the subhalo with smallest pericenter, these subhalos have $V_{\rm max} = 8.75, 11.16, 15.03$ km/s, and $r_{\rm max} = 0.48, 2.14, 1.44$ kpc.

We conclude that mass loss due to subhalo-host halo interactions causes subhalos to lose, on average, 2% (9%) of their mass in our S1 (S5) simulation.

Chapter 4

Simulations versus Observations of Milky Way Satellite Galaxies

In this Chapter, I compare MW subhalos in N-body simulations that include a disk potential to MW satellite galaxies. Cross sections in the $1-5$ cm^2/g range have been shown to create large cores in dwarf and low-surface brightness galaxies and are therefore excellent model targets for studying the lower-mass MW satellites. I discuss the distribution function of the MW satellites and the mass threshold for galaxy formation in the context of $\sigma/m = 0, 1, 5$ cm^2/g and show that, according to current galaxy formation models, CDM DMO, CDM + disk, S1, and S5 simulations all produce fewer subhalos than the number of observed satellite galaxies. The circular velocity profiles of subhalos in S1 and S5 can account for the low density classical satellites, but they have trouble matching the majority of the satellites because they don't scatter to sufficiently high densities. My key result is that cross sections in the $1-5$ cm^2/g range are unlikely to be consistent with the central densities of MW dSphs.

This chapter is based on research published in the Monthly Notices of the Royal Astronomical

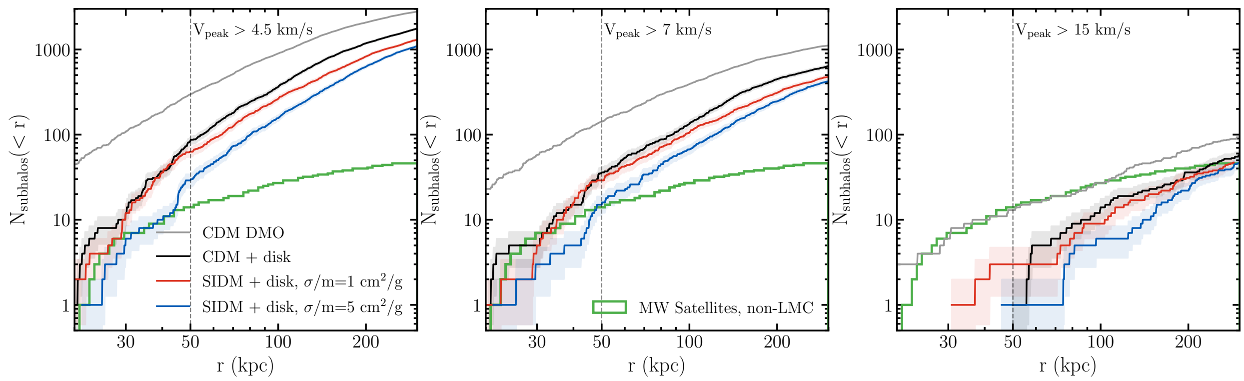

Figure 4.1: Cumulative number of subhalos within the virial radius of the host halo at z=0. We compare CDM dark matter only (gray), CDM with the baryonic disk (black), S1 with the baryonic disk (red), and S5 with the baryonic disk (blue) to observed Milky Way satellite galaxies (green). The left, middle, and right panels show subhalos with $V_{\rm peak}$ cuts of 4.5, 7, and 15 km/s , respectively. The vertical dashed line is a reminder that observations are likely not complete outside 50 kpc and we expect many other satellite galaxies to be observed in this region with upcoming telescopes.

Society. I use "we" throughout to acknowledge the joint contributions of myself (first author) and my co-authors.

4.1 Distribution Within the Milky Way

We now focus on the subhalo distribution within the host halo. Using $z = 0$ halo catalogs from merger trees, we look at the radial distribution of subhalos within 300 kpc from the center of the host halo. We will look at both the current position of subhalos, and their pericenters.

4.1.1 Current distance

Figure 4.1 shows the number of subhalos currently within a given radius of the host halo for CDM dark matter only (DMO), CDM with the baryonic disk, S1 with the baryonic disk, and S5 with the baryonic disk. In this section, we focus on three populations of subhalos: all well

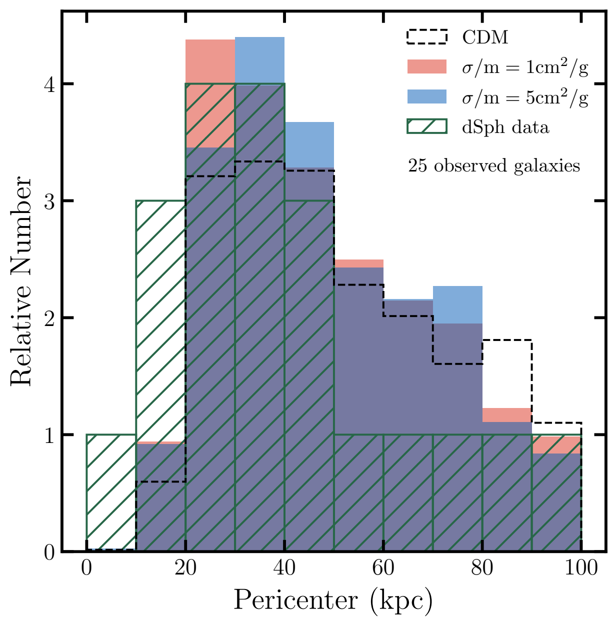

Figure 4.2: Pericenters of subhalos within the virial radius of the host halo and with V_{peak} ¿ 4.5 km/s at z=0. The Relative Number is equal to the number of subhalos at a given pericenter over the total number of observed dSphs, such that the sum of any one histogram is equal to the number of observed galaxies (in our case 25). We compare CDM (black), S1 (red), S5 (blue), and observed dSphs (green). We only include dSphs that are currently within 270 kpc from the center of the Galaxy. Histogram values for dSph data are found by taking the median of each bin after sampling the distribution of each dSph 10^3 times. Our sampled dSph data have Poisson distributions, indicating that $\sqrt{\text{N}}$ error bars are appropriate.

resolved subhalos ($V_{\rm peak} > 4.5$ km/s), more massive subhalos ($V_{\rm peak} > 7$ km/s), and the most massive subhalos ($V_{\rm peak} > 15$ km/s). Each panel shows subhalos with a different $V_{\rm peak}$ cut. To compensate for the variance among simulations we estimate an error of $\sqrt{N_{\rm subhalos}}$ for the CDM, S1, and S5 simulations. To compare the simulations to observations, we plotted the radial distribution of the observed MW satellites compiled in Simon (2019), excluding the six satellites that Patel et al. (2020) find are likely to be satellites of the Large Magellanic Cloud (LMC). We do not include any sky correction for satellites yet to be found, so the plotted curve should be treated as a lower limit to the actual radial distribution.

When looking at all resolved subhalos ($V_{\rm peak} > 4.5$ km/s) at and outside 50 kpc, all models produce more subhalos than observed. With the sensitivity and breadth of upcoming telescopes like the Vera C. Rubin Observatory, more satellite galaxies will likely be found, especially outside ~ 50 kpc. We do not focus on the radial distribution of satellites below 50 kpc because this region is more sensitive to the LMC. When looking at more massive subhalos ($V_{\rm peak} > 7$ km/s), S5 produces the same number of subhalos as observed galaxies within 50 kpc. CDM and S1 slightly over-predict the number of subhalos within 50 kpc, and we find that for only a slightly larger value of $V_{\rm peak} > 8$ km/s, CDM and S1 also produce the same number of subhalos as observed galaxies within 50 kpc. Again, all simulations over-predict the number of galaxies outside 50 kpc, which is likely due to incompleteness. Finally, when looking at only the most massive subhalos ($V_{\rm peak} > 15$ km/s), CDM, S1, and S5 under-predict the number of observed galaxies. Only CDM DMO (which is clearly not representative of the MW) has about the same number of subhalos as the number of observed galaxies within 50 kpc. Thus our simulations predict that $V_{\rm peak}$ must be below 15 km/s to be consistent with the observed galaxy sample, irrespective of the dark matter model.

It has been shown that not all subhalos host luminous galaxies (Sawala et al., 2015; Simpson et al., 2018; Benson et al., 2002; Somerville, 2002; Bullock et al., 2000), and the fraction of subhalos that do host luminous galaxies, depends on subhalo mass, reionization redshift, and baryon survival criterion (Kim et al., 2018) of the model. There have been many attempts to model the luminosity fraction, and for CDM DMO scenarios, a criteria of $V_{\text{peak}} > 23.5$ km/s is required to match simulations to observations (Dooley et al., 2017). This limit shifts to $V_{\text{peak}} > 7$ km/s for CDM + disk scenarios (Graus et al., 2019; Kelley et al., 2019). If we assume that the observed satellite data are complete within 50 kpc, S1 and S5 halos with V_{peak} down to 7 km/s are required to match the total number of observed satellites within 50 kpc, as seen in Figure 4.1.

This comparison between simulated subhalos and observed satellite galaxies within 50 kpc illuminates the trend that both CDM and SIDM models struggle to produce observed subhalo numbers at larger V_{peak} values. This result is based on one set of simulations, where our aim has been to compare the impact of dark matter self-interactions on this issue. A more through statistical analysis with a large set of simulations is clearly warranted given the importance of this issue.

For CDM, a Bayesian comparison between observed satellites and simulated subhalos at all radii by Jethwa et al. (2017) found that simulations match observations if subhalos with peak virial mass $M_{\text{vir}} > 2.4 \times 10^8$ $M_\odot$ (corresponding to $V_{\text{peak}} > 15$ km/s) form the faintest MW satellites. This is at odds with the results plotted in Figure 4.1 given the stark differences in the observed vs simulated satellites for $V_{\text{peak}} > 15$ km/s. The reasons for these large differences are not clear, and this should be studied further. We note that the largest effect on the subhalo population within 50 kpc (in our simulations) is due to the disk of the MW. For the disk mass and disk radius assumed here, the number of surviving CDM subhalos within 50 kpc is only about 30% of the number in the corresponding DMO simulation. What this implies is that the surviving satellite population is likely to be very sensitive to the disk modeling.

Some of this subhalo destruction may be due to artificial disruption. When comparing CDM N-body simulation, *Bolshoi* (Klypin et al., 2011), to `SatGen` (Jiang et al., 2021a), a semi-analytical subhalo evolution modeling framework which can track orphan galaxies, Green et al. (2021) find that accounting for orphan galaxies can boost the number of subhalos by up to a factor of two in the inner regions. With a factor of two more subhalos within 50 kpc, S5 would match the number of observed satellites for V_{peak} values greater than at least 7 km/s. However, Green et al. (2021) predict only 0.1 dex more subhalos below a mass of $m_{\text{sub}}/M_{\text{host}} < 10^{-4}$. Thus, artificial subhalo disruption should not greatly affect the results presented in Section 4.2 and onward.

A further complication is that, while we have removed some satellites that could have been associated with the LMC, we haven't included the gravitational impact of the LMC on the other satellites and the survival probability of the satellites in a consistent manner. This point has been noted in the literature (Nadler et al., 2021, 2020b; Bose et al., 2020). It is critical to explore this in more detail if we are to use the MW satellites to put a lower limit on the minimum halo mass to form galaxies. In the present analysis, we therefore focus our attention on the count within 50 kpc and not the detailed radial distribution, which is likely to have been impacted by the LMC.

These comments and results connect to interesting questions in galaxy formation at the faint end. Efforts in this regard have found that only dark matter halos with $V_{\text{peak}} > 20$ km/s form stars (Thoul & Weinberg, 1996; Okamoto et al., 2008; Ocvirk et al., 2016; Fitts et al., 2017). Subhalos with $V_{\text{peak}} = 7$ km/s have a virial temperature of about 2000 K (Graus et al., 2019), well below the atomic hydrogen cooling limit, 10^4 K. This suggests that in our S1 and S5 simulations (even when orphan galaxies are accounted for), as well as in CDM+disk simulations, subhalos would require molecular cooling to form stars (Graus et al., 2019; Kelley et al., 2019).

Manwadkar & Kravtsov (2021) come to a similar conclusion using the Caterpillar CDM simulation suite, which has comparable resolution to the simulations presented in this work but does not account for the gravitational potential of the baryonic disk. They are able to reproduce the observed radial distribution of satellite galaxies (when not accounting for orphan galaxies) only if halos below the atomic cooling limit are able to form stars.

Thus, it seems that the Missing Satellites problem has drastically changed since its original assessment (Kim & Peter, 2021).

In order for the number of subhalos produced in S1 and S5 simulations to agree with observations within 50 kpc, we find that stars must form in subhalos with $V_{\rm peak}$ *as low as 7 km/s . If only halos with* $V_{\rm peak} > 20$ *km/s can form stars, as suggested by some galaxy formation simulations, CDM DMO, CDM + disk, S1, and S5 all under-predict the number of observed satellites.*

4.1.2 Pericenter

We also look at the pericenter distributions of subhalos in the CDM, S1, and S5 simulations. Pericenter is defined as the minimum distance to the center of the host halo over all time. As noted by Garrison-Kimmel et al. (2017) a subhalo's orbit can drastically affect it's survival probability when the baryonic disk is taken into account. More specifically, few subhalos that come within 10 kpc of the center of the host halo survive.

Figure 4.2 shows pericenter histograms for CDM, S1, and S5 compared to *Gaia* data of satellite galaxies. In green, we show the satellite galaxies currently within 270 kpc of the host halo. The dashed black, solid red, and solid blue histograms show pericenters of simulated subhalos in CDM, S1, and S5 that are currently within 270 kpc of the host halo and have $V_{\rm peak} > 4.5$ km/s . The simulated subhalos are normalized to the number of observed halos for easier comparison.

For the CDM subhalos, pericenter is calculated by interpolating between snapshots (spaced by $14 - 16$ Myr) and selecting the minimum distance to the host (Kelley et al., 2019). For the SIDM simulations, we calculate pericenter by conserving energy and angular momentum between the two snapshots that straddle the subhalo's closest approach. This simple calculation, detailed in Section 4.1.3, assumes that the gravitational potential of the host halo is spherical and that no angular momentum is lost to dynamical friction. For cases where these assumptions do not hold we simply take the pericenter to be the minimum distance to the host captured in the simulation snapshots. To ensure that our calculated pericenters are reasonable, we only use calculated pericenter values that vary from the minimum distance captured in the simulation snapshots by less than 50%.

To compare simulation to observation, we use the inferred pericenter of satellite galaxies with respect to the MW (with a mass of 1×10^{12} $M_\odot$), taking into account the LMC with a mass of 1.8×10^{11} $M_\odot$ (Patel et al., 2020). We note that Patel et al. (2020) study all satellite galaxies that are associated with the LMC based on their membership to the MW's Vast Polar Structure. For satellites not given by Patel et al. (2020), we use pericenter data with respect to the MW (with a mass of 0.8×10^{12} $M_\odot$) assuming no effects by the LMC (Fritz et al., 2018). Using only Fritz et al. (2018) data, we found a similar histogram but with slightly smaller pericenters. Using a heavier MW mass (1.6×10^{12} $M_\odot$), we find a histogram with even smaller pericenters, as expected. We chose to show the lighter MW mass because it is more consistent with our simulated MW mass (1×10^{12} $M_\odot$). To account for the errors in inferred pericenters, we sampled the distribution of each dSph 10^3 times and plotted the median value for each pericenter bin.

Figure 4.2 shows that all three DM models predict a similar histogram to that of the observed dSphs, peaking at 20-40 kpc. We do notice a slight discrepancy between simulation and observation at pericenters below 20 kpc and at about 60 kpc. In each of these regions, we find that the sampling of the data gives a Poisson distribution, implying error bars of $\sqrt{N}$. While the discrepancy under 20 kpc was also noted in Kelley et al. (2019), we find it has been slightly alleviated when accounting for the LMC. [1] The remaining discrepancy within 20 kpc may be due to the non-identification of tidally and artificially disrupted halos that fall below the `Rockstar` resolution limit (Green et al., 2021). The discrepancy at about 60 kpc may be due to incomplete observations of the faintest dSphs outside 50 kpc. The middle panel of Figure 4.1 shows that there may be about 300 dSphs within 270 kpc rather than the 25 observed satellites that we include in Figure 4.2. These dSphs, which may be observed by upcoming telescopes like the Vera C. Rubin Observatory, would dominate the relative number count at larger pericenters.

Since the projection of dSphs pericenters does change based on the MW and LMC model, a range of MW and LMC models would be needed to make a more robust conclusion here. It would be interesting to study how the MW and LMC models would need to change in order to match the observed and simulated pericenter distributions. Our results indicate that pericenter distributions by themselves cannot distinguish between different cross sections in the $0 - 5$ cm^2/g range.

Looking at subhalo pericenters in conjunction with other observable quantities may prove useful in the future (Correa, 2021). A correlation between pericenter and the density at 150 pc is found among observed dSphs by Kaplinghat et al. (2019). We looked at pericenter in comparison to the density at 200 pc, and we found no correlation for subhalos in our S1 and S5 simulations. Robles & Bullock (2021) found a correlation between pericenter and $V_{\rm max}$ and $r_{\rm max}$. This correlation is discussed further in Section 4.2.

We are not able to use pericenter distributions alone to differentiate between CDM, S1, and S5, and we find a slight discrepancy between all three DM models and observations in subhalos with pericenters less than 20 kpc.

[1] The predicted pericenter distribution peaks below 10 kpc in simulations that do not include central disk potentials (Kelley et al., 2019), in significant disagreement with the observed distribution.

4.1.3 Pericenter Calculation

To calculate simulated subhalo pericenters with higher resolution than the snapshots captured by the simulation, we use a simple model that assumes conservation of energy and angular momentum between the two snapshots that straddle the pericentric passage. This refined interpolation only changes pericenter values by an average of 3%, which does not affect our conclusions.

The angular momentum is $L = rV_{\rm tan}$, where $V_{\rm tan}$ is the tangential velocity of the subhalo with respect to the host halo and r the relative distance. We approximate the gravitational potential as $A+Br$ and approximate $B = (\Delta V_{\rm tot}^2)/(2\Delta r)$ assuming energy ($= A+Br+V_{\rm tot}^2/2$) conservation. Pericentric passage occurs when the radial velocity is zero, implying that $V_{\rm tot}^2 = V_{\rm tan}^2 = L^2/r^2$. Rearranging this equation, we get:

$$Br_{\rm peri}^3 - (E - A)r_{\rm peri}^2 + \frac{L^2}{2} = 0 \tag{4.1}$$

We use the smallest positive root of this equation as the pericenter.

There are a few cases where our assumptions do not hold. If the subhalo has not made a pericentric passage, we use the distance of closest approach captured by the simulation, which is either in the first or last snapshot. If the subhalo's angular momentum changes by more than 50%, we use the distance of closest approach captured by the simulation. This may be the case if dynamical friction is changing the subhalo's orbit. If the gravitational potential is clearly non-spherical, resulting in a negative gradient of the gravitational potential, we again use the distance of closest approach captured by the simulation.

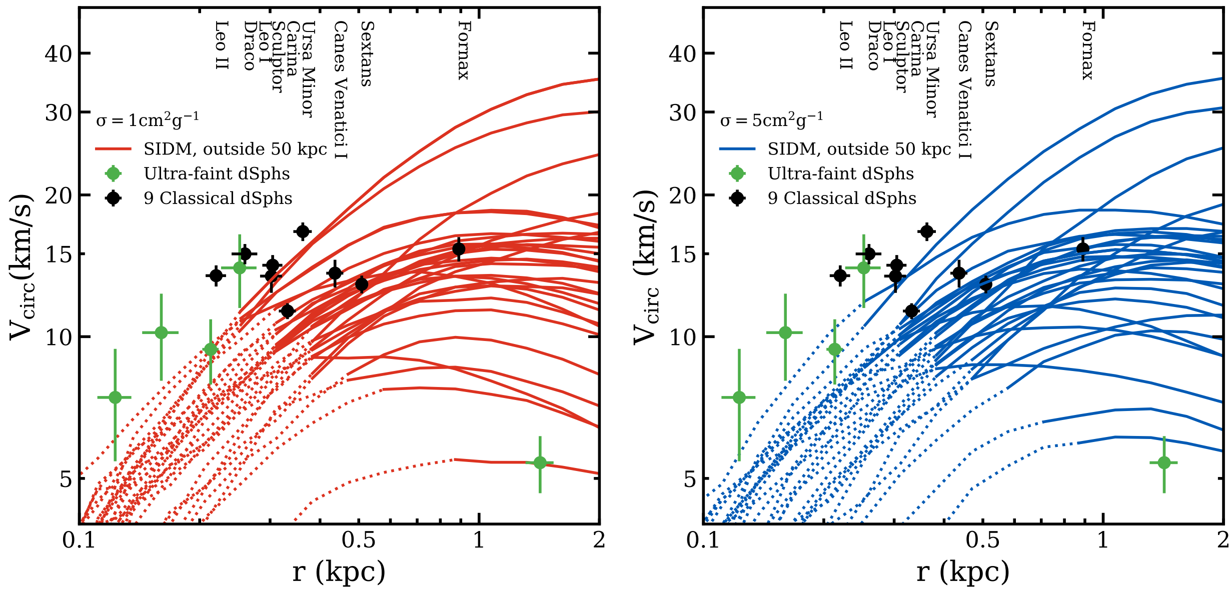

Figure 4.3: Circular velocity of the 30 subhalos that reside between 50 kpc and the host halo virial radius at z=0 with largest $V_{\rm peak}$ that are resolved at $r_{\rm max}$. We compare both S1 (left) and S5 (right) to the nine classical dwarf spheroidal (dSphs) MW satellite galaxies (black), which all reside outside 50 kpc from the MW center. We also compare to ultra-faint dSphs (green), some of which reside within 50 kpc and some which reside outside 50 kpc. For all dSphs, we plot the sphericallized half-light radius, $r_{1/2}$, and velocity at half-light radius, $V_{1/2}$. The dotted lines correspond to regions where the subhalos are not resolved, containing less than 200 particles.

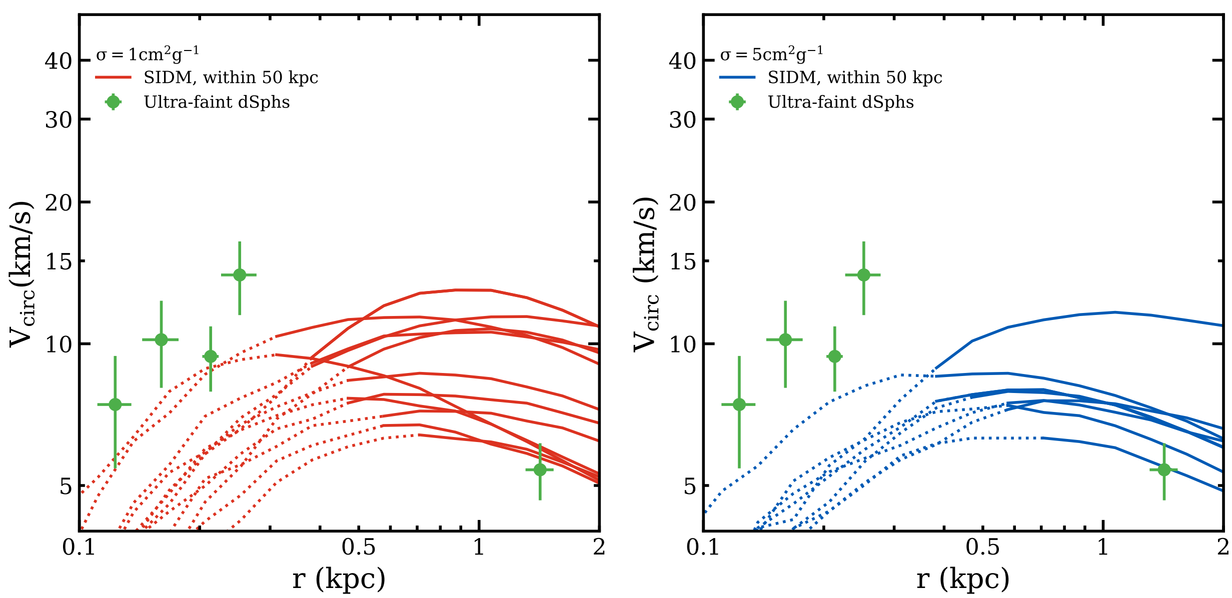

Figure 4.4: Circular velocity of all subhalos that reside within 50 kpc of the host halo center at z=0 that are resolved at $r_{\rm max}$. We have 12 resolved S1 subhalos and 8 resolved S5 subhalos. We compare to the sphericallized $r_{1/2}$ and $V_{1/2}$ of ultra-faint dSphs.

4.2 Circular Velocity Profiles

In this section we look at the $z = 0$ particle distribution within subhalos in the SIDM simulations. We focus on their circular velocity profiles, $V_{\rm max}$, and $r_{\rm max}$ values, in addition to their density profiles, which we show in Section 3.3.1. We define $r_{\rm max}$ as the radius at which $V_{\rm max}$ occurs. To make sure we can trust our $V_{\rm max}$ and $r_{\rm max}$ values, we only look at subhalos that are resolved at $r_{\rm max}$, which, from convergence studies (Power et al., 2003; Hopkins et al., 2018a) amounts to having ≥ 200 particles within $r_{\rm max}$. We use this cut because subhalos with fewer particles may undergo significant artificial stripping in the simulation. We use this resolution cut in addition to the resolution cut specified in Section 4.1: $V_{\rm peak} > 4.5$ km/s .

Using these resolved subhalos, we further define two populations. The first population of subhalos are currently within 50 kpc of the host center. These inner subhalos have come relatively close to the center of the host halo. The second population of subhalos are currently outside 50 kpc but within the virial radius of the host halo, $R_{\rm vir,host}$. For all simulations that we use in this paper, $R_{\rm vir,host} \approx 270$ kpc. These outer subhalos have likely not come as close to the center of the host halo but are likely bound to the host halo.

We use 50 kpc to separate the two populations to distinguish subhalos that have been through more dense regions of the host halo from those that have not. While the current position of a subhalo does not convey information about the subhalo's history, we find that it sufficiently distinguishes subhalos that have come closer to the host halo from those that have not. In Section 3.3.3, we additionally look at the subhalos' pericenters to convey information about their history.

The number of subhalos within 50 kpc with $V_{\rm peak} > 4.5$ km/s and for which $r_{\rm max}$ encloses 200 particles is so low that we are able to look closely at all of these subhalos. In the S1 simulation, we have 12 such subhalos, and in the S5 simulation, we have 8. There are many subhalos outside 50 kpc with $V_{\rm peak} > 4.5$ km/s and for which $r_{\rm max}$ encloses 200 particles, so we take a closer look at a subset of subhalos within the outer population that have the largest $V_{\rm peak}$, which corresponds to the most massive subhalos. Being the most massive subhalos, they most likely host massive dSphs, similar to the ones that have been observed in the MW. We look at 30 subhalos currently outside 50 kpc in each SIDM simulation. We chose to look at 30 subhalos to roughly replicate the number of observed dSphs.

To look at subhalo characteristics without influence from host halo particles, we distinguish subhalo and host halo particles from one another using their velocity with respect to the velocity of the subhalo, which we denote as the relative velocity. Particles that are bound in the subhalo have relative velocities $\mathcal{O}(10$ km/s $)$, capping at about the maximum circular velocity, $V_{\rm max}$, of the subhalo. Subhalos are orbiting the host halo at a velocity $\mathcal{O}(100$ km/s $)$, so the relative velocity of the host halo particles will be much larger than the relative velocity of the subhalo particles. When looking at subhalo characteristics, we cut out any particles with $V > 3V_{\rm max,sub}$, leaving only the subhalo particles. Assuming particles in the subhalo have negligible velocity dispersion, cutting $V > V_{\rm max,sub}$ removes all subhalo particles. We cut $V > 3V_{\rm max,sub}$ to account for velocity dispersion. The current circular velocity, $V_{\rm circ}$, as a function of radius of all of the selected subhalos are shown in Figures 4.3 and 4.4.

We also show two populations of observed dSphs, 1) the nine classical dSphs, and 2) a subset of ultra-faint dSphs with the cleanest data (Kaplinghat et al., 2019): Ursa Major I, Ursa Major II, Boötes I, Hercule, Coma Berenices, Canes Venatici II, Crater II, Reticulum II, Segue I, and Antlia II. Antilia II is a newly discovered and interesting satellite to compare to SIDM because it is the most diffuse satellite yet observed (Sameie et al., 2020a). Note that not all ultra-faint dSphs are shown in Figure 4.3 because of the radial range shown.

To compare the dSphs to the subhalo circular velocity profiles, we plot the inferred dSph circular velocity at half-light radius, $V_{1/2}$, versus the 3-Dimensional deprojected half-light radius, $r_{1/2}$. We calculate $V_{1/2}$ using (Wolf et al., 2010):

$$V_{1/2} = \sqrt{\frac{GM_{1/2}}{r_{1/2}}} = \sqrt{3\langle\sigma_{\rm los}\rangle^2} \tag{4.2}$$

where $M_{1/2} = \rho_{1/2}(4/3\pi r_{1/2}^3)$ and $\langle\sigma_{\rm los}\rangle$ is the average line of sight velocity dispersion.

For all dSphs, we use the 2-Dimensional half-light radius, $R_{\rm e}$, from Simon (2019) (except for Antlia II, which we get from Torrealba et al. (2019)) and convert to $r_{1/2}$ using the conversion factor of 4/3 (Wolf et al., 2010). We also modify $r_{1/2}$ by a factor of $\sqrt{1-\epsilon}$, where ϵ is the ellipticity given in Muñoz et al. (2018), to assume spherical symmetry for the dSphs, just as we do for our simulated halos (we use this sphericallized radius in Figures 4.3 and 4.4). In Section 4.2.1 we show the same dSphs *without* assuming spherical symmetry. For the nine classical dSphs we take $\rho_{1/2}$ from the Jeans analysis in Kaplinghat et al. (2019). For the ultra-faint dSphs, we use the mass estimator in Wolf et al. (2010) with the data in Simon (2019). The stellar mass contributions to $V_{1/2}$ are negligible for all dSphs. In the most extreme case of Fornax, stellar mass only contributes to $V_{1/2}$ by about 10%.

In Figures 4.3 and 4.4 we show the classical dSphs in black and the ultra-faint dSphs in green. The dotted lines correspond to regions where the subhalos are not resolved, containing less than 200 particles.

The increase in cross section from 1 to 5 cm^2/g does not visibly change the velocity profiles of the most massive subhalos outside 50 kpc. Within 50 kpc, we see a slight decrease in $V_{\rm circ}$ and $r_{\rm max}$ as cross section increases.

In both the S1 and S5 simulation, the low density classical dSphs can be hosted by the simulated subhalos. However, the high density of Draco cannot be explained, as was also found in previous studies (Valli & Yu, 2018; Read et al., 2018). We also find that Leo II, Sculptor, and Ursa Minor cannot be hosted by our S1 or S5 subhalos. Of the five ultra-faint dSphs that we show, two can be hosted by both the inner and outer SIDM subhalos, one can be accommodated by the outer subhalos only, and two cannot be allocated in any of the subhalos plotted. Overall, the SIDM subhalos in Figures 4.3 and 4.4 cannot host all of the observed dSphs.

The overall subhalo abundance may change with MW halo mass and we have accounted for such variance in the subhalos structural parameters by modelling circular velocity curves for subhalos with larger $V_{\rm max}$ and $r_{\rm max}$ values. We found that the $V_{\rm circ}$ values at 0.25 kpc were no larger than those we see in Figure 4.3. Thus, SIDM simulations with larger host halo masses will not necessarily create subhalos that can host the densest dSphs.

CDM simulations, both with and without a disk, predict the existence of subhalos that are more dense than the brightest dSphs that we have observed (see e.g. Figure 3 of Robles et al. (2019); Boylan-Kolchin et al. (2012); Garrison-Kimmel et al. (2014)), which motivated the TBTF problem. SIDM models can lead to the opposite problem: not predicting dense enough subhalos to explain the observed bright dSphs (Robles et al., 2019; Read et al., 2019). However, SIDM subhalos that undergo gravothermal core collapse are able to explain the densest dSphs (Kaplinghat et al., 2019; Kahlhoefer et al., 2019; Nishikawa et al., 2020). In Figures 4.3 and 4.4, we do not see any subhalos that can explain the densest dSphs, which is the first indication that subhalos in the S1 and S5 simulations are not experiencing core collapse. We discuss this further in Section 6.2.

4.2.1 Non Spherical Symmetry

In this section we show the S1 and S5 subhalo $V_{\rm circ}$ profiles compared to observed dSphs that have not been sphericalized. While we do not assume spherical symmetry in observed dSphs, we do still assume that our simulated subhalos are spherically symmetric, so we are hesitant to draw strong conclusions from this comparison. We plot the same subhalo circular velocity profiles as in Figures 4.3 and 4.4 compared to the same dSphs shown in Figures 4.3 and 4.4. Table 4.1 lists the projected 2D half-light radius, $R_{\rm e}$, the deprojected 3D half-light radius, $r_{1/2}$, the ellipticity, and the sphericallized 3D $r_{1/2}$.

To compare the dSphs to the subhalo circular velocity profiles, we plot the dSph velocity at half-light radius, $V_{1/2}$ versus the 3 Dimensional deprojected half-light radius, $r_{1/2}$. We calculate $V_{1/2}$ using equation 4.2 and the $\langle\sigma_{\rm los}\rangle^2$ in Simon (2019). We use the $R_{\rm e}$ in Simon (2019) and convert to $r_{1/2}$ using the conversion of 4/3 (Wolf et al., 2010).

Figure 4.5 shows that both our S1 and S5 subhalos can house all but two of the classical dSphs and all but one of the ultra-faint dSphs plotted. Previous studies have also found that Draco is an outlier when compared with subhalos formed in SIDM simulations (Valli & Yu, 2018; Read et al., 2018). We find that with the most recent data, Leo II is also in tension with our simulated subhalos.

The left panel of figure 4.6 shows that the subhalos within 50 kpc in our S1 simulation can explain the observed ultra-faint dSphs well. However, the right panel of figure 4.6 shows that the subhalos within 50 kpc in our S5 simulation have trouble explaining all of the observed ultra-faint dSphs.

Thus, the largest S5 subhalos can account for observed dSphs as well as S1 subhalos do. While subhalos in both simulations can account for the low density classical satellites, they have trouble matching the majority of the satellites because they don't scatter to sufficiently high densities.

dSph	R_e (pc)	$r_{1/2}$ (pc)	ϵ	$r_{1/2}(1-\epsilon)^{1/2}$ (pc)
Sculptor	279	372.0	0.33	304.50
Fornax	792	1056.0	0.29	889.80
Carina	311	414.7	0.36	331.73
Leo I	270	360.0	0.3	301.20
Sextans	456	608.0	0.3	508.69
Leo II	171	228.0	0.07	219.88
CVn I	437	582.7	0.44	436.03
UMi	405	540.0	0.55	362.24
Draco	231	308.0	0.29	259.53
UMa II	139	185.3	0.56	122.94
UMa I	295	393.3	0.59	251.86
Boötes I	191	254.7	0.3	213.07
Hercules	216	288.0	0.69	160.35
Cb I	69	92.0	0.37	73.02
CVn II	71	94.7	0	94.67
Cra II	1066	1421.3	0	1421.33
Ret II	51	68.0	0.58	44.07
Seg I	24	32.0	0	32.00
Ant II	2920	3893	0.38	3065.61

Table 4.1: Radial data of all dSphs shown in this paper. The 2D projected half-light radius, R_e, is taken from Table 1 in Simon (2019). We convert to 3D deprojected half-light radius, $r_{1/2}$ by multiplying by 4/3 (Wolf et al., 2010). The ellipticity, ϵ is the Plummer model value from Table 3 in Muñoz et al. (2018). Finally, the sphericallized 3D $r_{1/2}$ is calculated as 3D $\mathrm{r}_{1/2}\sqrt{1-\epsilon}$. Data for Ant II is taken from Torrealba et al. (2019). The first nine rows are the classical dSphs, and the last 10 rows are the ultra-faint dSphs that we use in this paper.

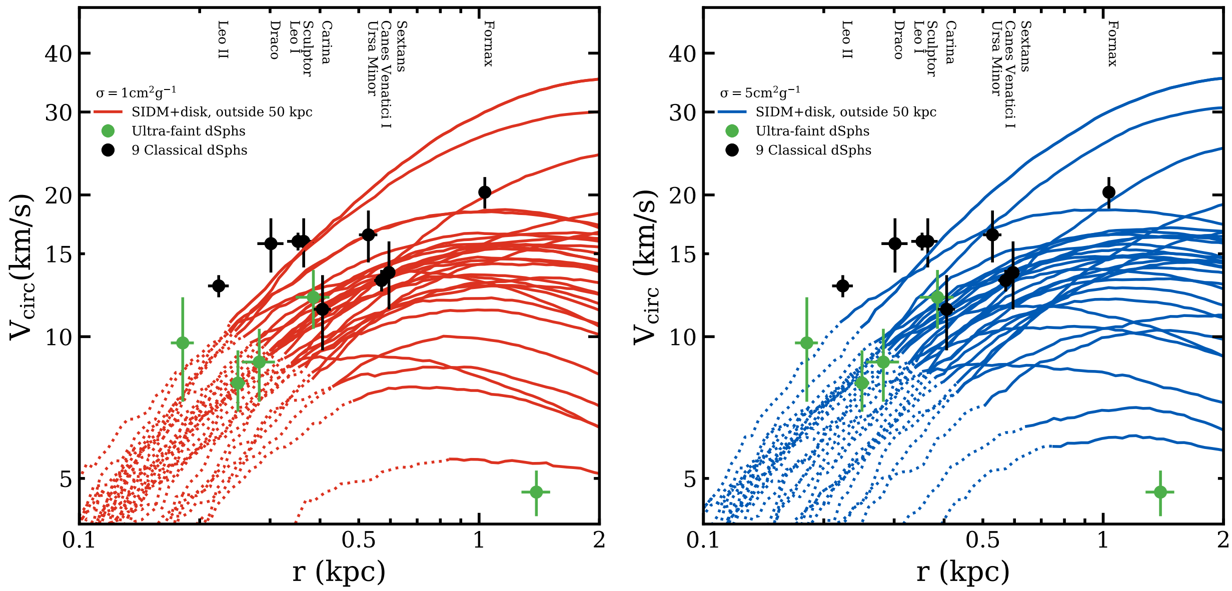

Figure 4.5: Circular velocity of the 30 subhalos that reside between 50 kpc and the host halo virial radius at z=0 with largest $V_{\rm peak}$ that are resolved at $r_{\rm max}$. We compare both S1 (left) and S5 (right) to the nine classical dSphs, which all reside outside 50 kpc from the MW center. We also compare to ultra-faint dSphs, some of which reside within 50 kpc and some which reside outside 50 kpc. We plot the dSph deprojected half-light radius, $r_{1/2}$ (given in Table 4.1), and velocity at half-light radius, $V_{1/2}$ not assuming spherical symmetry.

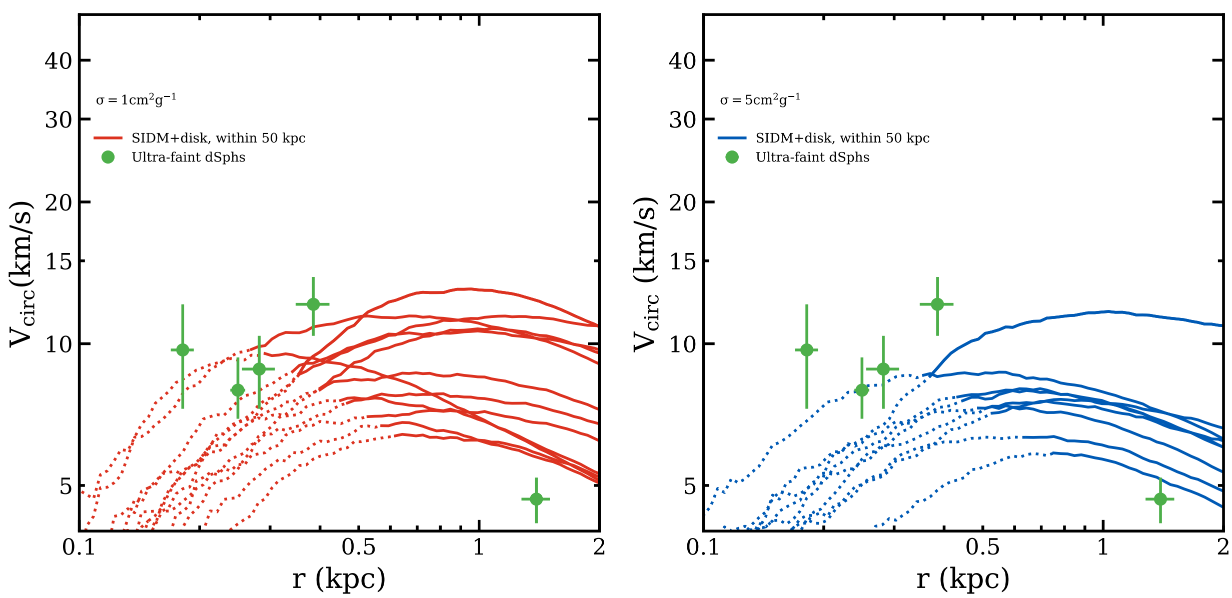

Figure 4.6: Circular velocity of all subhalos that reside within 50 kpc of the host halo center at z=0 that are resolved at $r_{\rm max}$. We have 12 resolved S1 subhalos and 8 resolved S5 subhalos. We compare to ultra-faint dSphs that reside within 50 kpc. We plot the dSph deprojected half-light radius, $r_{1/2}$ (given in Table 4.1), and velocity at half-light radius, $V_{1/2}$ not assuming spherical symmetry.

Chapter 5

Simulations of Low-Mass Halos with Large Cross Sections

In this Chapter I introduce a suite of cosmological, N-body simulations of low-mass halos ($M = 10^{10}$ $M_\odot$) with large cross sections ranging from $\sigma/m = 30 - 140$ cm^2/g . I discuss the SIDM implementation in detail, including the convergence of two numerical parameters in the time-stepping mechanism. I go on describe the six different initial conditions used, focusing on halo growth and subhalo orbits. Based on these quantities, I differentiate early-forming halos with few massive mergers and few mergers on radial orbits from late-forming halos with frequent or massive mergers on radial orbits.

This chapter is based on research in preparation for submission to the Astrophysical Journal. I use "we" throughout to acknowledge the joint contributions of myself (first author) and my co-authors.

5.1 Simulation Methodology

We present a suite of DM-only (DMO) zoomed cosmological simulations of dwarf halos ($M_{\rm host} \sim 10^{10}$ $M_\odot$, hereafter "m10s"), run with the `GIZMO` code (Hopkins, 2015) that uses a Tree-Particle-Mesh gravity solver. The suite samples a range of initial conditions to compare halo evolution in CDM and SIDM cosmologies. Collisionless gravity is softened with a cubic-spline kernel and a fixed Plummer-equivalent softening length $\epsilon_{\rm DM} = 28$ pc, consistent with Hopkins et al. (2018b); Wheeler et al. (2019); Wetzel et al. (2023). Table 5.1 summarizes the runs and their key parameters.

We adopt a fixed gravitational softening rather than an adaptive one because it is computationally cheaper and reduces numerical heating that can bias the evolution of collisionless and self-interacting DM (Hopkins et al., 2018b; Palubski et al., 2024). Our choice of $\epsilon_{\rm DM}$ meets the spatial- and mass-resolution criteria of van den Bosch & Ogiya (2018) for reliably resolving the inner structure of isolated halos and the convergence criteria of Mace et al. (2024) for gravothermal collapse in SIDM, helping ensure the results are not dominated by numerical relaxation.

5.2 SIDM Methodology

DM self interactions are implemented in the `GIZMO` code (Fitts et al., 2019; Sameie et al., 2021; Vargya et al., 2021; Shen et al., 2021, 2024; Arora et al., 2024) using the Monte Carlo-based scattering method from Rocha et al. (2013); Peter et al. (2013), which is summarized briefly here. In this procedure, the DM simulation particle i located at position $\mathbf{r}$ is associated with a kernel $W(r, h_{s,i})$ with smoothing length $h_{s,i}$. The smoothing length roughly corresponds to the size of the particle and determines the number of nearest neighbors it scatters with. We use the standard SIDM implementation in `GIZMO` where $h_{s,i}$ is adaptive and set its minimum value to 0.3 pc.

The SIDM interaction rate between simulation particles i and j is given by

$$\Gamma_{ij} = (\sigma/m)\; m_{\rm DM}\; V_{\rm rel}\; g_{ij}\,, \tag{5.1}$$

where $m_{\rm DM}$ is the mass of the DM simulation particle and $V_{\rm rel}$ is the relative velocity between particles i and j. The quantity g_{ij} is the kernel overlap between the two particles, defined as

$$g_{ij} = \int d^3\mathbf{x}\; W(|\mathbf{x}|, h_{s,i})\; W(|\mathbf{x} + \delta\mathbf{x}_{ij}|\,, h_{s,j})\,, \tag{5.2}$$

with $\delta\mathbf{x}_{ij}$ corresponding to the particle separation and the integral evaluated over the kernel volume. To simplify the calculation of g_{ij}, the smoothing length of each particle is set to $h_{\rm avg} = (h_{s,i} + h_{s,j})\,/2$. W represents cubic spline kernel in this work (e.g., Rocha et al., 2013).

The number of scattering events of particle i with any of its neighbors j in the timestep δt_i is

$$P_{ij} = \Gamma_{ij}\,\delta t_i\,. \tag{5.3}$$

The timestep δt_i is determined adaptively and depends on the gravitational acceleration that the particle experiences. As shown by Palubski et al. (2024); Mace et al. (2024), the SIDM interactions are sensitive to the choice of two key parameters. The first is the tolerance parameter, η, which scales how δt_i depends on the gravitational acceleration. The second is the maximum probability for a particle to scatter within a single timestep, defined as κ. We set $\kappa = 0.002$ and $\eta = 0.05$ in this work. Section 5.2.1 discusses these choices in more detail and presents the results of our convergence testing.

As summarized in Table 5.1, most of the halos in the suite are run assuming a velocity-independent SIDM cross section of either 30, 70, or 140 cm^2/g . One halo (m10b-vdSIDM) is run using a velocity-dependent scattering cross section of the form

$$\sigma(V_{\rm rel}) = \frac{\sigma_0}{1 + (V_{\rm rel}/w)^4} , \tag{5.4}$$

where w is a characteristic velocity below which the cross section is approximately constant $\sigma(V_{\rm rel} \ll w) \approx \sigma_0$. This is the default SIDM parametrization in `GIZMO` and approximates the viscosity cross section for realistic SIDM models (see e.g., Yang et al. (2023a)). This cross section is consistent with observational constraints at cluster scales and is expected to cause a fraction of low-mass halos and subhalos to gravothermally collapse (e.g., Turner et al., 2021; Lovell et al., 2017).

5.2.1 Adaptive Time-Stepping Parameter κ

Simulation time-stepping mechanisms can artificially impact halo evolution, particularly when including non-gravitational self-interactions (Palubski et al., 2024). An adaptive time-stepping mechanism allows the timestep that each particle is evolved to be calculated based on its local density and gravitational acceleration, such that it is fine enough to resolve physical interactions yet does not waste resources on particles with infrequent interactions. The limit on local density is set by κ, and the limit on gravitational acceleration is set by η.

κ determines the upper limit of the probability that a particle interacts with any one of its neighbors within one timestep. This parameter is designed to decrease the probability that a particle scatters more than once in a given timestep, which may lead to energy and momentum non-conservation. κ is defined as $\Gamma_{ij}\ \delta t_i < \kappa$ where Γ_{ij}, the scattering rate of particle i with its neighbor j, is dependent on the cross section, σ/m, and the SIDM smoothing length, $h_{\rm s}$ (Palubski et al., 2024). When the scattering rate approaches the upper

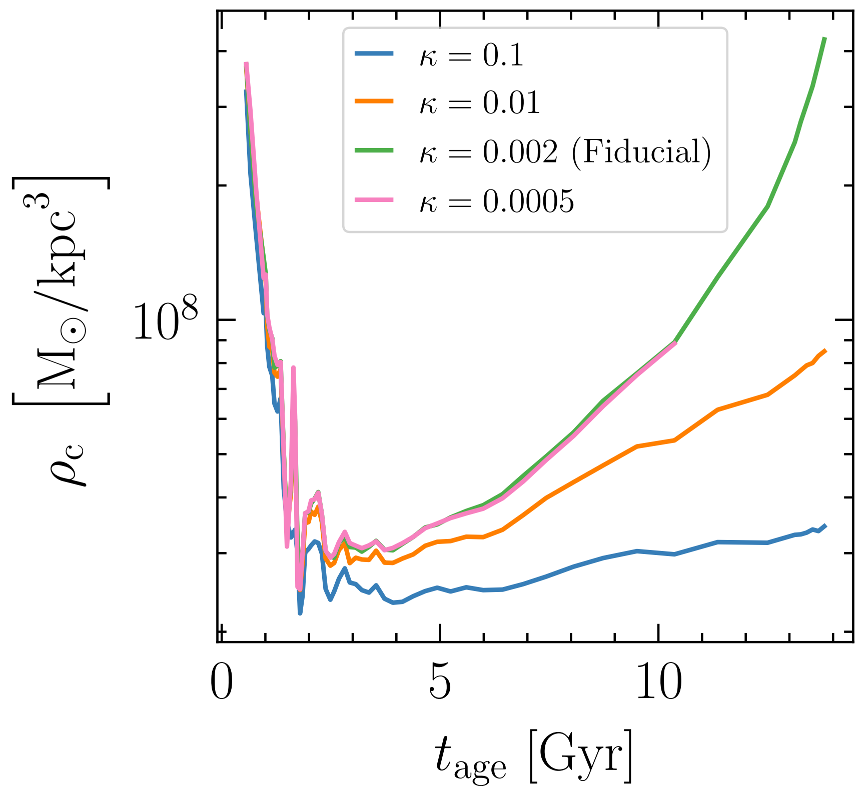

Figure 5.1: Evolution of the central densities of the m10q-s70 simulation with time-stepping parameter κ varied. Core densities are larger and gravothermal collapse occurs earlier with smaller values of κ. The fiducial value of κ is shown by the green line. We also test 1/4 our fiducial value ($\kappa = 0.0005$, pink) and find convergence between this value and our fiducial κ. We use GIZMO's fiducial value for $\eta = 0.05$ and plan to conduct convergence testing on η in the future.

limit, the timestep that that particle experiences, δt_i, decreases. The default value for κ in GIZMO is 0.2, but we probe smaller values, which have been shown to reduce artificial heating during core collapse in isolated halos (Palubski et al., 2024). We test $\kappa = 0.1$, 0.01, 0.002, and 0.0005. Our fiducial value for κ is 0.002, which agrees with $\kappa = 0.005$, indicating convergence. The simulation with $\kappa = 0.0005$ was not run to completion because particles with extremely small timesteps slowed the simulation.

Time-stepping is also set by the gravitational acceleration that a particle experiences within timestep δt_i. The tolerance parameter, η is defined as $\delta t_i = \sqrt{2\eta\epsilon_{\mathrm{DM}}/a}$ (Palubski et al., 2024). Here ϵ_{DM} is the gravitational force softening and a is the magnitude of the acceleration that the particle experiences. η becomes important in high density regions where particles experience large accelerations. The default value for η in cosmological DMO simulations with GIZMO is 0.05, which we use as a fiducial value. We plan to conduct convergence testing of η in future work.

Figure 5.1 shows the core density evolution of the m10q-s70 simulation with different values of κ. Here core density is defined as the innermost density of the analytic model fit to the core of the halo, as defined in Section 8. The simulations with large values of κ collapse slower and thus produce lower density cores at $z = 0$. This is likely due to artificial heating since large values of κ can result in multiple scattering events per timestep. These results agree with those in Palubski et al. (2024), where they are able to use total energy to confirm that larger values of κ lead to artificial heating in the core. These results, and those found by Palubski et al. (2024), agree that a value of $\kappa = 0.002$ best matches the analytic model.

5.3 Initial Conditions

The ICs used in this work sample across halo environments, varying formation history, as well as halo mass and concentration. They are chosen from a set of halos that have been well-studied in the context of CDM (Kim et al., 2013; Fitts et al., 2017; Hopkins et al., 2018b) by the FIRE project (Hopkins et al., 2014) and are referred to as m10q, m10b, m10d, m10f, m10i, and m10j. Given the mass and concentration for each halo, the fluid model expectation is that they should each collapse within a Hubble time with $\sigma/m = 70\ \mathrm{cm}^2/\mathrm{g}$. Unless otherwise noted, the simulations are run to the present day ($z = 0$). Some simulations are not run to the present day because high density regions increase the computational time necessary to run them further, as noted throughout the text.

The m10q halos are evolved in a WMAP 7/9 cosmology (Komatsu et al., 2011), adopted from the AGORA collaboration (Kim et al., 2013): $\Omega_\mathrm{m} = 0.272$, $\Omega_\Lambda = 0.728$, $\Omega_\mathrm{b} = 0.0455$, and $H_0 = 70.2$ km s^{-1} Mpc^{-1}. The remaining halos use a slightly different cosmology, following the Planck Collaboration 2014 results (Ade et al., 2014): $\Omega_\mathrm{m} = 0.266$, $\Omega_\Lambda = 0.734$, $\Omega_\mathrm{b} = 0.0449$, and $H_0 = 71$ km s^{-1} Mpc^{-1}. These slight differences of cosmological parameters impact halo-to-halo variation at the 1% level (Hopkins et al., 2018b), which is less than the variation of impacts from SIDM discussed in this work.

Table 5.1 characterizes the halo IC and DM particle mass (m_DM) of each simulation. The variation in m_DM across simulations is due to box size: m10q is run in a box with 5 Mpc side length while the other simulations are run in 25 Mpc boxes. We validate that these simulations are converged at this resolution by running versions with 8 and 64 times larger particle masses than the fiducial values, as discussed in more detail in Section 5.3.1.

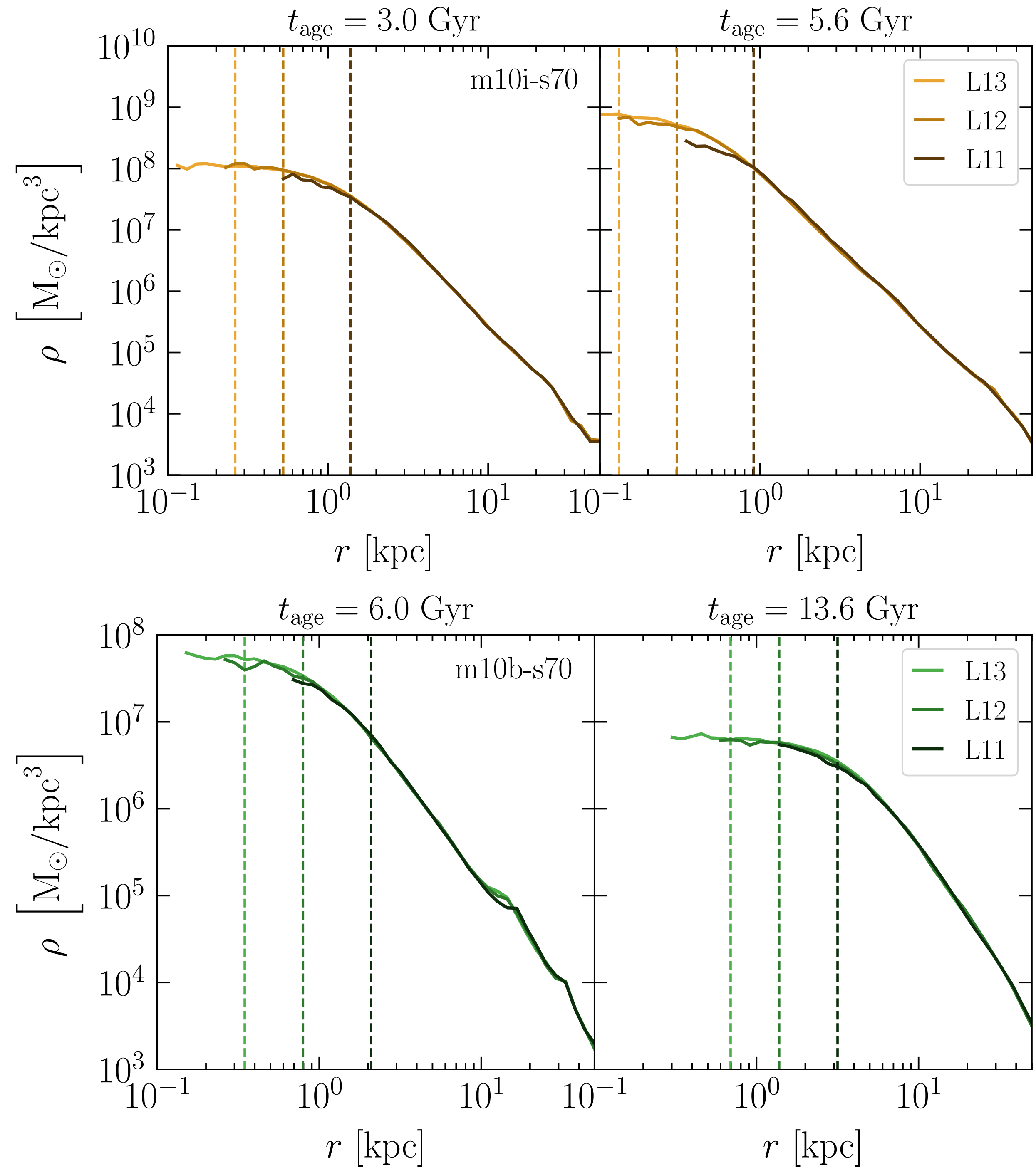

Figure 5.2: Density profiles of halos m10i-s70 (top) and m10b-s70 (bottom) at the fiducial resolution (L13), and at two lower resolutions with 8 (L12) and 64 (L11) times larger particle masses. The dashed vertical lines correspond to the Power radius (Power et al., 2003) which estimates the radius of numerical convergence. Density profiles are only plotted at radii that enclose at least 200 particles. We show each halo at the latest time that all three resolutions are run to (5.6 Gyr for m10i and 13.6 Gyr for m10b) and at an earlier snapshot (3.0 Gyr for m10i and 6.0 Gyr for m10b). Both halos show that the density profiles of all three resolutions agree beyond the corresponding Power radii, indicating that the simulations achieve numerical resolution.

5.3.1 Resolution Convergence

To examine numerical resolution of the simulations presented in this work, Figure 5.2 shows the density profiles of two halos at the fiducial mass ($m_{\rm DM} = 3 \times 10^3$ $M_\odot$) and spacial ($\epsilon_{\rm DM} = 28$ pc) resolution as well as at two lower resolutions. L12 corresponds to a resolution with $m_{\rm DM} = 2.4 \times 10^4$ $M_\odot$ and $\epsilon_{\rm DM} = 56$ pc and L11 corresponds to a resolution with $m_{\rm DM} = 1.9 \times 10^5$ $M_\odot$ and $\epsilon_{\rm DM} = 110$ pc. Numerical convergence is expected beyond the Power radius (Power et al., 2003), which corresponds to a radius that encloses $\sim$ 2500 particles (Fitts et al., 2019). The Power radii (determined by DM particles) are shown as dashed vertical lines in Figure 5.2 for each resolution.

We test numerical convergence in two halos: m10i-s70 as an example halo that collapses, and m10b-s70 as an example halo that doesn't collapse due to mergers. We show density profiles for halo m10i-s70 at the time of minimum density (3.0 Gyr) and at the latest snapshot available for all simulations (5.6 Gyr). We show density profiles for halo m10b-s70 before the major merger (6.0 Gyr) and at the latest snapshot available for all simulations (13.6 Gyr). For both halos, the density profiles agree well at each resolution for all converged radii.

5.4 Halo Merger Histories

To track the halos in our suite, we construct halo catalogs using `Rockstar` (Behroozi et al., 2013) and then link the halos across time using `consistent-trees` (Behroozi et al., 2013), following the method described by Samuel et al. (2019); Sameie et al. (2020a). Figure 5.3 shows the mass evolution of halos m10q-s70, m10d-s70, m10i-s70, m10j-s70, m10f-s70, and m10b-s70 . The arrows along the horizontal axis indicate the infall time of subhalos that merge with each host with $m_{\rm sub}/M_{\rm host} \geq 0.01$, where $m_{\rm sub}$ is the subhalo mass. The arrow color corresponds to $m_{\rm sub}/M_{\rm host}$ at infall.

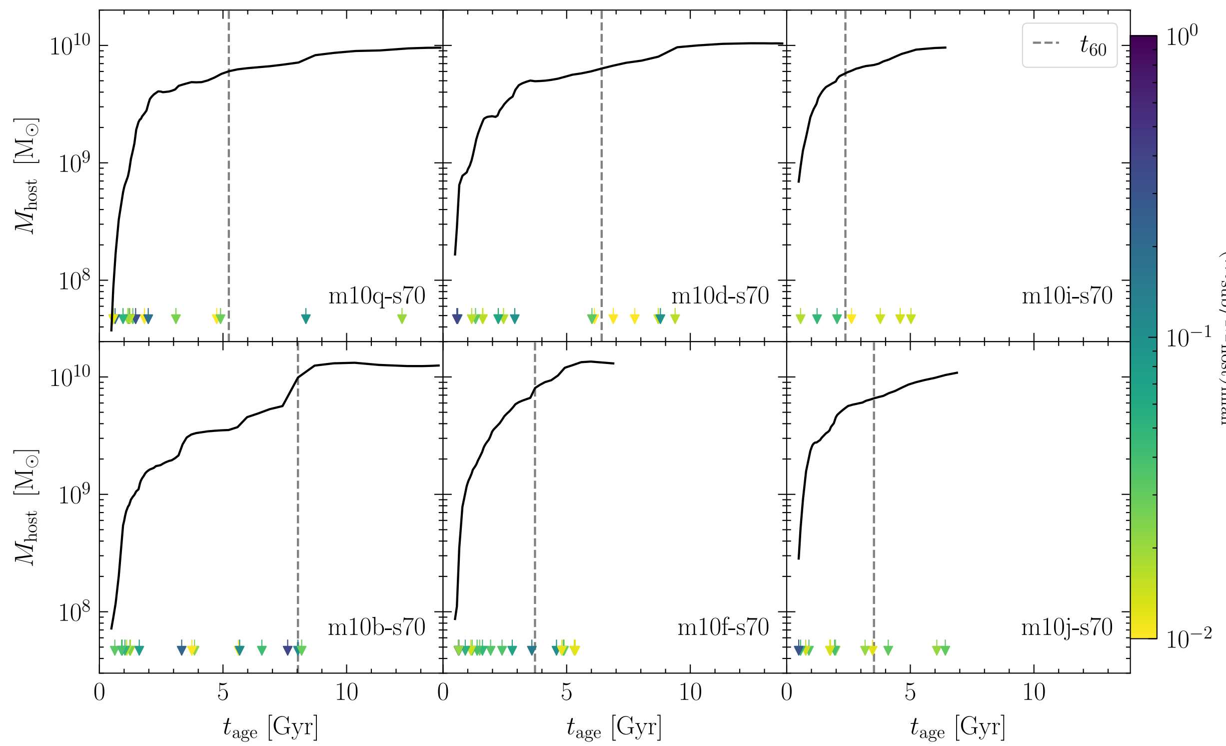

Figure 5.3: Evolution of host halo mass with time. Results are provided for halos m10q, m10d, m10i, m10b, m10f, and m10j with $\sigma/m = 70$ cm^2/g . The time at which the halo reaches 60% of its final mass, t_{60}, is indicated by the dashed gray line. Arrows along the x-axis indicate the infall time of subhalos, with the color corresponding to $m_{\rm sub}/M_{\rm host}$ at infall. Darker colors indicate more massive subhalos, relative to the host, at infall. All subhalos that fall into the virial radius of the host with a mass $m_{\rm sub} \geq M_{\rm host}/100$ at the time if infall are shown. Halos in the top row are early-forming—reaching 60% of their final mass in the first half of their growth times, and halos in the bottom row are late-forming—reaching 60% of their final mass in the second half of their growth times.

The halos included in Figure 5.3 represent a variety of formation histories, with some gaining mass more rapidly than others. To guide the eye, the time at which each halo reaches 60% of its final mass, defined as t_{60}, is indicated by the vertical dashed-gray line. Table 5.2 summarizes some key features of each halo's history, including the total number of mergers that are more than 0.01 and 0.1 times the mass of the host at infall. For the major mergers, defined as $(m_{\rm sub}/M_{\rm host})_{\rm infall} > 0.3$, the infall time and tangential velocity at infall are also provided. The latter quantity, $V_{\rm tan}$, is calculated as $|\vec{v} \times \hat{r}|$, where $\vec{v}$ is the subhalo velocity with respect to the host halo and $\hat{r}$ is a unit vector from the center of the host halo to the subhalo. This is evaluated at infall and normalized by $V_{\rm tot}$, the magnitude of the subhalo's velocity with respect to the host halo at infall. When $V_{\rm tan}/V_{\rm tot} = 1$, the subhalo has a circular orbit, and when $V_{\rm tan}/V_{\rm tot} \ll 1$, the subhalo has a highly radial orbit. We define subhalos with $V_{\rm tan}/V_{\rm tot} \leq 0.2$ to have radial orbits because they are likely to travel through the host core and impact gravothermal evolution. A detailed reasoning behind this definition is provided in Section 5.4.1.

Each halo in our sample stands out for distinctive features in its evolution. For example, halos m10q-s70 and m10d-s70 both experience a major merger in the first ~ 2 Gyr of their evolution, which is then followed by a period of relatively slow mass accretion. In contrast, halo m10b-s70 experiences a nearly $1:1$ merger at 7.6 Gyr which, along with other concurrent mergers, causes the host mass to increase by a factor of two at a fairly late stage of evolution. This particular subhalo is also on a highly radial orbit with $V_{\rm tan}/V_{\rm tot} = 0.060$.

Halo m10f-s70 is distinctive for the large number of massive mergers that it experiences. In contrast, halo m10i-s70 has a more quiet accretion history, with the fewest mergers of all the halos considered here and none that would be classified as major. Halo m10j-s70 also has few mergers overall, but stands out for having a massive event at ~ 0.5 Gyr that is on a radial orbit with $V_{\rm tan}/V_{\rm tot} = 0.015$—the earliest subhalo on a radial orbit across all halos.

Section 5.4.1 provides $V_{\rm tan}/V_{\rm tot}$ compared to subhalo mass for all subhalos.

5.4.1 Subhalo Orbits

To highlight the rarity of massive subhalos on radial orbits, Figure 5.4 shows the normalized mass and tangential velocity of all subhalos with mass $m_{\rm sub}/M_{\rm host} \geq 0.01$ for all halos. The vertical dashed gray line indicates the tangential velocity below which a subhalo is expected to have travel through the host core. To calculate this expectation, we use an approximate relationship between eccentricity and tangential velocity: $1 - e^2 \approx V_{\rm tan}/V_{\rm tot}$, where e is the eccentricity of the subhalo orbit. Eccentricity is calculated as $e = (r_{\rm vir} - r_{\rm core})/(r_{\rm vir} + r_{\rm core})$ since the subhalo must have a minimum distance to the host of $r_{\rm core}$ after falling into the host at $r_{\rm vir}$ in order to travel through the host core. We calculate the eccentricity of each halo at the latest available snapshot and use the smallest, most conservative eccentricity to approximate the maximum to $V_{\rm tan}/V_{\rm tot}$ a subhalo that travels through the core can have. We find that subhalos with $V_{\rm tan}/V_{\rm tot} \leq 0.2$ travel through the host core.

While about half of the shown subhalos are on radial orbits, only two have masses such that $m_{\rm sub}/M_{\rm host} \geq 0.3$, as shown in the upper left corner of Figure 5.4. These subhalos correspond to the major mergers in halos m10b-s70 and m10j-s70. Notably, halos m10f-s70 and m10j-s70 experience the most subhalos on radial orbits. Halos m10b-s70, m10f-s70, and m10j-s70 are the three halos that do not undergo gravothermal collapse.

In conclusion, halos m10q-s70, m10d-s70, and m10i-s70 are early-forming halos with few massive mergers and few subhalos on radial orbits. Halos m10b-s70 and m10j-s70 are late-forming and each have a major merger on a radial orbit. Halo m10f-s70 is late-forming and has a large number of mergers, many of which are on radial orbits.

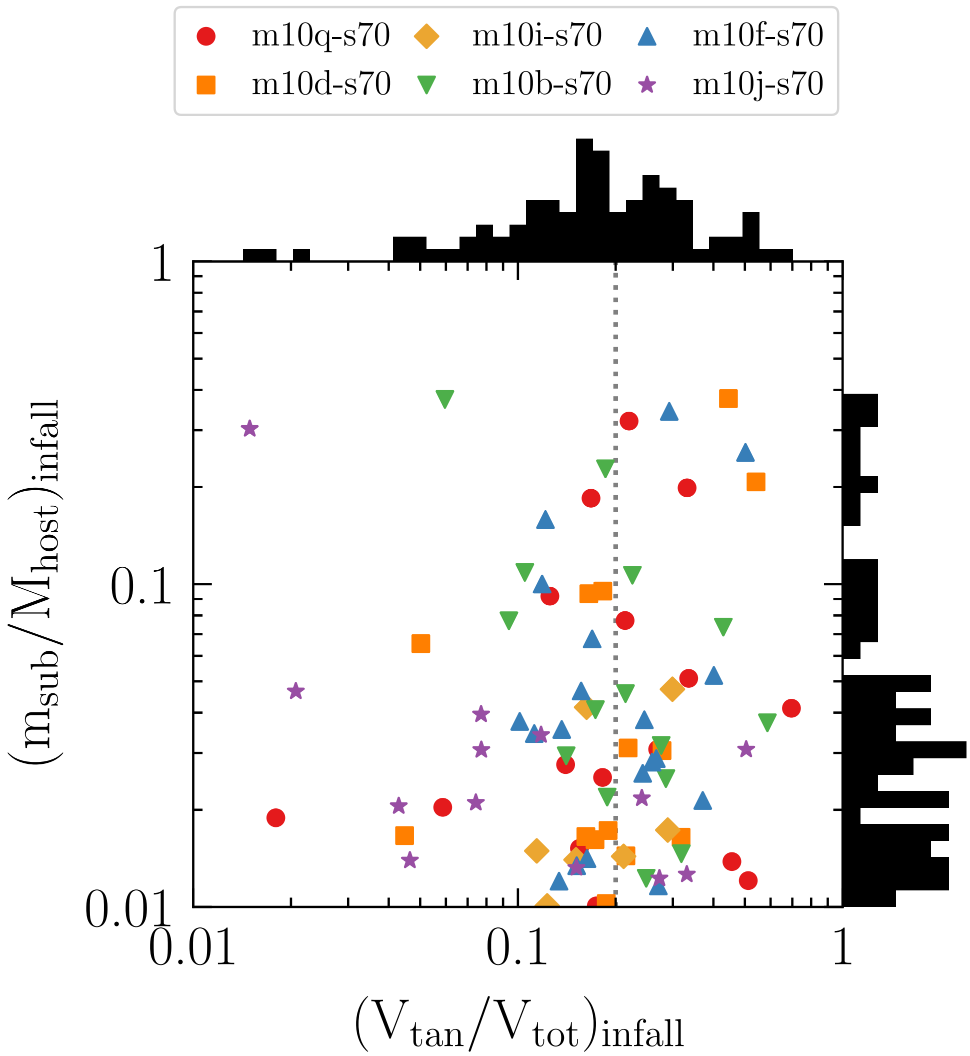

Figure 5.4: Subhalo mass, m_{sub}, and tangential velocity, V_{tan}, at infall. Mass is compared to the host halo mass, M_{host}, at the time of subhalo infall. Tangential velocity is normalized by the subhalo total velocity, V_{tot}, at infall. Radial orbits correspond to $V_{tan}/V_{tot} \ll 1$ and circular orbits correspond to $V_{tan}/V_{tot} \simeq 1$. Subhalos that may travel through the core are those in the left region with $V_{tan}/V_{tot} \leq 0.2$. Halos that are more massive compared to their host will have a larger impact on the host core. Two subhalos fall within this region and are considered major mergers ($m_{sub}/M_{host} \geq 0.3$). These halos fall into host m10b-s70 and m10j-s70. The right and top axes show histograms of the x and y values, respectively.

Halo	Name	σ/m [cm^2/g]	m_{DM} [$M_\odot$]	ϵ_{DM} [pc]	M_{host} [10^{10} $M_\odot$]	$t_{coll, model}$ [Gyr]
		Cross Section Scan				
m10q	m10q-CDM	0	1500	28	1.012	-
	m10q-s30	30	1500	28	0.988	17.61
	m10q-s70	70	1500	28	0.956	7.55
	m10q-s140	140	1500	28	0.823	3.77
		IC Scan				
m10b	m10b-CDM	0	3000	28	1.230	-
	m10b-s70	70	3000	28	1.252	9.57
m10d	m10d-CDM	0	3000	28	1.091	-
	m10d-s70	70	3000	28	1.039	5.34
m10f	m10f-CDM	0	3000	28	1.769	-
	m10f-s70	70	3000	28	1.330	6.94
m10i	m10i-CDM	0	3000	28	1.770	-
	m10i-s70	70	3000	28	0.958	2.32
m10j	m10j-CDM	0	3000	28	1.392	-
	m10j-s70	70	3000	28	1.086	2.37
		Subhalo-Host Scattering Scan				
m10b	m10b-s30	30	3000	28	1.178	22.32
	m10b-vdSIDM	$\sigma_0 = 147$ cm^2/g $w = 24$ km/s	3000	28	1.178	

Table 5.1: Summary of simulations generated in this work and their various parameters. The initial conditions for halo m10q were first introduced by Kim et al. (2013) and the initial conditions of the remaining halos were first introduced by Fitts et al. (2017). From left to right, the columns refer to: (1) Halo name; (2) Simulation name; (3) SIDM cross section over DM mass, σ/m; (4) Mass, $m_{\rm DM}$, of the high-resolution DM particles; (5) Plummer equivalent softening length, $\epsilon_{\rm DM}$, following the conventions used in Wheeler et al. (2019); Wetzel et al. (2023); (6) Bound virial mass of the host halo, $M_{\rm host}$, at the latest available timestep; and (7) Expected time at which the halo reaches gravothermal collapse, $t_{\rm coll}$, defined in Equation 6.2.

Name	**# of mergers**	**# of mergers**	$t_{\rm infall}$	$V_{\rm tan}/V_{\rm tot}$
	$(m_{\rm sub}/M_{\rm host} \geq 0.01)$	$(m_{\rm sub}/M_{\rm host} \geq 0.1)$	$(m_{\rm sub}/M_{\rm host} \geq 0.3)$	
m10q-s70	17	3	1.5 Gyr	0.220
m10d-s70	17	2	0.6 Gyr	0.445
m10i-s70	7	0	-	-
m10b-s70	17	4	7.6 Gyr	0.060
m10f-s70	20	5	0.6 Gyr	0.262
m10j-s70	13	1	0.5 Gyr	0.015

Table 5.2: Mergers of each host halo (m10q, m10d, m10i, m10b, m10f, and m10j) with $\sigma/m = 70$ cm^2/g . Columns show: (1) Simulation name; (2) Total number of mergers with infall mass greater than 0.01 $M_{\rm host}$; (3) Number of mergers with infall mass greater than 0.01 $M_{\rm host}$, referred to as massive mergers; (4) Infall time of major mergers, defined as those with infall mass greater than 0.3 $M_{\rm host}$; (5) Tangential velocity of major merger, normalized by total velocity, at infall. Halo m10f-s70 has the largest number of mergers with masses $m_{\rm sub}/M_{\rm host} \geq 0.01$ and > 0.1. Halos m10b-s70 and m10j-s70 have major mergers with the most radial orbits. These three halos are expected to have the largest impact from mergers.

Chapter 6

Gravothermal Core Collapse

In this Chapter, I introduce a fluid model for gravothermal collapse and compare it to subhalos with moderate cross sections ($\sigma/m = 1 - 5$ cm^2/g) and isolated halos with large cross sections ($\sigma/m = 30 - 140$ cm^2/g). I find that subhalos with moderate cross sections have not undergone gravothermal collapse, motivating large cross sections. Using larger cross sections of $30 - 140$ cm^2/g , I find that an isolated low-mass halo does undergo gravothermal collapse, with the level of collapse correlated both to cross section and time.

This chapter is based on research published in the Monthly Notices of the Royal Astronomical Society and in preparation for submission to the Astrophysical Journal. I use "we" throughout to acknowledge the joint contributions of myself (first author) and my co-authors.

6.1 The Fluid Model

Analytic and semi-analytic methods have proven to be efficient and illuminating tools to use alongside cosmological N-body simulations in the pursuit of constraining SIDM models because they run in a fraction of the time it takes to run full simulations. Outmezguine et al. (2023) present an analytic that describes the gravothermal collapse process in isolated SIDM halos in the long mean-free path regime and Gad-Nasr et al. (2023) extend this model into the short mean-free path regime. These methods model SIDM as a gravothermal fluid, following the work by Lynden-Bell & Wood (1968); Balberg & Shapiro (2002). The model has been tailored to isolated (Koda & Shapiro, 2011; Yang et al., 2023b; Jiang et al., 2023) and tidally stripped (Nishikawa et al., 2020) halos to predict SIDM halo evolution.

This formalism predicts that the time to gravothermal collapse is universal across initial conditions when normalized by the timescale:

$$t_{c,0} = \frac{2}{3\,a\,C}\left(\rho_{c,0}\,v_{c,0}\,\frac{\sigma}{m}\right)^{-1}. \tag{6.1}$$

Here $\rho_{c,0}$ is the halo's core density, $v_{c,0}$ is the halo's velocity dispersion, $a = 4/\sqrt{\pi}$, and C is an order-unity constant that depends on the heat conductivity and is obtained from fits to simulations. The '0' subscript indicates that the density and velocity dispersion pertain to the point of minimum density and maximum core size. Outmezguine et al. (2023) showed that $\rho_{c,0}$ and $v_{c,0}$ are correlated to the halo's initial NFW profile (Navarro et al., 1997). Thus, the evolution of an isolated SIDM halo may be predicted by an initial CDM profile. The time of collapse from the initial conditions is defined as:[1]

$$t_{coll} = 400\ t_{c,0}. \tag{6.2}$$

While analytic and semi-analytic models are computationally efficient, their effectiveness must be validated by comparisons to physical systems, such as N-body and hydrodynamic simulations.

[1] We use the constant 400 instead of 330, the value defined by Outmezguine et al. (2023), to account for the time before minimum density. This allows us to calculate collapse time with respect to the initial time rather than with respect to the time of minimum density, t_{core}.

To validate the analytic model for gravothermal collapse in isolated, idealized systems, Palubski et al. (2024) compares the analytic model to idealized N-body simulations of isolated low-mass halos of mass $\sim 10^9$ $M_{\odot}$. They find that isolated halos follow the expected collapse process in an SIDM model with $\sigma/m = 50$ cm^2/g when numerical challenges are minimized.

Using an analytic model for gravothermal collapse, Yang et al. (2025) developed a parametric model that predicts the gravothermal evolution of an SIDM halo from the properties of a corresponding CDM halo. They validate their model using halos in CDM and SIDM cosmological N-body simulations (Yang et al., 2023a; Nadler et al., 2023). While their model does well for isolated halos, they find their model is less successful deep in the collapse regime due to numerical issues and in subhalos that experience multiple pericentric passages due to increased tidal stripping.

Our research studies gravothermal core collapse of low-mass halos in cosmological environments using N-body simulations for the first time. We test the limits of the fluid model by comparing it to cosmological subhalos orbiting a MW-mass host as well as isolated halos. Although these halos (introduced in Chapter 5) are considered isolated because they are not subhalos of a more massive system, they do experience merger events with subhalos of masses up to 0.4 times the host mass.

6.2 Core Expansion in Low-Mass Subhalos with Moderate Cross Sections

In a DM model with a small cross section ($\sigma/m = 1$ cm^2/g), DM particles undergo fewer collisions than in a model with a larger cross section ($\sigma/m = 5$ cm^2/g). Thus, subhalos in our S1 simulation undergo less mass loss due to host and subhalo particle interactions (as seen in Figure 3.7). One might expect S1 subhalos to be more dense than, or at least as

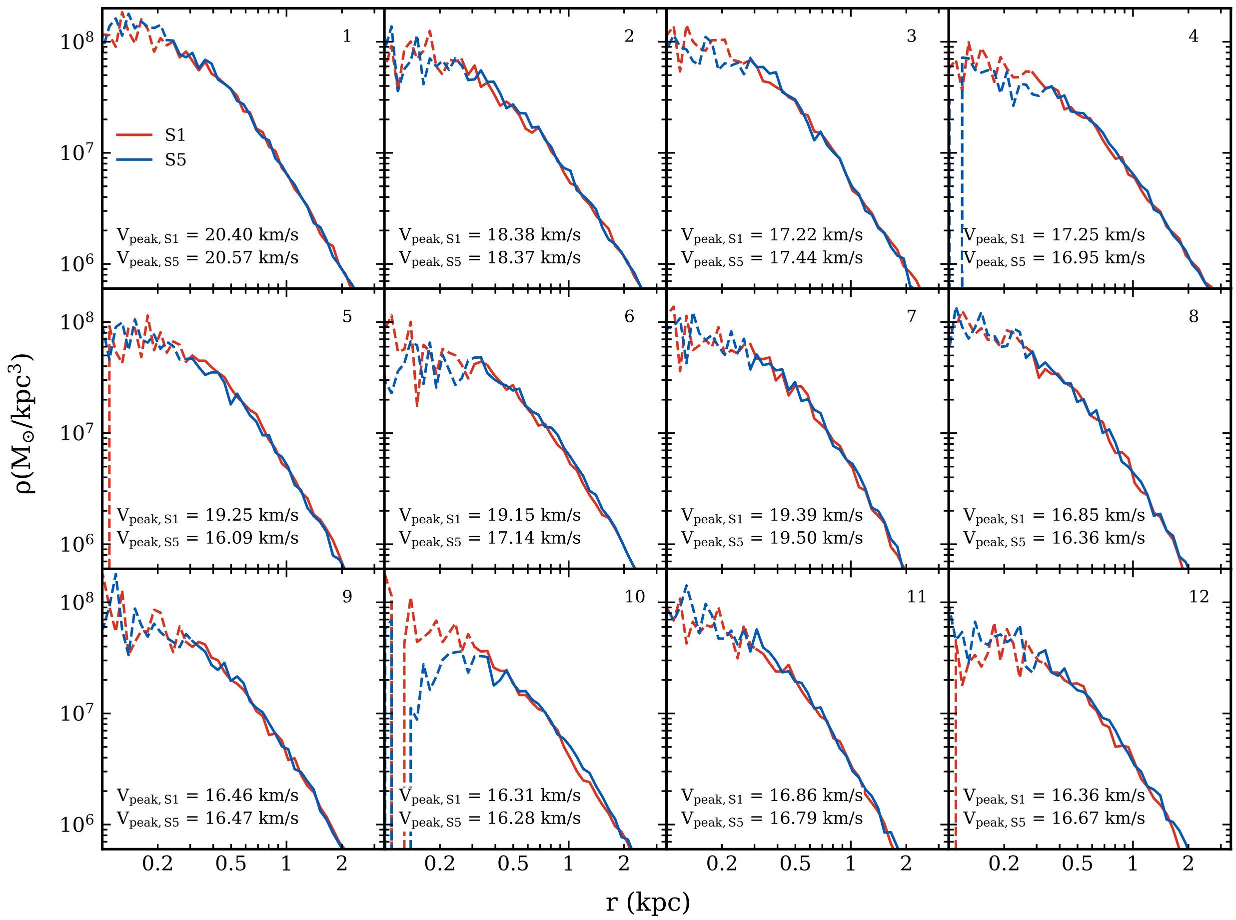

Figure 6.1: Density profiles for 12 pairs of matching subhalos from the S1 and S5 simulations. Pairs are found by maximizing equation 6.3 and only using pairs with $\xi > 0.3$. Dashed lines show unresolved regions (with less than 200 particles). Pairs are ordered from largest to smallest $V_{\max}$ of the S1 halo pair. V_{peak} values for both subhalos are given in the bottom left of each subplot and the values for $V_{\max}$, and $r_{\max}$ are given in Table 6.1.

Pair #	$V_{\max}$ (km/s)		$r_{\max}$ (kpc)		r_{peri} (kpc)	
	S1	S5	S1	S5	S1	S5
1	18.41	18.59	1.02	0.94	48.40	47.84
2	16.64	17.06	1.65	1.41	77.50	80.40
3	16.60	16.49	0.94	0.94	88.04	92.05
4	16.22	16.38	1.79	1.52	113.81	67.77
5	15.74	15.31	1.02	1.02	56.06	55.00
6	15.67	16.31	1.30	1.41	59.46	75.65
7	15.63	15.74	1.02	1.11	52.27	53.14
8	14.75	14.86	0.94	1.11	64.35	69.08
9	14.62	14.74	1.11	1.02	69.88	73.90
10	14.28	14.56	1.02	1.52	96.97	101.75
11	13.55	13.88	0.94	0.94	38.94	39.88
12	12.83	13.29	1.20	1.41	54.77	63.23

Table 6.1: $V_{\max}$, $r_{\max}$, and pericenter values for the S1 and S5 subhalo pairs shown in Figure 6.1. The subhalos' pair number is given based on S1 $V_{\max}$ and is shown in the top right corner of Figure 6.1. Pairs are selected by maximizing ξ, a value that quantifies the number of particles that two subhalos share, and we only show pairs with $\xi > 0.3$.

dense as a subhalo in the S5 simulation with similar initial conditions and orbit.

Another physical process called gravothermal core collapse (Zel'dovich & Podurets, 1966; Lynden-Bell & Wood, 1968; Larson, 1970; Lightman & Shapiro, 1978; Shapiro & Teukolsky, 1985) may also affect the densities of subhalos in our simulations. Through heat transfer to the colder, central regions of subhalos, core collapse increases the central densities of subhalos while decreasing the radius of the core (Hachisu et al., 1978; Lynden-Bell & Eggleton, 1980; Balberg et al., 2002; Balberg & Shapiro, 2002; Koda & Shapiro, 2011). This is especially pertinent in DM models with large cross sections (≥ 5 cm^2/g) at small velocities (order $V_{\max}$) (Nishikawa et al., 2020; Turner et al., 2021). Core collapse is dependent on subhalo concentration, orbit, and DM self-interaction cross section (Kahlhoefer et al., 2019; Sameie et al., 2020b). Furthermore, core collapse may cause the central densities of subhalos in models with large cross section to be larger than corresponding subhalos in models with small cross section (see Kahlhoefer et al. (2019) Figure 1).

In this section, we aim to determine whether subhalos in our S5 simulation have undergone core collapse. In Section 6.2.1 we match S1 subhalos to the S5 subhalos that have the most similar initial conditions. We find, however, that our resolution is not sufficient to make conclusions about core collapse. In Section 6.2.2, to explore subhalo densities within the resolution limit, we utilize an isothermal model. After confirming that the model correctly predicts subhalo densities in resolved regions, we use the model to extrapolate our density profiles to lower radii.

6.2.1 Matching Low-Mass Subhalos with Moderate Cross Sections

To determine if core collapse is playing a major role in our simulations, we look at direct comparisons of subhalos in the S1 simulation and the S5 simulation. To find these halo matches, we look at only the 30 subhalos within the outer region of the host halo (between 50 kpc and $R_{\rm vir,host}$) with largest $V_{\rm peak}$, and compare subhalos in two ways. First, we look at the coordinate position of the subhalos at accretion, and evaluate matches assuming that corresponding subhalos would have similar accretion histories.

Second, we look at the particles within each subhalo, which are flagged with a unique ID number. Since the S1 and S5 simulations were run from the same initial conditions, corresponding subhalos in both simulations should share many particles. We quantify the amount of shared particles using the equation:

$$\xi = \frac{N_{\rm shared}^2}{N_1 N_2} \tag{6.3}$$

where N_1 and N_2 are the number of particles in each subhalo, and $N_{\rm shared}$ is the number of particles that are shared between the two subhalos (Knollmann & Knebe, 2009). To find subhalo pairs, we maximize this quantity and only look at pairs with $\xi > 0.3$. All of the pairs that we find have $0.3 < \xi < 0.55$.

Under these conditions, we found 12 pairs of subhalos. A more extensive search through all subhalos to find more pairs may be insightful in the future, but was not necessary for the analysis presented in this work.

With the subhalo pairs, we are able to compare how subhalos evolve in the S1 versus the S5 simulation. To compare the potential mass loss and core collapse in each model, we look at the z=0 density profiles. Figure 6.1 shows the local density in spherical shells of each of the 12 pairs of subhalos. The S1 subhalos are in red and the S5 subhalos are in blue. The pairs are ordered from largest to smallest $V_{\max}$ of the S1 subhalo and the $V_{\max}$, $r_{\max}$ and $r_{\rm peri}$ are given in Table 6.1. The solid line shows fully resolved areas of the density profile, while dashed lines indicate unresolved ($\leq$ 200 particles) radii.

Figure 6.1 shows that the density profiles of an S1 and S5 pair are very similar. All pairs have the same profile outside about 0.5 kpc, and only one pair, pair 10, differs significantly within 0.5 kpc. With the given resolution, we speculate that this subhalo pair had an orbit with few and far pericentric passages and has a low concentration such that neither subhalo underwent core collapse. Indeed, we confirmed that this subhalo pair has the largest pericenter of all 12 pairs.

From Figure 6.1 we conclude that no subhalos in the S5 simulation that we have explored are undergoing core collapse to the extent that their densities increase to be larger than their S1 pair. We do see that some subhalos may have started to undergo core collapse more than others. For example subhalo pair 10, with the largest pericenter, doesn't seem to have undergone any core collapse, versus subhalo pair 11, with the smallest pericenter, where we see that the S5 subhalo density is at least as large at its S1 pair. However, we are limited by resolution at small radii.

The density profiles show no difference between S1 and S5 subhalos at the radii that are resolvable in our simulations ($r > 0.25$ kpc), indicating that our subhalos have not undergone

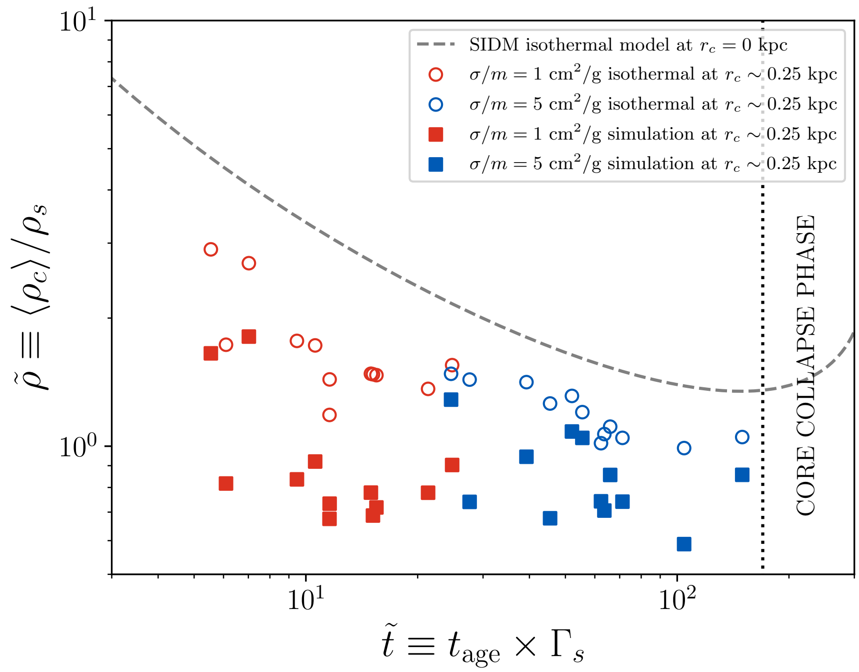

Figure 6.2: Average core density as a function of time. The squares show the densities and timescales of the subhalo pairs in the S1 (red) and S5 (blue) simulations. The circles show the predicted densities and timescales of the subhalo pairs, calculated from their $V_{\rm max}$ and $r_{\rm max}$ values. For both the squares and circles, we define the core radius, $r_{\rm c}$, as the innermost resolved radius, which is about 0.25 kpc. The dashed grey line shows the density at the center (r=0) of a subhalo predicted by the isothermal model. On the right side of the plot, we identify the times for which a subhalo has entered the core collapse phase, identified by an upturn in the dashed line. In this phase the core density of the subhalo increases.

core collapse.

6.2.2 Core Density Extrapolation Using an Isothermal Model

In our SIDM simulations, we are limited by resolution and not able to make conclusions from the inner areas of subhalos, specifically, within about 0.25 kpc. Instead, we use an isothermal model to explore the central densities of subhalos in both SIDM models. We are particularly interested in two aspects of the central densities. First, from the central densities we determine whether our SIDM subhalos have entered the core collapse phase. We then compare the central density profiles to observed dSphs to address the TBTF problem

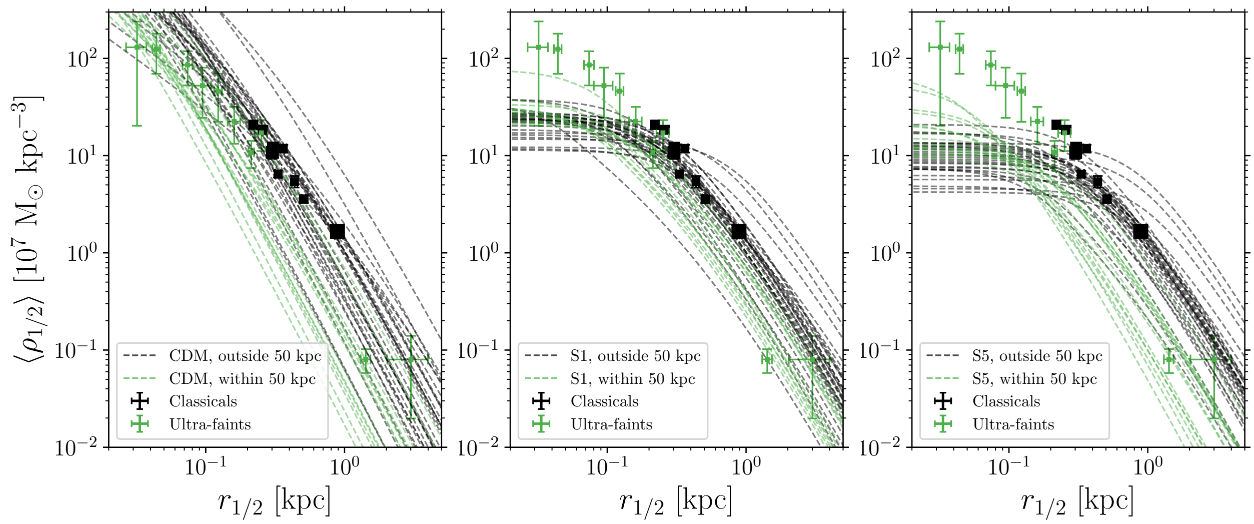

Figure 6.3: Mean density profiles of 30 resolved subhalos outside 50 kpc with largest V_{peak} (black) and all resolved subhalos within 50 kpc (green) in our S1 (middle) and S5 (right) simulation. From the CDM simulation (left), we show mean density profiles of 30 resolved subhalos outside 50 kpc with largest V_{peak} (black) and 15 resolved subhalos within 50 kpc with largest V_{peak} (green). Densities are calculated from an isothermal model with the V_{max} and r_{max} values from the simulations. We compare to the mean density and half-light radius of classical (black) and ultra-faint (green) dSphs. The size of the black squares is given by the luminosity of that dSph.

highlighted in Kaplinghat et al. (2019).

The isothermal model that we use is described in detail in Kaplinghat et al. (2014) (see also Kaplinghat et al. (2016)). This model has been tested extensively by Robertson et al. (2020) who find it to be surprisingly accurate for SIDM models similar to ones we use in this work. We fit this isothermal model to our subhalos using their V_{max} and r_{max} values.

Figure 6.2 shows the average core density and how close our subhalo pairs are to the core collapse phase. The red squares show the density and timescales for the S1 subhalo pairs, and the blue squares show those for the S5 subhalos. Due to resolution constraints, the core density for our simulated subhalos is taken at the smallest radius at which both subhalos in a pair enclose at least 200 particles, which is about $r_{\text{c}} = 0.25$ kpc. The y-axis is the average core density divided by ρ_{s}, which is taken to be $\rho_{\text{s}} = 1.721 V_{\text{max}}^2 G^{-1} R_{\text{max}}^{-2}$ (Kaplinghat et al., 2019). The x-axis is the age of the subhalo, taken to be 10 Gyr, multiplied by the scattering rate, which is $\Gamma_{\rm s} = a\frac{\sigma}{m}v_0\rho_{\rm s}$ where $a = \sqrt{16/\pi}$, the velocity scale is $v_0 = \sqrt{GM_0/r_{\rm s}}$, and the mass scale is $M_0 = 4\pi r_{\rm s}^3\rho_{\rm s}$ (Koda & Shapiro, 2011; Nishikawa et al., 2020).

The circles show the average density at the core radius and timescale for the S1 and S5 subhalo pairs, predicted by the isothermal model. We calibrate the isothermal model using each subhalo's $V_{\rm max}$ and $r_{\rm max}$ values, and we plot the average density at that subhalo's $r_{\rm c}$.

Figure 6.2 shows that the isothermal model predicts average core densities that are slightly larger than the simulated subhalo core densities. The modeled and simulated subhalo densities agree better when only looking at the local density at $r_{\rm c}$ rather than the average density. The difference in average core density is thus due to differences in the density profiles in the central regions of the subhalos. This is likely due to the isothermal model deviating slightly from the subhalo density profile. An example of this can be seen in the right panel of Figure 4 in Robles et al. (2019), which compares the density profiles of subhalos in the S1 simulation to the isothermal model. A more robust comparison between model and simulations in central the regions will be possible with higher resolution simulations.

On average, the model predicts larger core densities by up to a factor of about 2. This systematic error goes in the direction of making the densities predicted by the analytic model larger. We take this into account when we derive our conclusions regarding ultra-faint satellites.

The dashed grey line shows the density evolution of the isothermal model at $r = 0$ kpc. Because this shows the density at a different radius as the data points, they should not be directly compared. Rather, we show the density evolution of the isothermal model at r=0 to highlight the general trend of the density evolution; subhalos further along in their core collapse timescales have lower average core densities. Additionally, we can use the time at which the isothermal model at r=0 begins to increase in density to estimate the time at which subhalos will enter the core collapse phase. This occurs when a subhalo's core density begins increasing. This is shown in Figure 6.2 as the region to the right of the dotted black line.

Figure 6.2 shows that no subhalos have entered the core collapse phase. This confirms that none of our subhalo pairs should show that the core density of the S5 subhalo is much larger than that of its S1 counterpart.

To determine whether a difference in core radii could be observed in Figure 6.1 we calculated the core radius, as defined by Kaplinghat et al. (2014), using the isothermal model. We find that the S5 subhalos have slightly larger core radii than their S1 pair. The predicted core radii for S1 subhalos lie between $0.15 - 0.23$ kpc, while the core radii of the S5 subhalos lie between $0.21 - 0.33$ kpc. Since the model predicts about a factor of two larger core densities, it likely also predicts smaller core radii. A small shift in core radii, even for radii up to 0.5 kpc would not be easily visible in Figure 6.1. It is expected that core radii depend weakly on cross section for these subhalos, as is shown by the weak dependence on cross section of core density shown in Figure 6.2.

Figure 6.3 shows the average density profiles from the isothermal model based on $V_{\rm max}$ and $r_{\rm max}$ values of subhalos in the S1 and S5 simulations (middle and right panels). We additionally show the average density profiles of subhalos in the CDM simulation (left panel). We show the profiles for the 30 subhalos currently outside 50 kpc with largest $V_{\rm peak}$ that are resolved at $r_{\rm max}$ (black dashed) and all subhalos currently within 50 kpc that are resolved at $r_{\rm max}$ (green dashed). Since CDM contains many resolved subhalos within 50 kpc, we show only those with the 15 largest $V_{\rm peak}$ values. We compare these to the half-light radius and average density at half-light radius of the classical and ultra-faint dSphs that we have been using throughout this paper.

In the left panel of Figure 6.3, we see that CDM subhalos can explain all of the classical and ultra-faint dSphs well. However, there are a few massive simulated halos that should have created galaxies that we do not observe. This illustrates a tension, known as the TBTF problem; these subhalos are too big to fail at forming galaxies, yet we do not observe such galaxies.

While S1 and S5 somewhat alleviate the TBTF problem associated with classical dSphs, they both have trouble reproducing the high densities seen in the smallest ultra-faint dSphs. The S1 subhalos in the middle panel of Figure 6.3 can explain the observed classical dSphs because the most massive subhalos have large enough cores to host classical dSphs with small half-light radii. However, there are not enough subhalos that are dense enough to host all of the ultra-faint dSphs with $r_{1/2} < 200$ pc. The S5 simulation is even more discrepant with the ultra-faint population: there are four ultra-faint dSphs that are denser than *any* of the simulated subhalos.Additionally, at least two of the classical dSphs that are in tension with the subhalo velocity profiles (Figure 4.3) are also denser than the simulated subhalos in the S5 simulation. This tension is exacerbated by the fact that the isothermal model over predicts the average density of simulated subhalos by a factor of about two.

Some values for mean density of dSphs may be updated as their binary fractions are taken into account. Using multi-epoch observations and Bayesian analysis, the binary fraction has been taken into account when calculating the velocity dispersion of Sculptor (Minor, 2013), Fornax (Minor, 2013), Carina (Minor, 2013), Sextans (Minor, 2013), Leo II (Spencer et al., 2017), Boötes I (Koposov et al., 2011), and Segue I (Martinez et al., 2009), but it remains to be done for others. Accounting for binary systems may change velocity dispersion, especially of ultra-faint dSphs (Minor et al., 2010; McConnachie & Côté, 2010), which affects the mean density and relative error of some dSphs, possibly decreasing the tension in Figure 6.3.

Neither of our SIDM models are sufficient to explain both the classical and ultra-faint dSphs. An SIDM model with cross section significantly greater than 5 cm^2/g may be able to explain both the classical and ultra-faint dSphs with dense cores if some of the subhalos undergo core collapse. In a model with a large cross section, we anticipate that some of the outer subhalos will form larger cores, *and* many subhalos will core collapse. A sharp velocity dependence to reduce mass loss in halo-subhalo dark matter scattering would likely be necessary to allow core collapse to proceed (Zeng et al., 2021). Core collapsed subhalos may have cores dense enough to be compatible with the smallest ultra-faint dSphs. It would be interesting to test these expectations by running a Milky Way-like N-body simulation with a velocity dependent cross section that is greater than 5 cm^2/g at the subhalo circular velocity scale.

We conclude that neither the S1 nor the S5 simulations formed subhalos that are compatible with all the observed dSphs. Using an analytic model as an upper bound for the subhalo central densities, we predict that with a cross section at $V \approx V_{\rm max}$ of a factor of few larger, many subhalos would be in the core collapse phase and have large enough central densities to be consistent with the densest dSphs. This would require a sharp velocity dependence such that the effective cross section at orbital velocities ($V \sim 200$ km/s) is below ~ 1 cm^2/g to reduce mass loss from halo-subhalo dark matter scattering.

6.3 Core Collapse in Low-Mass Halos with Large Cross Sections

Throughout this work, we use halo density to characterize the impact of DM self interactions on halo evolution. To demonstrate how the density profile of an SIDM halo changes with time and cross section, this subsection walks through the example of halo m10q as it evolves towards gravothermal collapse.

The impact that self-interactions have on halo density and circular velocity profiles depends on the number of self-interactions that particles experience. The probability that an SIDM

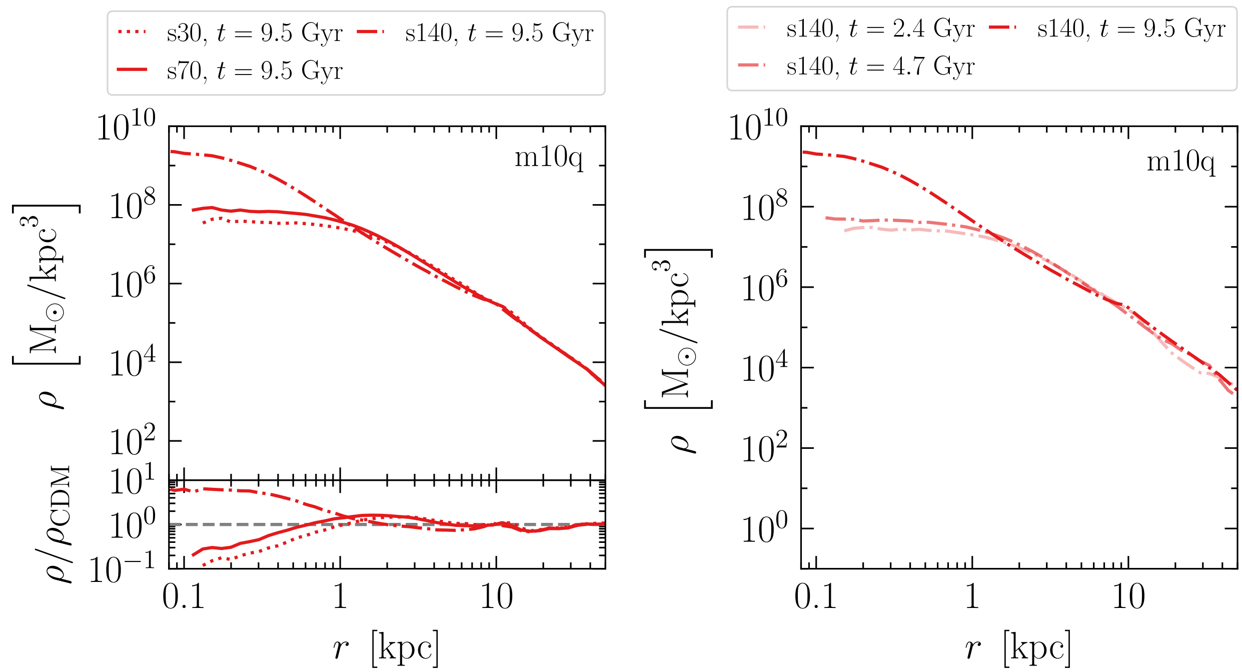

Figure 6.4: Density profiles of the m10q host halo with three different DM models: SIDM with cross sections $\sigma/m = 30$ (dotted red), 70 (solid red), and 140 (dot-dashed red) cm^2/g . Profiles are shown at three different times: 9.5 (dot-dashed red with $\alpha = 1$), 4.7 (dot-dashed red with $\alpha = 0.6$), and 2.4 Gyr (dot-dashed red with $\alpha = 0.3$). These times were chosen to replicate the difference between s140, s70, and s30. The bottom of the left panel shows the SIDM profiles compared to the CDM profile at $t = 9.5$ Gyr. The left and right panels show similar profiles although cross section is varied on the left and time is varied on the right. Halos m10q-s30 at $t = 9.5$ Gyr and m10q-s140 at $t/4 \approx 2.4$ Gyr have low density extended cores; halos m10q-s70 at $t = 9.5$ Gyr and m10q-s140 at $t/2 \approx 4.7$ Gyr have extended cores with core densities larger than the low cross section/early time profile; and halo m10q-s140 at $t = 9.5$ Gyr has a high-density, collapsed core. Profiles are only shown for radii enclosing at least 200 particles.

particle scatters is given by

$$P_{\text{scatter}} = 1 - \exp\left(-\int_0^{t_{\text{age}}} \rho \frac{\sigma}{m} V_{\text{rel}}\, dt\right), \tag{6.4}$$

where V_{rel} is the relative velocity between interacting particles. Within a halo of set mass and concentration, ρ and V_{rel} are fixed, so the number of interactions depends on σ/m and t_{age}, such that changing σ/m by a factor of two should yield the same results as changing the time by a factor of two.

The left panel of Figure 6.4 shows the DM density profile, $\rho(r)$, for the m10q halo at $t_{\text{age}} =$ 9.5 Gyr for varying SIDM cross section. The density is calculated as the mass per volume in 60 logarithmically spaced spherical shells. Profiles are only shown for radii that enclose at least 200 particles. The ratio of the SIDM density profile relative to its corresponding CDM density profile is shown in the bottom panel.

All halos have approximately the same density profile (to within $\sim 1\%$) outside ~ 1 kpc. In the central region of the host, halo m10q-s30 has a low-density core that extends to ~ 1 kpc, as expected of the core-expansion phase. Halo m10q-s70 has a slightly higher-density core that extends to ~ 1 kpc, which indicates that the halo has entered the core-collapse phase. Halo m10q-s140 has a high-density core, about an order-of-magnitude more dense than CDM at ~ 0.1 kpc, which extends to ~ 0.2 kpc and quickly falls off to match the other simulations at ~ 1 kpc. This halo is deep in the core-collapse phase.

The right panel of Figure 6.4 shows more density profiles for halos in the suite. For these examples, the SIDM cross section is fixed to 140 cm^2/g and the time is varied. Note that the density profile for m10q-s30 at 9.5 Gyr aligns with that of m10q-s140 at 2.4 Gyr. Similarly, the profile for m10q-s70 at 9.5 Gyr aligns with that of m10q-s140 at 4.7 Gyr. This correspondence is not coincidental; it arises because the halo density depends on the number of self interactions experienced by the simulation particles, which is directly proportional to the product of cross section and time as specified in Equation 6.4. Because the ratio of σ/m between 30 and 140 cm^2/g is $\sim 1/4$ and between 70 and 140 cm^2/g is 1/2, the profiles are shown at $9.5/4 \approx 2.4$ Gyr and $9.5/2 \approx 4.7$ Gyr. The striking similarity between the left and right panels confirms that varying σ/m has the same effect on halo profiles as varying time.

Figure 6.4 shows that all halos have approximately the same density profile (to within $\sim 1\%$) outside ~ 1 kpc. In the central regions, the profiles with fewer interactions (S30 at 9.5 Gyr and S140 at 2.4 Gyr) have low-density cores that extend to ~ 1 kpc, as expected of the core-expansion phase. The profiles with moderate interactions (S70 at 9.5 Gyr and S140 at 4.7 Gyr) have slightly higher-density cores that extend to ~ 1 kpc. This indicates that the halo has entered the core-collapse phase. The profile with many interactions (S140 at 9.5 Gyr) has a high-density core, about an order-of-magnitude more dense than CDM at ~ 0.1 kpc, which extends to ~ 0.2 kpc and quickly falls off to match the other simulations at ~ 1 kpc. This halo is deep in the core-collapse phase.

The density profiles of CDM and SIDM halos are expected to change when the baryonic disc and bulge are accounted for (Fitts et al., 2017) because the DM density is dependent on the baryonic gravitational potential (Kaplinghat et al., 2014). Using a cross section of 1 cm^2/g , Robles et al. (2017) find that the density profiles of m10b, m10d, and m10f are similar when run with SIDM DMO and SIDM with FIRE-2 hydrodynamics. However, with larger cross sections of $30 - 140$ cm^2/g , we expect the energy injection due to baryonic feedback to increase the scatter in the DM profiles. Future work will detail the density profiles of SIDM halo in simulations that include full FIRE-2 hydrodynamics.

Thus, we conclude that halo m10q is early in the gravothermal collapse phase by 9.5 *Gyr if* $\sigma/m = 70$ *cm^2/g and is deep in the gravothermal collapse phase by* 9.5 *Gyr if* $\sigma/m = 140$ *cm^2/g . We confirm that the same conclusions are true if time is varied rather than cross section.*

Chapter 7

The Impact of Mergers on Gravothermal Collapse

In this Chapter I explore the impact that mergers have on gravothermal evolution. I show that three halos, with quiet merger histories, collapse within a Hubble time, while three halos, with massive or frequent mergers (as described in Chapter5) do not collapse. I show that the halos that do not collapse experience periods where heat is transferred into the core, delaying collapse. Finally, I show that these cosmological simulations with $\sigma/m = 70$ cm^2/g produce halos that have a diversity of core density that ranges over 2 orders of magnitude.

This chapter is based on research in preparation for submission to the Astrophysical Journal. I use “we” throughout to acknowledge the joint contributions of myself (first author) and my co-authors.

7.1 Core Density Evolution

This section explores in detail the density evolution of the low-mass halos simulated in this work. The main results are summarized in Figure 7.1, which shows the core density of each host halo as a function of time. The arrows along the horizontal axis indicate the infall time and mass of the most significant mergers and are identical to those in Figure 5.3.

Since $r = 0$ of the halo is not resolved, we calculate the core density by fitting the inner density profile to an analytic profile. Following the method described in Palubski et al. (2024), we first calculate the core center-of-mass using 0.67% $N_{\rm vir}$ particles (where $N_{\rm vir}$ is the number of particles within $r_{\rm vir}$) with the smallest SIDM kernel radius, $h_{\rm s}$. As described in Section 5.1, $h_{\rm s}$ is calculated such that it encloses 32 nearest neighbors. Thus, particles with small $h_{\rm s}$ have the largest local DM density. The core density is obtained by fitting $\rho_{\rm c}$ and r_0 to the profile

$$\rho(r) = \rho_{\rm c} \left(1 + \left(\frac{r}{r_0}\right)^2\right)^{-3/2} , \tag{7.1}$$

where ρ_c is the core density and r_0 is analogous to the scale radius where the slope of the log profile becomes -3.

It is crucial to center around the core rather than the halo for this calculation because the center-of-mass of the core is not the same as the center-of-mass of the entire halo (Palubski et al., 2024). For example, in the most extreme case, halo m10q-s70, the core density calculated by centering on the halo is an average across time of 0.73 times the core density calculated by centering on the core.

The top row of Figure 7.1 shows how the core evolves for the early-forming halos (m10q-s70, m10d-s70, and m10i-s70). In each case, the core density initially decreases until it achieves a minimum when the core radius is maximal. This point is indicated by time $t_{\rm core}$ and

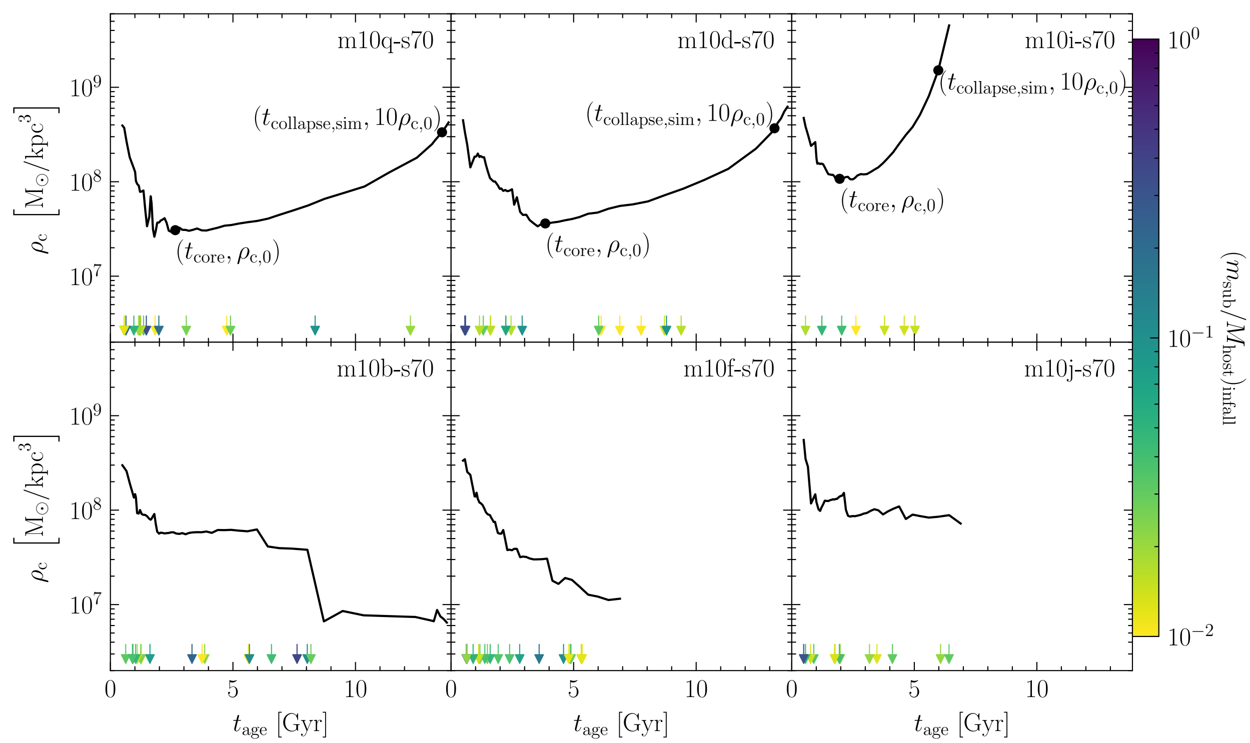

Figure 7.1: Core density of each host halo (m10q, m10d, m10i, m10b, m10f, and m10j) with $\sigma/m = 70$ cm^2/g across time. The infall times for the most significant mergers are indicated by the arrows along the horizontal axis with the colors corresponding to $\rm m_{sub}/M_{host}$ at infall, identical to Figure 5.3. Early-forming halos (top row) show an early core expansion phase that ends at $(t_{\rm core}, \rho_{\rm c,0})$, followed by the gravothermal collapse phase where core density increases. We define a halo as collapsed when the core density reaches $10\rho_{\rm c,0}$. The late-forming halos (bottom row) show a continually decreasing core density. These halos do not experience gravothermal collapse.

core density $\rho_{c,0}$. After that point in time, the density rapidly increases as the halo enters the core-collapse phase. We define the time it takes a halo to collapse, t_{collapse} as the time at which the core density reaches $10\rho_{c,0}$. Since the analytic definition for collapse time, $r_{\text{core}} \rightarrow 0$ and $\rho_c \rightarrow \infty$, is impossible to achieve in N-body simulations, we use $10\rho_{c,0}$ as a realistic marker for collapse. Halos m10q-s70 and m10d-s70 start collapsing at $\sim$ 4 Gyr and reach a core density of 10 times the minimum value at $\sim$ 13.7 Gyr. Halo m10i-s70 enters the collapse phase at $\sim$ 2 Gyr and reaches a core density of 10 times its minimum at $\sim$ 6 Gyr.

The bottom row of Figure 7.1 shows how the core evolves for the late-forming halos (m10b-s70, m10f-s70, and m10j-s70). These three halos are noteworthy as they do not undergo gravothermal core collapse. Based on these halo's CDM counterparts, they are expected to collapse within the age of the universe (see Section 8 for more details), so these halos should exhibit some (if not complete) collapse over their lifetime. Instead, the core density continually decreases in all three cases. The result for m10b-s70 is particularly striking, with a decrease in core density of almost two orders of magnitude.

To explain these trends, Section 7.2 considers the impact of mergers on the direction of heat flow at the core region of the host halos. Section 7.3 explores the impact of subhalo-host SIDM interactions, using halo m10b as a case study. Chapter 8 then compares the numerical results with semi-analytic predictions for the core evolution, demonstrating that the presence of mergers in a full cosmological treatment does not reproduce the predictions of these models.

7.1.1 Core Radius

Figure 7.2 shows the core radius of halos m10i-s70, m10j-s70, m10b-s70, m10d-s70, m10q-s70, and m10f-s70 across time. The core radius is calculated as the radius where the density falls to 1/2 the central density. This is calculated using the analytic profile described by equation 7.1

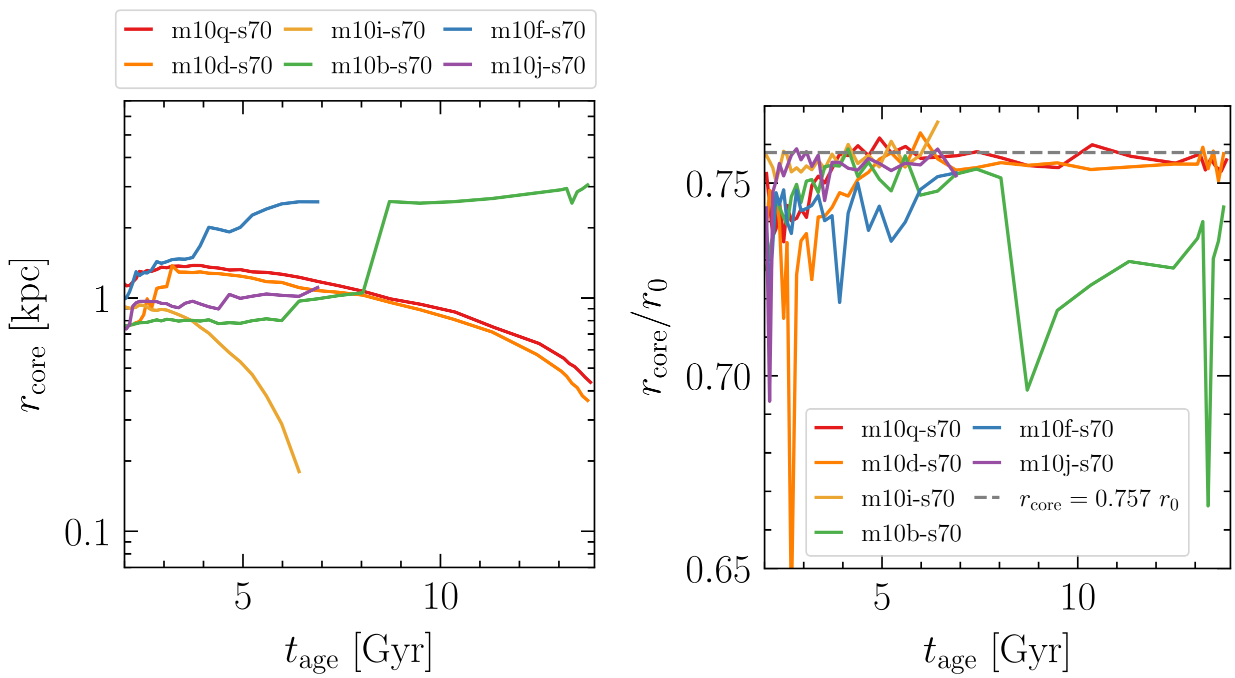

Figure 7.2: *(Left)* Core radius of each host halo (m10i, m10j, m10b, m10d, m10q, and m10f) with $\sigma/m = 70$ cm^2/g across time. Core radius is defined as the radius at which the fit analytic density falls to 1/2 the central density. Halos that undergo gravothermal collapse (m10q-s70, m10d-s70, and m10i-s70) have a decreasing $r_{\rm core}$ at late times, while those that don't (m10b-s70, m10f-s70, and m10j-s70) have a constant or increasing $r_{\rm core}$. *(Right)* Core radius normalized by r_0 of each host halo with $\sigma/m = 70$ cm^2/g across time. r_0 is calculated using equation 7.2. Halos with isothermal cores follow the predicted relationship, $r_{\rm core}/r_0 = 0.757$ (dashed gray), while halos with major or frequent mergers have smaller core radii compared to r_0. Radii are only shown after 2 Gyr since early halos are not expected to form isothermal cores.

fitted to each halo. Halos m10i-s70, m10q-s70, and m10d-s70 undergo gravothermal core collapse, which is evident from the decrease in their core radii. Halos m10b-s70, m10f-s70, and m10j-s70 do not undergo gravothermal collapse, as is evident from their increasing or constant core radii.

The right panel of Figure 7.2 shows the core radius normalized by the scale radius, r_0. The scale radius is calculated as

$$r_0 = \frac{3v_{\rm c}}{\sqrt{4\pi G\rho_{\rm c}}}, \tag{7.2}$$

where $v_{\rm c}$ is the one-dimensional velocity dispersion within the core radius and $\rho_{\rm c}$ is the core density. Analytic isothermal profiles predict $r_{\rm core}/r_0 = 0.757$.

Halos m10q-s70, m10q-s70, and m10i-s70 follows the predicted ratio after early mergers, as expected for halos with few disruptive mergers. Halo m10j-s70 follows the predicted ratio well although this halo does not experience gravothermal collapse. This may indicate that halo m10j-s70 is approaching gravothermal collapse. Halos m10b-s70 and m10f-s70 fall below the predicted ratio, indicating the profile does not have an isothermal core. These halos experience frequent and major mergers that inject heat into the core, as seen in Figure 7.3.

7.2 The Impact of Mergers on Heat Flow

Previous work has shown that major mergers, defined as mergers with $\rm M_{sub}/M_{host} \geq 1/3$, impact the DM vertical acceleration profile (Chakrabarti et al., 2019, 2020; Arora et al., 2024), halo orientation with respect to the disk (Baptista et al., 2023), disk formation (Springel, 2005; Robertson et al., 2006; Sparre & Springel, 2017), and the shapes of halos (Wang et al., 2019). In particular, Arora et al. (2024) find that major mergers can have larger impacts on the vertical acceleration profile than the differences between CDM and SIDM with a low

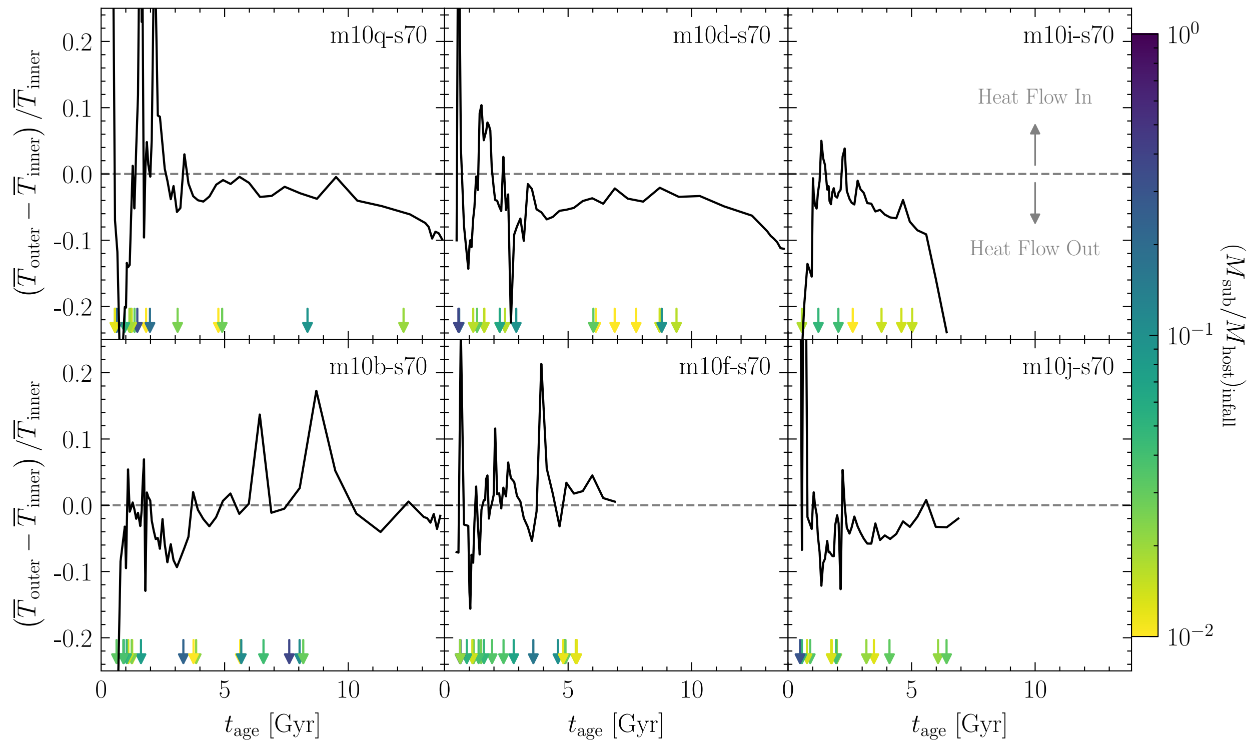

Figure 7.3: Difference in average temperature between the inner and outer regions of each host halo (m10q, m10d, m10i, m10b, m10f, and m10j) with $\sigma/m = 70$ cm^2/g , shown as a function of time. The average temperature is defined in Equation 7.3, with $\overline{T}_{\rm inner}$ corresponding to the volume within 1 kpc and $\overline{T}_{\rm outer}$ corresponding to the volume from 1–5 kpc of the halo center. Fractional temperature differences that are positive (negative) correspond to heat flowing in (out) of the central region of the halo. Similar to Figure 5.3, the infall times for the most significant mergers are indicated by the arrows along the horizontal axis with the colors corresponding to $M_{\rm sub}/M_{\rm host}$ at infall. Gravothermal collapse is correlated with the direction of heat flow in the halo and may be delayed as heat flows inwards, which is observed for halos m10b-s70, m10f-s70, and m10j-s70. The halos in the top row, which all collapse, exhibit outwards heat flow at late times.

constant cross section of 1 cm^2/g . This highlights the importance of accounting for the impacts of mergers when comparing the density profiles of halos in differing DM models.

The density evolution of an SIDM halo depends critically on the flow of heat through its innermost regions. This subsection explores the temperature gradients in the central regions of halos m10q, m10d, m10i, m10b, m10f, and m10j for the case of a 70 cm^2/g cross section, showing how they correlate with merger history and affect whether the system collapses. The average temperature, or specific kinetic energy, within some region of interest is given by

$$\overline{T} = \frac{E_{\rm kin}}{m_{\rm DM}} = \frac{1}{2}\sum_{i=1}^{N} v_i^2 \, , \tag{7.3}$$

where $E_{\rm kin}$ is the total kinetic energy, v_i is the velocity of the $i^{\rm th}$ particle, and N is the number of particles in the region. To study the heat flow in the central region of the halo, we compare the average temperature within 1 kpc, defined as $\overline{T}_{\rm inner}$, with that in the volume that extends from 1–5 kpc, defined as $\overline{T}_{\rm outer}$. For halos generated with $\sigma/m = 70~{\rm cm}^2/{\rm g}$, the core radius is generally $\lesssim 1$ kpc, as discussed in Appendix 7.1.1.[1] The maximum radius is set to 5 kpc because it encompasses the largest core radius encountered across the six halos studied at this cross section (for halo m10b-s70).

Figure 7.3 shows the fractional change in average temperature, $(\overline{T}_{\rm outer} - \overline{T}_{\rm inner})/\overline{T}_{\rm inner}$, as a function of time. A fractional change that is negative corresponds to heat flowing outward from the halo's core, as expected during gravothermal core collapse. In contrast, a positive temperature gradient corresponds to heat flowing towards the core, which can delay the collapse process. Recall that all three halos in the top row of Figure 7.3 core collapse. In each of these cases, the temperature gradient is negative after a period of some initial turbulence that is associated with the active and early formation of these systems. For example, the late-time evolution of halos m10q-s70 and m10d-s70 is fairly quiet and, in both cases, the mergers that occur after ~ 3 Gyr do not significantly impact the direction of heat flow. Halo m10i-s70, which has the fewest number of mergers in the set, has the most significant outward heat flow, which is correlated with how rapidly it core collapses. This is in agreement with the collapse times of these halos, which Figure 7.1 shows is ~ 6 Gyr for m10i-s70 and ~ 13 Gyr for m10q-s70 and m10d-s70.

The halos in the bottom row of Figure 7.3 do not core collapse, which should correlate

[1]The core radius is defined as the radius where the density falls to half the central density.

with more inwards heat flow. Halo m10b-s70 provides the most dramatic example, with the direction of heat flow changing several times during its evolution and a noticeable spike flowing into the core just after the major merger that occurs at an infall time of ~ 8 Gyr. Similarly, halo m10f-s70, which experiences a number of major mergers over its evolution, has considerable inward heat flow. Halo m10j-s70 experiences the largest spike in inwards heat flow across all halos, correlated with the significant radial merger around ~ 0.5 Gyr. Halos m10j-s70 and m10b-s70 have outwards heat flow at the latest snapshots, indicating that they may start collapsing if allowed to run further.

7.3 Low-Mass Host-Subhalo Dark Matter Scattering

Given the dramatic density change it undergoes during its last major merger, halo m10b provides a useful case study for understanding how variations to the DM scattering rate impact heat flow and core evolution. To this end, the left panel of Figure 7.4 compares the time evolution of ρ_c for halo m10b between three SIDM models: velocity-independent cross sections 30 cm^2/g (s30; dotted) and 70 cm^2/g (s70; solid), plus a velocity-dependent cross section with $\sigma_0/m = 147\ \mathrm{cm}^2/\mathrm{g}$ and $w = 24\ \mathrm{km/s}^2$ (vdSIDM; dash-dot-dotted). This particular velocity-dependent model gives scattering cross sections comparable to 70 (30) cm^2/g for particles with relative velocities $V_{\mathrm{rel}} \sim 25$ (35) km/s. Given that the host's velocity dispersion profile peaks at ~ 50 km/s and that the subhalos orbiting m10b have infall velocities in the $27-66$ km/s range,[3] this means that most halo-halo and halo-subhalo scattering events are suppressed relative to the constant cross section examples being compared to. However, this also decreases the cross section between host-host particles, impacting collapse time. The host halo has a velocity dispersion profile that reaches a maximum at 50 km/s, meaning host-host scattering also occurs with a suppressed cross section relative to the constant cross

[2]See Equation 5.4 for the full form of this cross section.

[3]The major merger that is of particular interest has an infall velocity of 50 km/s.

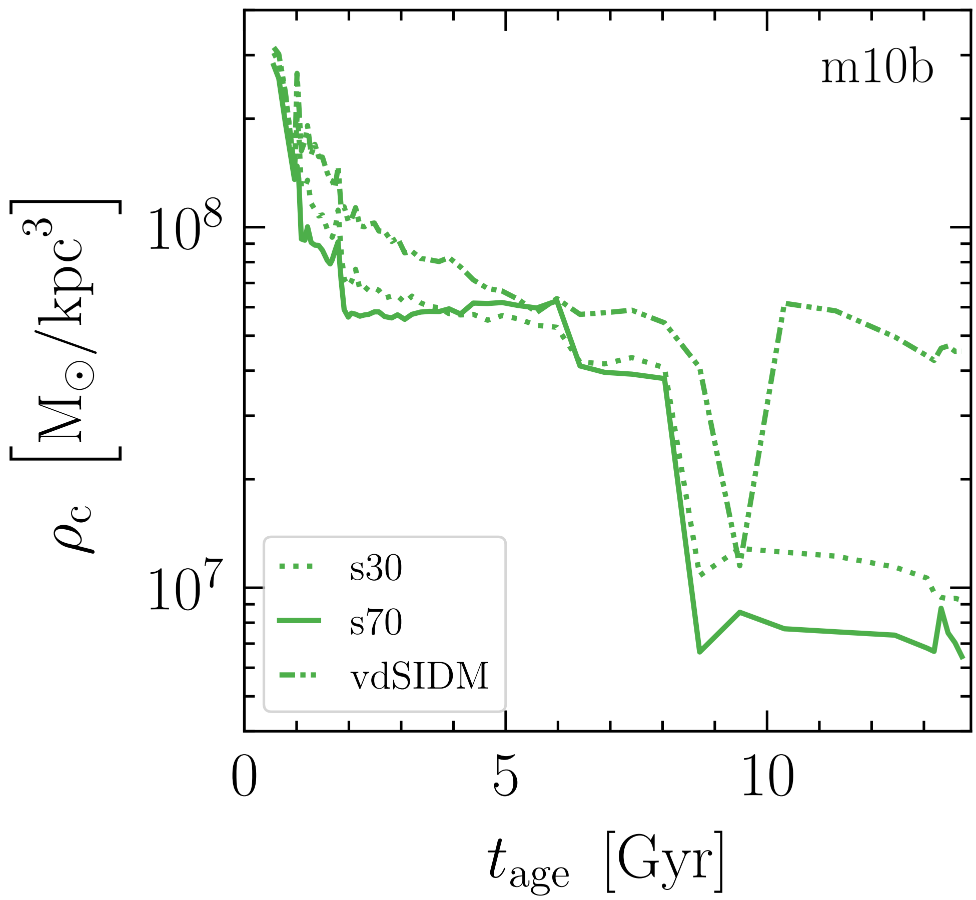

Figure 7.4: Core density evolution of halo m10b assuming three different models: SIDM with constant $\sigma/m = 30$ cm^2/g (dotted), SIDM with constant $\sigma/m = 70$ cm^2/g (solid), and SIDM with a velocity-dependent cross section with $\sigma_0 = 147$ cm^2/g and $w = 24$ km/s (dash-dot-dotted). Host halos in all three models experience a merger at ~ 6 Gyr and a major merger at ~ 8 Gyr. Halo m10b-s70 decreases in core density by an order of magnitude, with m10b-s30 decreasing slightly less. Halo m10b-vdSIDM has a temporary drop in density, but returns to it's core density before the major merger.

sections being compared to. Since subhalos orbit at similar velocity scales to the relative velocities of host particles, a velocity dependent cross section cannot impact subhalo-host interactions without also impacting host-host interactions.

In each model, the core density initially decreases, as expected in the core-expansion phase. The major merger at ~ 8 Gyr is concurrent with a decrease in ρ_c of 74% and 83% in the s30 and s70 halos, respectively, remaining essentially constant thereafter. The vdSIDM halo also experiences a decrease in core density of 72%, but this is followed by an increase in core density back to (approximately) its initial value.

To better understand how the SIDM model impacts the halo evolution, we must understand the relevant timescales. The dynamical timescale, the time it takes the halo to return to virial equilibrium, is given by

$$t_{\rm dyn} = (4\pi\ G\ \rho_{\rm c})^{-1/2}\,. \tag{7.4}$$

In all models, halo m10b has a dynamical timescale that is less than the time between simulation snapshots.

The timescale at which SIDM interactions impact halo evolution via halo-halo scattering is described as the thermal relaxation time (Yang & Yu, 2022; Outmezguine et al., 2023)

$$t_{\rm c} \sim (\rho_c\ v_c\ \langle\sigma/m\rangle)^{-1}\,. \tag{7.5}$$

This is a more general form of equation 6.1 where subscript c indicates that these are scale parameters taken at the core radius. The $\langle\cdot\rangle$ indicates a thermal average (Outmezguine et al., 2023; Gad-Nasr et al., 2023; Yang & Yu, 2022). In the core expansion phase, the thermal relaxation time dictates how quickly an SIDM halo develops an isothermal core with a flat temperature gradient. In the case of a merger, where the temperature gradient becomes

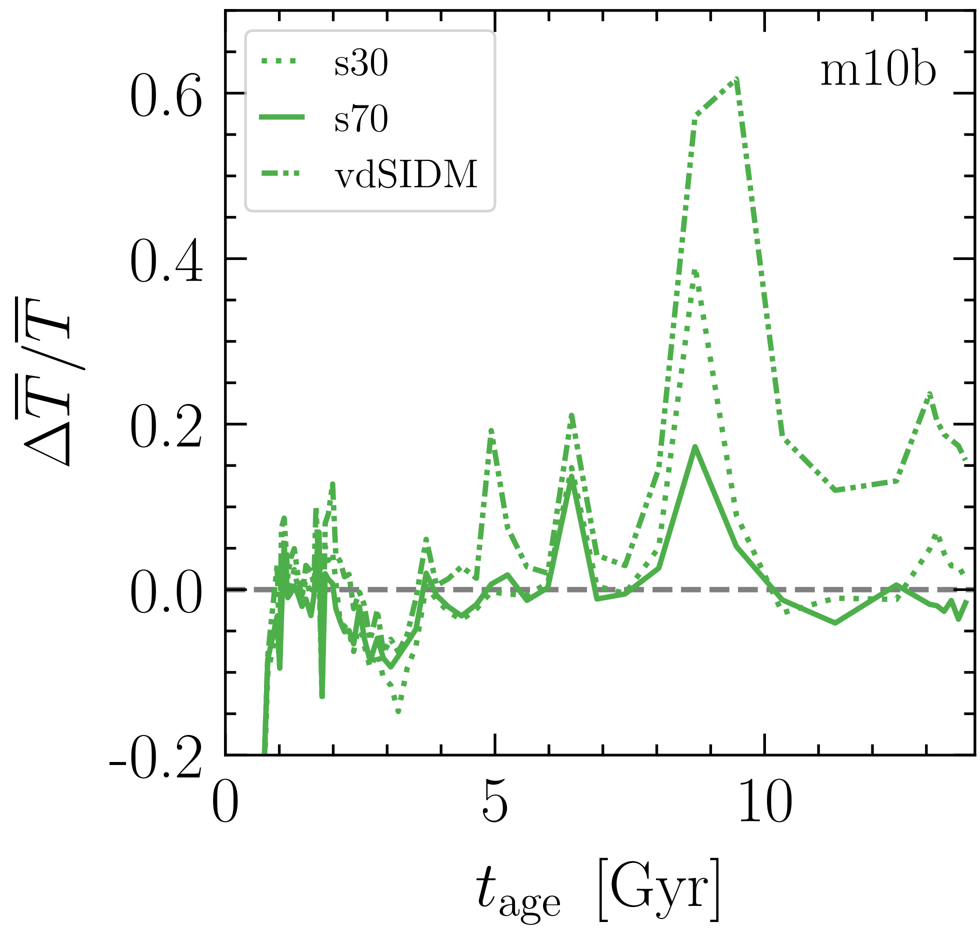

Figure 7.5: Difference in temperature between the core and the outer regions of halo m10b with three different DM models: SIDM with constant $\sigma/m = 30$ cm^2/g (dotted), SIDM with constant $\sigma/m = 70$ cm^2/g (solid), and SIDM with a velocity-dependent cross section with $\sigma_0 = 147$ cm^2/g and $w = 24$ km/s (dash-dot-dotted). Halos with larger thermally averaged cross sections maintain smaller temperature differences.

positive, the thermal relaxation time dictates how quickly the temperature gradient returns to zero.

Since the thermal relaxation time depends on cross section, halo m10b-s30, with $\langle\sigma/m\rangle = 30$ cm^2/g , will take about twice as long as m10b-s70, with $\langle\sigma/m\rangle = 70$ cm^2/g , to return to a state with an isothermal core after the merger. Halo m10b-vdSIDM, with $\langle\sigma/m\rangle = \mathcal{O}(1)$ cm^2/g , should take even longer than m10b-s30 to return to an isothermal core. In Section 7.3.1 we show the density and velocity dispersion profiles of halo m10b with these three models over time, confirming that m10b-s70 has the fastest thermal relaxation time and m10b-vdSIDM has the slowest.

To show how fast a halo returns to an isothermal core after a merger, we show the difference in temperature between the core and the outer regions of each m10b halo in Figure 7.5. Difference in temperature is calculated exactly as in Figure 7.3 as the difference in the specific kinetic energy within 1 kpc and the specific kinetic energy between $1-5$ kpc, normalized by the specific kinetic energy within 1 kpc. Figure 7.5 shows that the temperature difference increases with thermal relaxation time. Halo m10b-s30 reaches larger temperature differences and takes more time to return to an isothermal core than m10b-s70, and halo m10b-vdSIDM reaches larger temperature differences and takes more time to return to an isothermal core than both m10b-s30 and m10b-s70. After the major merger at ~ 8 Gyr, the m10b-vdSIDM halo does not return to an isothermal core within the age of the universe.

Halos with a short thermal relaxation will experience faster heating of the core due to mergers. Hotter cores produce lower core densities with larger core radii. Section 7.3.1 shows the halo velocity dispersion and density profiles across time to confirm this process.

7.3.1 Density and Velocity Dispersion Profiles Over Time

The difference in temperature in the core versus in regions outside the core is related to the core velocity dispersion. To show how the core velocity dispersion evolves with time, we show the density and velocity dispersion profiles at each snapshot. Figure 7.6 shows these profiles for halo m10b run with three DM models: SIDM with a constant cross section of $\sigma/m = 70$ cm^2/g (top), SIDM with a constant cross section of $\sigma/m = 30$ cm^2/g (middle), and SIDM with a velocity dependent cross section with $w = 24$ km/s and $\sigma_0 = 147$ cm^2/g (defined in Section 7.3; bottom).

The one-dimensional velocity dispersion is the magnitude of the three-dimensional variance of the velocity of each particle within 60 logarithmically spaced spherical shells.

All three halos experience a major merger at ~ 8 Gyr, which can be seen in Figure 7.6 as a peak in the velocity dispersion at ~ 20 kpc, which creates a positive slope in the velocity dispersion. In halo m10b-s70, the positive slope is quickly thermalized such that the halo has an isothermal core with a velocity dispersion of ~ 45 km/s. This leads to a large decrease in core density. In halo m10b-s30, the positive slope remains at later times, slowly becoming more isothermal. This leads to a small drop in core density. In halo m10b-vdSIDM, the positive slope remains almost unchanged until the end of the simulation, at 13.7 Gyr. This leads to an almost negligable drop in core density.

We conclude that the sustained decrease in core density concurrent with the infall of a disruptive merger is due to the merger imparting kinetic energy around the core and efficiently heating the core via SIDM scattering.

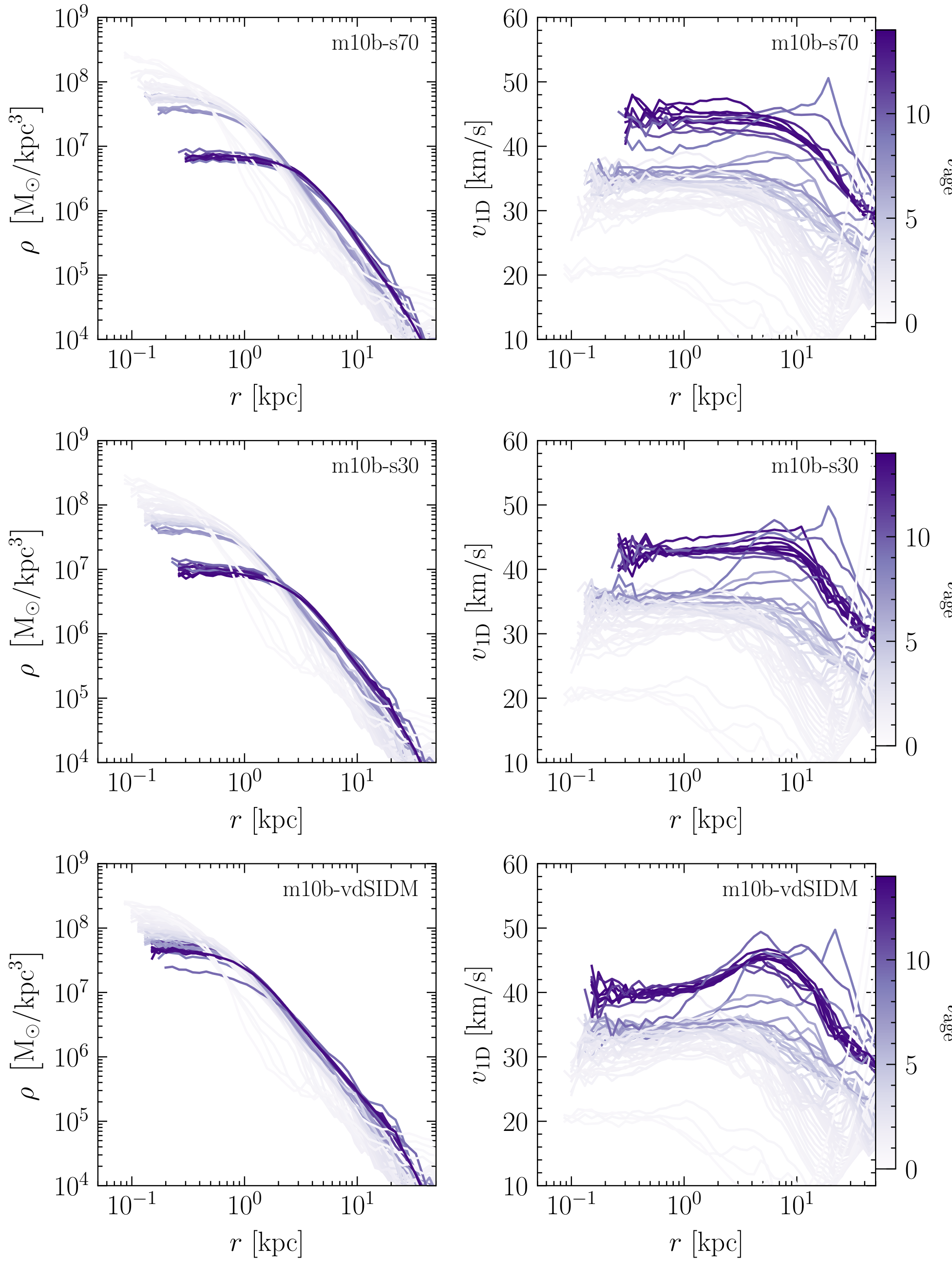

Figure 7.6: Density (left) and one-dimensional velocity dispersion (right) profiles at all snapshots for the m10b halo with three DM models: SIDM with a constant cross section of $\sigma/m = 70$ cm^2/g (top), SIDM with a constant cross section of $\sigma/m = 30$ cm^2/g (middle), and SIDM with a velocity dependent cross section with $w = 24$ km/s and $\sigma_0 = 147$ cm^2/g (defined in Section 7.3; bottom). Halos in all three models experience a major merger at ~ 3 Gyr. At this time, the velocity dispersion develops a positive gradient between $1 - 10$ kpc. Halo m10b-s70 returns to an isothermal core profile within a few snapshots and halo m10b-s30 returns to an isothermal core profile by the end of the simulation. However, halo m10b-vdSIDM continues to have a positive dispersion gadient until the end of the simulation.

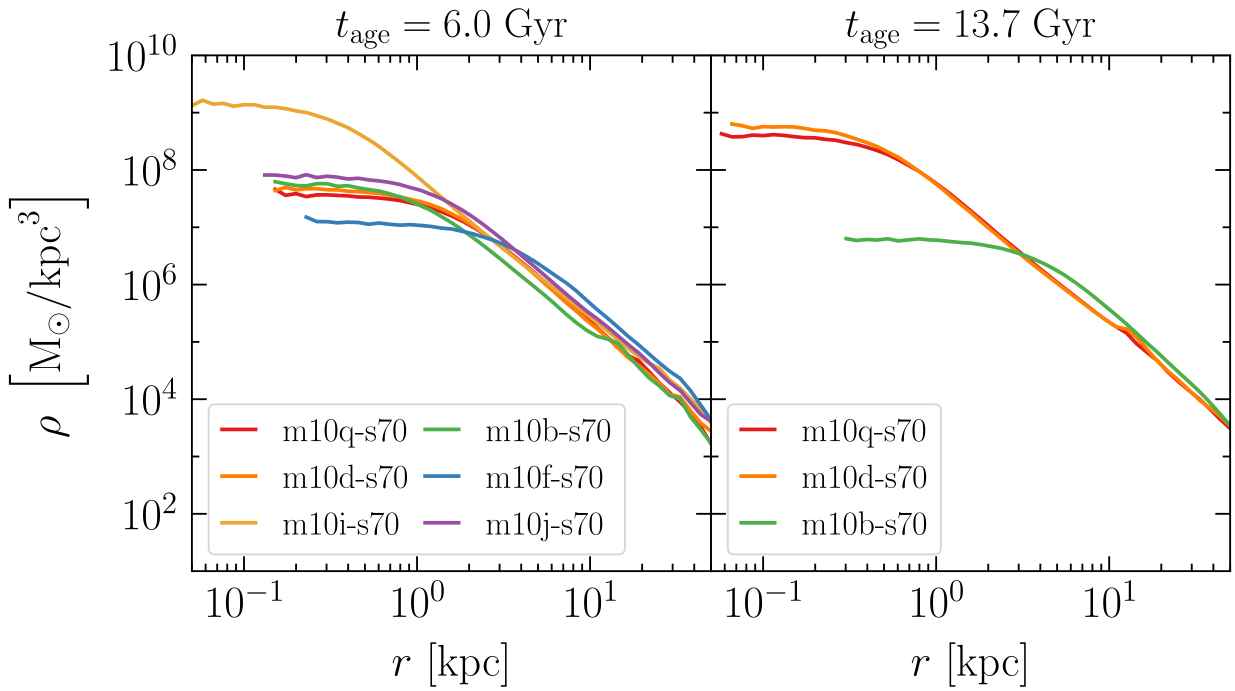

Figure 7.7: Density profiles of six host halos (m10q, m10d, m10i, m10b, m10f, and m10j) with a cross section of $\sigma/m = 70$ cm^2/g . The left panel shows the halos at $t_{\rm age} = 6$ Gyr ($z = 1$) and the right panel shows the halos at $t_{\rm age} = 13.7$ Gyr ($z = 0$). Some halos stall before reaching 13.7 Gyr and, thus, are not shown in the right panel. Halo m10i-s70 at $t_{\rm age} = 6$ Gyr and halos m10q-s70 and m10d-s70 at $t_{\rm age} = 13.7$ Gyr depict gravothermally collapsed halos. Halos m10q-s70, m10d-s70, m10b-s70, and m10j-s70 at $t_{\rm age} = 6$ Gyr depict cored halos. Halo m10f-s70 at $t_{\rm age} = 6$ Gyr and halo m10b-s70 at $t_{\rm age} = 13.7$ Gyr depict ultra-cored halos with core densities almost an order of magnitude lower than the densities predicted by the fluid model.

7.4 Diversity of Density Profiles in Low-Mass Halos with large Cross Sections

In this Section we discuss the diversity of density profiles produced by SIDM DMO simulations of low-mass halos and how this relates to the Core-Cusp problem. In particular, Kong et al. (2022) point out that IllustrisTNG (Nelson et al., 2019) halos with masses $\sim 10^{10}\mathrm{M}_\odot$ do not reproduce the large $R_{\rm max}$ and slow rising inner circular velocity profiles of seven gas-rich isolated ultradiffuse galaxies (UDGs). They find that these UDGs are consistent with DM density profiles that have low-density, extended cores (Kong et al., 2022).

Observations of isolated field galaxies infer that halos have both cored and cuspy central density profiles (Flores & Primack, 1994; Moore et al., 1999; Dubinski & Carlberg, 1991), while CDM DMO simulations produce cored central density profiles (Navarro et al., 1997). This motivates

Figure 7.7 shows the density profiles of all halos with $\sigma/m = 70$ cm^2/g at $t = 6$ Gyr ($z = 1$; left) and $t = 13.7$ Gyr ($z = 0$; right). Profiles are only shown for radii that enclose at least 200 particles. Although these halos are all run with the same cross section and are shown at the same times, their density profiles within 1 kpc span two orders of magnitude—ranging from cored to cuspy.

The left column of Figure 7.7 shows that at $t = 6$ Gyr, m10i-s70 has a high-density core of about 10^9 M$_\odot$/kpc^3 that extends to about 0.3 kpc corresponding to a steeply increasing inner circular velocity profile. This is indicative of a halo undergoing gravothermal core collapse. Halo m10i-s70 is not run past $t = 6$ Gyr due to stalling from its high density core. Conversely, at $t = 6$ Gyr, m10f-s70 has a low-density core of about 10^7 M$_\odot$/kpc^3 that extends to about 3 kpc corresponding to a gradually increasing inner circular velocity profile. These two halos emphasize that SIDM can produce both concentrated halos via gravothermal collapse, and cored halos.

At $t = 6$ Gyr, halos m10j-s70, m10b-s70, m10d-s70, and m10q-s70 all have cores of about 10^8 M$_\odot$/kpc^3 that extend to about 1 kpc corresponding to moderately increasing inner circular velocity profiles. Halos m10f-s70 and m10j-s70 are not run past $t = 6$ Gyr due to stalling from other halos in the cosmological box that develop high density cores.

Halos m10b-s70, m10d-s70, and m10q-s70 are run to $t = 13.7$ Gyr and their profiles are shown in the right panel of Figure 7.7. Although these halos all had similar central densities at $t = 6$ Gyr, their central densities span two orders of magnitude by $t = 13.7$ Gyr—again ranging from cored to cuspy. Halos m10q-s70 and m10d-s70 both have high-density cores with densities $\gtrsim 5 \times 10^8$ $M_\odot/\mathrm{kpc}^3$ within 0.4 kpc. Halo m10b-s70 has an extremely low-density core of less than 10^7 $M_\odot/\mathrm{kpc}^3$ that extends to about 5 kpc corresponding to a gradually increasing inner circular velocity profile.

At their latest snapshots, halos m10f-s70 and m10b-s70 both have core density profiles about 0.7 and 0.9 dex lower than the analytic model from an NFW profile predicts (see Figure 8.1). Since such low densities are not predicted by the fluid model, we postulate that these ultra-cored profiles form due to mergers. Such ultra-cored halos are similar to the density profiles required to explain the observed gas-rich isolated UDGs noted by Kong et al. (2022) to be in tension with simulated field galaxies in IllustrisTNG. In conclusion, large SIDM cross sections in conjunction with major or frequent mergers is a novel method of creating extremely low-density cores.

Although we form core densities that span 2 orders of magnitude in DMO simulations, it is important to note that these conclusions may be impacted by baryonic physics. The sample of CDM halos studied in this work span the spread in the stellar mass-halo mass relation, ranging from $M_\star = 5 \times 10^5 - 1 \times 10^7 M_\odot$ (Fitts et al., 2017). Using CDM, hydrodynamical simulations form low-density cores compared to DMO simulations, with the difference in core density increasing with stellar mass (Fitts et al., 2017). Robles et al. (2017) find similar conclusions using SIDM with $\sigma/m = 1$ cm^2/g . We explore the impacts of baryonic physics in these simulations with large SIDM cross sections in an upcoming work (Hussein et al., in prep).

Thus, Figure 7.7 shows the diversity in density profiles in DMO simulations that arise from variations in initial conditions. This diversity may alleviate the Core-Cusp problem and may provide an explanation for the extended DM cores in UDGs.

Chapter 8

Simulations versus the Fluid Model of Low-Mass Halos

The simulation suite generated in this work provides a unique opportunity to test, for the first time, whether cosmological N-body simulations of gravothermal collapse reproduce analytic predictions. These models evolve a spherically symmetric, isolated, and virialized halo through time by solving the gravothermal equations that relate halo density, mass, luminosity, and velocity dispersion. I use the `GravothermalSIDM`[1] code (Outmezguine et al., 2023; Gad-Nasr et al., 2023) to analytically evolve an SIDM halo from an initial NFW profile (Navarro et al., 1997) with scale density ρ_s and radius r_s. I show that the halos analyzed in this section are not well modeled by the gravothermal fluid model; halos reach lower core densities and collapse slower than predicted by the model.

This chapter is based on research in preparation for submission to the Astrophysical Journal. I use "we" throughout to acknowledge the joint contributions of myself (first author) and my co-authors.

[1] `https://github.com/kboddy/GravothermalSIDM`

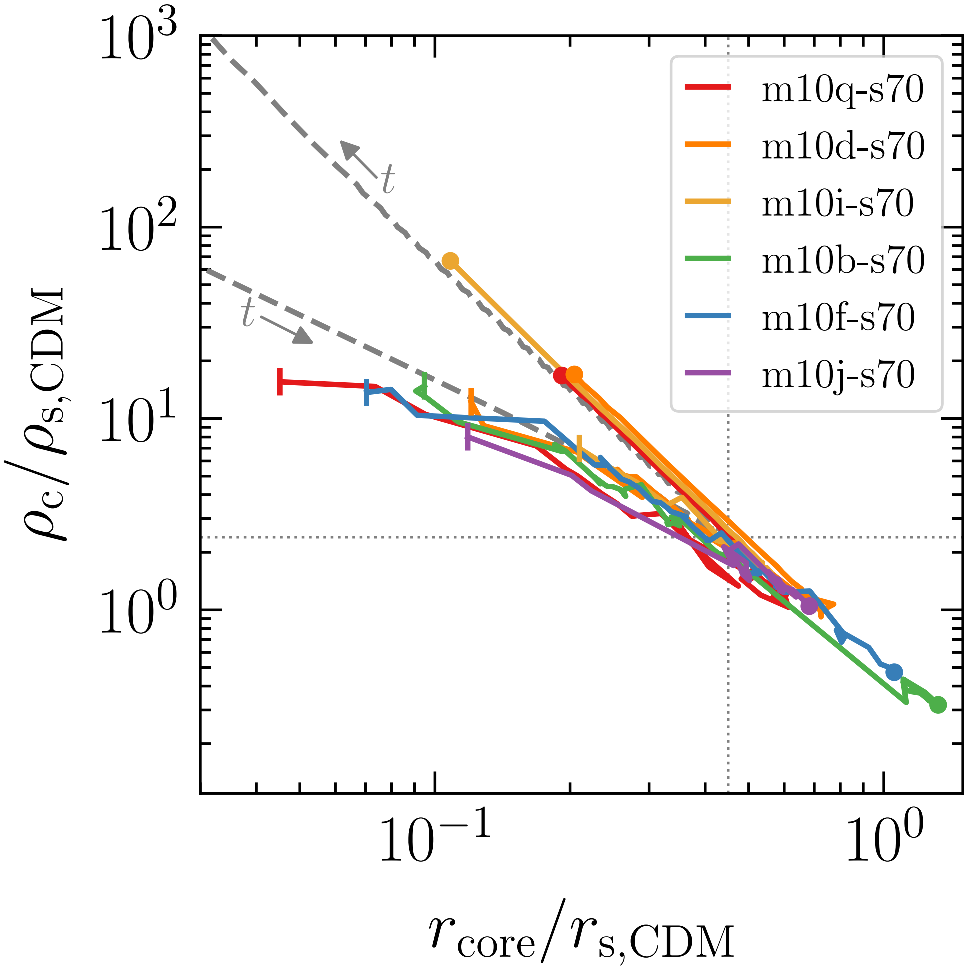

Figure 8.1: Core density and radius evolution for all halos (m10q, m10d, m10i, m10b, m10f, and m10j) with $\sigma/m = 70\ \mathrm{cm^2/g}$ compared to the fluid model (dashed gray; Outmezguine et al. 2023). The core density is normalized by the scale density of the CDM counterpart of each halo at $z = 0$, $\rho_{\mathrm{s,CDM}}$. Similarly, the core radius is normalized by the CDM scale radius, $r_{\mathrm{s,CDM}}$. The earliest timestep of each simulated halo is indicated by a vertical line and the latest timestep is indicated by a dot. The flow of time is indicated by gray arrows along the model. The dotted gray lines highlight the predicted turnaround point at $\rho_{\mathrm{c},0}$ and $r_{\mathrm{core},0}$, predicted by Outmezguine et al. (2023) to be universal at $\rho_{\mathrm{c},0} \simeq 2.4\rho_{\mathrm{s}}$ and $r_{\mathrm{core},0} \simeq 0.45 r_{\mathrm{s}}$. Halos m10q-s70, m10d-s70, and m10i-s70 follow the fluid model, particularly in the collapse regime. However, all halos reach lower minimum core densities and larger core radii than predicted by the fluid model. Halos m10b-s70 and m0f-s70 reach core densities an order of magnitude lower than those predicted by the fluid model.

8.1 Minimum Core Density-Maximum Core Radius

In idealized simulations, Outmezguine et al. (2023) find that the gravothermal evolution of halos is universal with minimum core density $\rho_{\mathrm{c},0}/\rho_{\mathrm{s}} = 2.4$, maximal core radius $r_{\mathrm{core},0}/r_{\mathrm{s}} = 0.45$, and core velocity dispersion at minimum density $v_{\mathrm{c},0} = 0.64 V_{\mathrm{max}}$ where ρ_{s} and r_{s} are the scale density and radius of the initial NFW profile and V_{max} is the maximum circular velocity of the initial NFW profile.

Figure 8.1 shows the core density and radius evolution from the fluid model (dashed gray) with the time evolution indicated by arrows along the model. Figure 8.1 also shows the normalized $\rho_{\mathrm{c}} - r_{\mathrm{core}}$ evolution of simulated halos. Since the model expects an NFW profile to normalize, we use the $z = 0$ density profile from CDM counterpart of each SIDM halo. ρ_{s} and r_{s} are determined by fitting an NFW to the density profiles of each halo between $r = 0.5 - 30$ kpc using `COLOSSUS` (Diemer, 2018).

Figure 8.1 indicates that the simulations do not follow the fluid model prediction. Halos m10i-s70, m10d-s70, and m10q-s70 follow the model after collapse, but all reach maximum cores with larger radii and lower densities than predicted. The trajectories for the three halos that do not collapse (m10j-s70, m10b-s70, and m10f-s70) are noteworthy as they never turn around and end up with larger radii and lower densities than predicted (final snapshots are indicated by a dot).

8.2 Collapse Time

Next, we explore how the analytical predictions for the time of gravothermal collapse compare with the simulation results. The collapse time of an SIDM halo is estimated using equations 6.1 and 6.2. C is an order unity constant that calibrates the fluid model to N-body simulations. Values ranging from $C = 0.6 - 0.84$ have been found to agree with other simulations (Essig et al., 2019; Nishikawa et al., 2020; Palubski et al., 2024; Yang et al., 2024). We use the geometric mean of this range, $C = 0.71$[2]. Using $C = 0.6$ or 0.84 increases or decreases $t_{\rm collapse}$ by 0.073 dex.

We calculate $t_{\rm coll,model}$ using two methods. First, we use $\rho_{\rm s}$ and $V_{\rm max}$ from the CDM $z = 0$ halos. $\rho_{\rm s}$ and $V_{\rm max}$ are determined by fitting an NFW profile to the density profile between $r = 0.5 - 30$ kpc using `COLOSSUS` (Diemer, 2018). The predicted correlations are then used to calculate $\rho_{\rm c,0} = 2.4\rho_{\rm s}$ and $v_{\rm c,0} = 0.64V_{\rm max}$ (Outmezguine et al., 2023). These values are input into equations 6.1 and 6.2, and the resulting $t_{\rm collapse}$ is shown by unfilled bars in Figure 8.2. However, since Figure 8.1 shows that the simulations do not follow the predicted correlation, we also use $\rho_{\rm c,0}$ and $v_{\rm c,0}$ directly from the simulation, shown in hashed bars. $\rho_{\rm c,0}$ and $v_{\rm c,0}$ are calculated as the density and 1D velocity dispersion within $r_{\rm core}$ at $t_{\rm core}$. The second method is more dependent on the simulation and therefore has less predictive power. $t_{\rm coll,sim}$, shown in filled bars, is calculated as the time when the core density reaches $\sim 10\rho_{\rm c,0}$. If a halo does not reach that point, the smulated collapse time is not shown.

Figure 8.2 indicates that all halos are predicted to collapse within 13.8 Gyr when using the CDM $\rho_{\rm s}$ and $r_{\rm s}$ values. When instead using $\rho_{\rm c,0}$ and $v_{\rm c,0}$ from the simulation, the predicted collapse time increases for all halos, delaying the predicted collapse time past 13.8 Gyr for m10b-s70 and m10f-s70. The delay in collapse time is due to $\rho_{\rm c,0}$ being $< 2.4\rho_{\rm s}$, likely due to mergers. The simulated halos m10q-s70, m10d-s70, and m10i-s70 collapse within 3 Gyr of predicted $t_{\rm collapse}$ when using $\rho_{\rm c,0}$ and $v_{\rm c,0}$ from the simulation. These halos experience few mergers at late times. We can't compare $t_{\rm coll,sim}$ to $t_{\rm coll,model}$ for halos that have not entered the core collapse regime since $\rho_{\rm c,0}$ and $v_{\rm c,0}$ are at the final timestep of the simulation. However, it is clear that m10j-s70 is deviating from the model since both of its predicted collapse times are before the final timestep of the simulation, yet the simulated halo has

[2] We do not fit for C because these halos do not follow the analytic model well enough to allow for an accurate fit, as shown in Figure 8.1

not collapsed. Halos m10b-s70 and m10f-s70 would need to be run longer to compare the simulation to the model accurately.

In conclusion, the expected universality of the fluid model breaks down for all six isolated cosmological simulations. Consequently, the model is not able to consistently predict the collapse time of halos when using initial NFW $\rho_{\rm s}$ *and* $r_{\rm s}$*. The model, tuned to* $\rho_{\rm c,0}$ *and* $\upsilon_{\rm c,0}$*, is able to predict the simulated collapse time for three of six halos. These three halos have quiet merger histories with no major mergers on radial orbits at late times. This suggests that the fluid model loses its predictive power in cosmological settings where halo merger history,* $\rho_{\rm c,0}$*, and* $\upsilon_{\rm c,0}$ *are not known.*

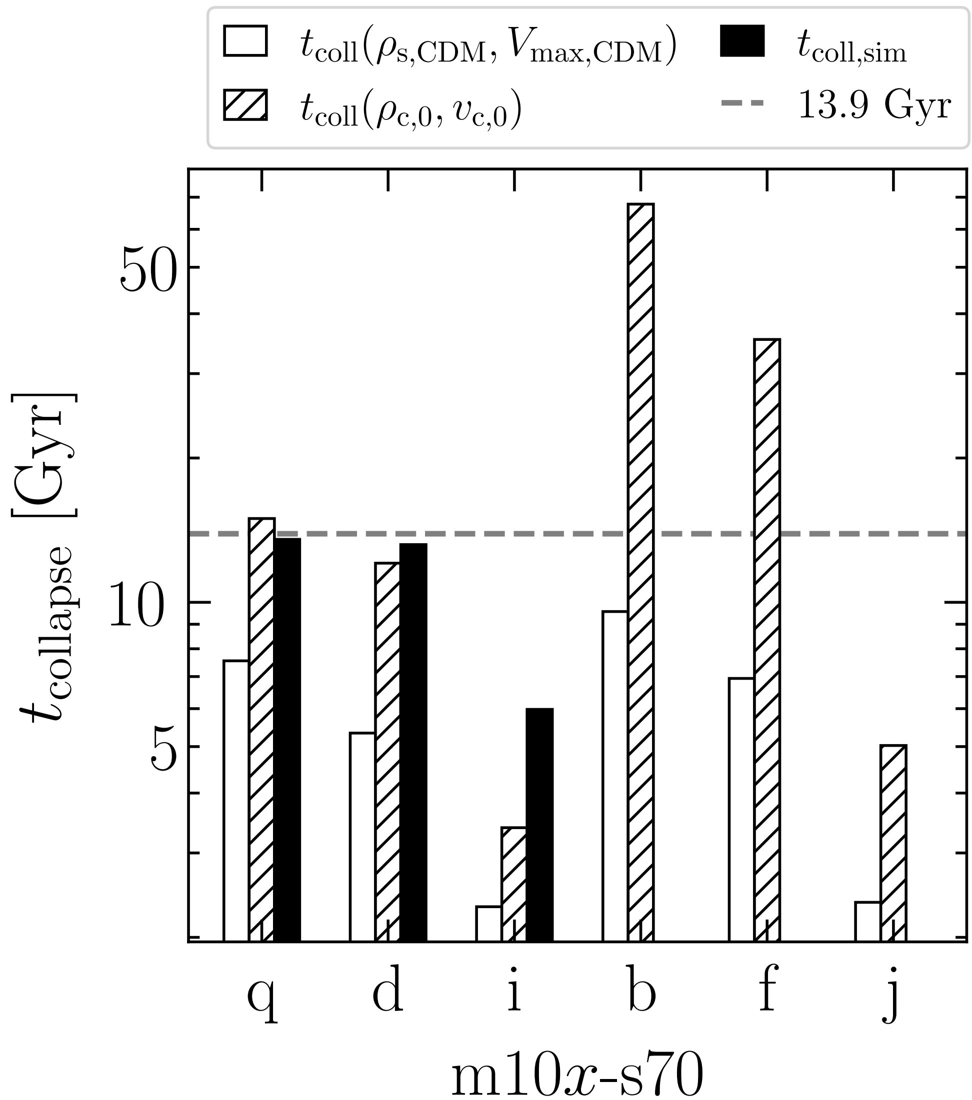

Figure 8.2: Collapse time predicted by the fluid model compared to collapse time of the simulation. Predicted collapse time is calculated using equation 6.2 with two sets of inputs. The unfilled bars show $t_{\rm collapse}$ calculated from $\rho_{\rm s,CDM}$ and $r_{\rm s,CDM}$ fit to the CDM $z = 0$ simulation. This estimates the collapse time fully via the analytic model. The hashed bars show $t_{\rm collapse}$ calculated from $\rho_{\rm c,0}$ and $v_{\rm c,0}$ from the s70 simulations. This estimates the collapse time from the minimum density of the SIDM simulation. Collapse time from the simulation is calculated as the time when the core density reaches $\sim 10\ \rho_{\rm c,0}$. The simulation collapse time is not shown in cases where the halo doesn't reach collapse. The dashed gray line shows $t_{\rm collapse} = 13.9$ Gyr. All halos collapse later than predicted using a CDM halo as initial conditions. In three of the six cases (m10b-s70, m10f-s70, and m10j-s70), the collapse time is delayed past the end of the simulation.

Chapter 9

Rising Stargirls: Benefits of a Creative Arts-Based Approach to Astronomy Education for Middle-School Girls from Underrepresented Groups

Women from historically marginalized groups in the sciences continue to be severely underrepresented in the fields of physics and astronomy. Young girls identifying with these groups often lose interest in science, technology, engineering, and math (STEM) fields well before college. Middle school (grades 6-8) emerges as a pivotal phase for nurturing science identities among girls. The educational program Rising Stargirls offers creative arts-based astronomy workshops for middle-school girls, with the aim of cultivating their science identities. We retrospectively analyze participants' responses to four key assessment items through which their engagement in science and their science identities before and after the workshops are assessed. Our findings overwhelmingly indicate that girls exhibit heightened engagement in science and enhanced science identities after engaging in the Rising Stargirls program. These outcomes underscore the merits of fostering creativity and integrating the arts into science education.

9.1 Introduction

Women from historically marginalized groups in the sciences (American Indian or Alaska Native, Black or African-American, Hispanic or Latinx, Native Hawaiian or other Pacific Islander, hereafter "URM") continue to be severely underrepresented in the fields of physics and astronomy. This remains true across all levels of the academic hierarchy in physics and astronomy, and disparities persist in advances across URM groups. The number of Latinx women earning bachelor's degrees in astronomy has doubled to 16% since 2002, and though still under the Hispanic/Latinx population of 19.1% in the United States, progress has been made over the past 20 years (Porter & Ivie, 2019). In contrast, the number of African American women earning bachelor's degrees in astronomy has remained relatively static over the same time period, at 3%, despite African Americans comprising 13.6% of the United States population (Mulvey & Nicholson, 2020). At the PhD level, during the 2018-19 academic year, of the 1,875 total doctorates earned in physics, ten were awarded to Latinx women, and one was awarded to an African American woman (The American Institute of Physics, 2022).

Girls from URM groups often stop pursuing their interest in science, technology, engineering, and math (STEM) fields long before they enter college due to a lack of self-confidence and few role models who look like them (Weir, 2007). The combined impact of internal and external forces on the educational trajectories of women of color underscores that there is a small window of opportunity available to cultivate interest and nurture the involvement of young URM girls in astronomy and physics. The *Planetary Science and Astrobiology Decadal Survey 2023-2032* has identified that "increasing diversity and representation in NASA Planetary Science Division missions requires a concerted effort to engage members of underrepresented communities at early stages of career/education" (National Academies of Sciences, Engineering, and Medicine, 2022).

Middle school is often the time where girls (aged 10-14) start to place a significant amount of focus on their physical appearance, and shift the focus away from their mental aptitude and accomplishments (Gurian, 2012). As a result, feelings of low self-esteem and a lack of self-confidence begin to take root (Rakow, 2009; Gurian, 2012). This age range is both a challenging time for young girls, and an ideal time to develop and nurture their science identities, which is deemed critical for the retention of African American students pursuing an undergraduate degree in Physics and Astronomy (The AIP National Task Force to Elevate the Representation of African Americans in Undergraduate Physics and Astronomy (TEAM-UP), 2020).

Studies on teaching methods and assessment strategies suggest that students' conceptual understanding of astronomy improves as a result of the implementation of learner-centered, interactive exercises in class (Alexander, 2005; Rudolph et al., 2010). Additionally, the incorporation of literary exercises and role-playing exercises has been shown to improve students' engagement and excitement in astronomy and astrobiology, as well as their confidence in answering questions (Garland & Ratay, 2007; Crider & Weston, 2012). Wulf et al. (2013) show that shifting their curriculum such that students take on an active role in their learning promotes development of student agency and communication. And according to the National Research Council National Research Council (2009), informal settings provide an increased motivation to learn about the natural world, and to develop and nurture an identity that includes practicing and even contributing to science. In summary, learner-centered, interactive, literary, and role-playing exercises and giving students an active role in their learning have been shown to improve students' engagement with science and science identity—their perception of themselves as a "science person".

To add to these results, we study the effects of creative arts-based astronomy curricula on the broader science engagement and science identity of middle-school girls. To not only involve but enthrall girls in the possibility of identifying with and potentially becoming astronomy and planetary science researchers means engaging girls in the discovery and exploration of astronomical phenomena and questions, using who they are and what they think and feel about the universe as the lens through which this information is processed.

To study the impact of creative arts-based education, we analyze data from anonymous program-improvement surveys conducted by Rising Stargirls between 2015 and 2023. Rising Stargirls[1], a program founded by Professor Aomawa Shields and facilitated by the authors, offers creative arts-based astronomy workshops for middle-school girls with the mission to build personal connections between the girls and the universe, of which they are an integral part. By integrating creative arts-based strategies such as free writing, visual art, and theater exercises, Rising Stargirls has developed a curriculum that "addresses each girl as a whole by providing an avenue for individual self-expression and personal exploration that is interwoven with scientific engagement and discovery."[2] Using this approach, we highlight how incorporating creative arts at the core of astronomy education can enhance participants' engagement with science and strengthen their science identity.

Data analyzed in this study are in response to four survey items. Science identity is probed by analyzing participant responses to questions asking whether they believe they can do well in science and if they see themselves as scientists. Engagement in science is probed by analyzing participant responses to questions asking if they talk to their families and friends about science and if they enjoy their science classes.

[1] http://www.risingstargirls.org/
[2] http://www.risingstargirls.org/

This study explores the impact of creative arts-based astronomy activities on middle-school girls of all colors and backgrounds. However, given that a majority of participants identify with at least one URM group (see Table 9.1), these results also highlight the benefits of creative arts-based astronomy activities on girls from URM groups.

Although Rising Stargirls is an astronomy-focused education program, we offer two key reasons for its use in studying girls' engagement and identity in science more broadly. First, middle-school girls often lack access to formal astronomy classes in school, so gauging changes in their engagement and identity with science is more meaningful at this stage of their education. Second, our hypothesis is not confined to astronomy; it applies across the sciences. Therefore, the assessment questions evaluate participants' engagement with science and their science identity. This approach allows us to explore the benefits of creative arts-based curricula in science education, with astronomy workshops serving as our model.

In short, this work addresses the broader question: How does incorporating creative arts into science education increase engagement with science and shape science identity among middle-school girls? Using data collected by an educational outreach program that engages middle-school girls in creative arts-based astronomy workshops, we analyze responses to four survey items: two designed to assess participants' engagement in science, and two aimed at evaluating their science identity. Our results demonstrate that encouraging middle-school girls to bring their creativity to science promotes their engagement with science and nurtures their science identity.

This paper is organized as follows: Section 9.2 describes the Rising Stargirls program, including the resources that the program has made publicly available. Section 9.3 details the data collection and analysis methodology. Section 9.4 describes the results of our analysis, separated by Rising Stargirls' in-person and virtual workshops. Finally, Section 9.5 discusses the impacts, limitations, and conclusions of our results.

9.2 Program Description

Rising Stargirls was founded in 2014 with the mission to build personal connections between middle-school URM girls and the universe with the aim of encouraging increased participation in astronomy and astrobiology from groups traditionally underrepresented in the sciences. It integrates scientific discovery with arts-based activities to invite girls to bring their whole selves to the science learning process.

The curriculum is implemented in after-school or summer camp workshops for middle-school students. Rising Stargirls' workshops have been conducted in-person on the East and West Coasts of the United States, and virtually on Zoom for students across the world. In the six workshops analyzed in this study, Rising Stargirls reached 126 students across the world! The format for the workshops is flexible but the curriculum remains largely consistent. The curriculum is a collection of arts-based astronomy activities that are selected and curated from free, publicly-available Rising Stargirls educational materials (see Section 9.2.2).

An example arts-based astronomy activity that participants in Rising Stargirls' workshops experienced focuses on teaching girls about extrasolar planets (or "exoplanets") – planets that orbit stars other than our Sun. The activity begins with a lecture that includes images and videos of exoplanets to give them a visual representation. During the lecture, participants have the opportunity to share what they know with facilitators and peers and ask questions. They learn the definition of a planet, and the difference between planets within our solar system and exoplanets. After being introduced to basic concepts, they apply their knowledge through a hands-on activity called, "Build Your Own Exoplanet."

The goal of this activity is to give participants an opportunity to think critically and creatively about the types of exoplanets that may exist. They are encouraged to consider what they might look like and what elements of a planet might be conducive or detrimental to life. Each participant receives a large sheet of construction paper, a pencil, a pen, crayons,

	Race or Ethnicity	Number	
URM	Black or African American	16	48
	Hispanic, Latinx or Spanish Origin	18	
	American Indian or Alaska Native	2	
	Mixed race URM	12	
Non-URM	Asian	14	25
	Middle Eastern or North African	2	
	White	9	
Unspecified	Unspecified	7	7
	Total participants	80	

Table 9.1: Demographics of virtual workshop participants from Summer 2021, 2022, and 2023. Of the total, 48 identified as URM, 25 non-URM, and 7 preferred not to specify. The categories shown are based on the National Science Foundation categorizations (National Center for Science and Engineering Statistics (NCSES), 2023).

and markers to design their own exoplanet. They get to decide whether their planet is rocky like Earth or giant like Jupiter; whether it is cold or hot. They are also asked to think about whether their planet contains land or ocean; if it's an aquaplanet, or a land planet. Additionally, they are asked to reflect on what life might look like on that planet. This activity is intended to encourage curiosity, creativity, and imagination, and help girls develop their scientific thinking.

This example activity is supported by multiple other activities that participants do earlier in the workshop. For example, an activity that precedes this one is called "Art and the Cosmic Connection," adapted with permission from *NASA's Discovery & New Frontiers Programs*[3]. In this activity, girls create their own artist depictions of NASA images. These images show planets and moons that are similar to potential exoplanet environments, fueling their creativity for what their own exoplanet might look like.

[3]https://eurekus.org/nasa-art-cosmic-connection

9.2.1 Participant Demographics

The primary demographic of Rising Stargirls workshops are middle-school aged (11-14 years old). However, in order to welcome broad interest, occasional exceptions were made to accommodate participants who were younger or older than this range. Therefore, it is noted that some survey responses may correspond to students outside of the middle-school age range.

From 2015 to 2016, three in-person Rising Starigirls workshops were conducted by Professor Aomawa Shields with support from her NSF Astronomy and Astrophysics Postdoctoral Fellowship.

In Winter 2015, Rising Stargirls collaborated with Irving STEAM Magnet Middle School in Eagle Rock, California to offer their students after-school programming. Irving STEAM aims to develop critical thinking by project-based learning that incorporates both the arts and sciences. In 2019, Irving STEAM's student population was 82% Hispanic[4], and 100% of students who participated in the Rising Stargirls after-school programming in 2015 self identified as Hispanic. This after-school programming took place for two hours twice a week for three weeks, for a total of 12 hours.

In Summer 2015, Rising Stargirls collaborated with the Science Club for Girls in Cambridge, Massachusetts for their intensive skill-development and career exploration program called "Young Leaders in STEM." Science Club for Girls offers experiential learning for girls and gender-expansive youth from underrepresented communities[5]. Students who participated in the Rising Stargirls summer programming came from low-income backgrounds. This summer camp programming took place over four days within a week for four hours each day, for a total of 16 hours.

[4]https://www.greatschools.org/california/los-angeles/2162-Irving-STEAM-Magnet/#Students
[5]https://www.scienceclubforgirls.org/

In Fall 2016, Rising Stargirls collaborated with the Young Women's Christian Association (YWCA) in Pasadena-Foothill Valley. The YWCA's mission of "eliminating racism, empowering women, and promoting peace, justice, freedom and dignity for all," [6] aligns with Rising Stargirls' mission of "encouraging girls of all colors and backgrounds to learn, explore, and discover the universe."[7] In 2010, 34% of Pasadena's population identified as Hispanic or Latino, and 10% identified as Black. This after-school programming took place for two hours twice a week for three weeks, for a total of 12 hours.

With the onset of the COVID-19 pandemic in 2020, Rising Stargirls adapted its programming to a virtual format to continue reaching students during the isolation restraints. In Summer 2021, Rising Stargirls hosted its first virtual workshop. It reached 40 participants living in nine states across the United States. Of its participants, 57% self identified with URM groups. This summer workshop ran for two hours a day, Monday through Friday for two weeks, for a total of 20 hours.

In Summer 2022, Rising Stargirls hosted its second virtual workshop. It reached 28 participants, including four returning participants, from nine states across the United States. Of its participants, 69% self identified with URM groups. This summer workshop ran for two hours a day, Monday through Friday for two weeks, for a total of 20 hours.

In Summer 2023, Rising Stargirls hosted its third virtual workshop. It reached 33 participants, including three returning participants, from 11 states across the United States and five countries outside of the United States. Of its participants, 48% self identified with URM groups. This summer workshop ran for two hours a day, Monday through Friday for two weeks, for a total of 20 hours.

The demographics of the participants in the three virtual workshops are presented in Table 9.1. Demographics of participants in the in-person workshops were not available, so they

[6] https://www.ywca.org/what-we-do/our-mission-in-action/
[7] http://www.risingstargirls.org/

are not included in Table 9.1. Of the 66 participants who filled out a demographic survey, 60% identified with URM groups, with 20% being Black or African American, 23% Hispanic, Latinx, or Spanish origin, 3% American Indian or Alaska Native, and 15% having multiple identities, including at least one URM. The remaining 31% of the participants identified with non-URM groups, with 18% being Asian, 3% Middle Eastern or North African, and 11% White. The remaining 9% preferred not to specify. These categories for participant race and ethnicity are based on the categories for URM by the National Center for Science and Engineering Statistics National Center for Science and Engineering Statistics (NCSES) (2023). This demonstrates that the Rising Stargirls program has achieved its goal of targeting girls from URM backgrounds while also reaching a diverse group of girls and welcoming everyone who expresses interest in the workshops.

9.2.2 Resources

Rising Stargirls has made two main resources publicly available to encourage the integration of arts-based activities in science curriculum outside of the Rising Stargirls programming: activity handbooks and educator webinars. Although these resources are not immediately applicable to the findings of the paper, they are described here to paint a more complete picture of the Rising Stargirls organization.

To encourage educators across the world to integrate creative arts-based strategies into scientific curricula in their own classrooms, Rising Stargirls publicly released *The Rising Stargirls Teaching and Activity Handbook*[8], written by Professor Shields. At the onset of the COVID-19 pandemic, this handbook was adapted by Maya Silverman to allow curriculum activities to be conducted via Zoom and similar online platforms[9]. In 2021, Jessica N. Howard de-

[8] You can access the handbook after filling out a short questionnaire at http://www.risingstargirls.org/teaching-and-activity-handbook-1

[9] You can access the Zoom adapted handbook after filling out a short questionnaire at http://www.risingstargirls.org/covid-19-virtual-teaching-and-activity-handbook

veloped five additional Rising Stargirls activities that can be conducted both virtually and in person. These activities are available in *The Rising Stargirls Teaching Activity Supplement*[10]. In 2021, Nina Robbins Blanch translated the *Rising Stargirls Teaching and Activity Handbook* to Spanish, now publicly available on the Rising Stargirls website[11].

These free handbooks lead educators through over 20 hours of arts-based astronomy activities developed by Rising Stargirls and borrowed with permission from other programs[12]. The original handbook guides educators through 10 days of working with middle-school girls including ice breakers and an end-of-program celebration. The handbook supplement leads educators through five additional creative arts-based astronomy activities. Each activity introduces a topic in astronomy or astrobiology and encourages exploration of the topic through a creative arts lens.

Since 2019, Rising Stargirls has hosted five webinars geared towards modeling how educators can incorporate the Rising Stargirls philosophy into their own outreach programs. Participating educators ranged from those growing their program to those with an established presence in the communities they serve. These two hour webinars complemented the publicly available *The Rising Stargirls Teaching and Activity Handbook*, as educators are guided by Rising Stargirls' facilitators through a selection of learner-centered activities included in the handbook, and taught how to develop these activities for in-person and virtual classroom environments. In addition, educators received access to further resources beyond *The Rising Stargirls Teaching and Activity Handbook*, including example workshop flyers, participant contracts, media and art consent and release forms, and directions to potential funding resources. These resources were distributed with the intent to be built upon and adapted by

[10] You can access the supplemental activities after filling out a short questionnaire at http://www.risingstargirls.org/teaching-and-activity-supplement

[11] You can access the Spanish language handbook after filling out a short questionnaire at http://www.risingstargirls.org/teaching-and-activity-handbook-en-espanol

[12] Drama-Based Instruction (DBI) Network, Drama For Schools, Eurekus, Improv Encyclopedia, NASA Astrobiology Institute "Life on Earth...and elsewhere?" Astrobiology Teaching Guide, NASA's Discovery and New Frontiers Programs, and Voyage: A Journey Through Our Solar System.

individual educators for the needs of their own outreach communities. In this way, the Rising Stargirls' philosophy extends beyond the direct endeavors of Rising Stargirls, and intersects with underserved communities alongside their target group of URM.

9.3 Methodology

Data for this work were collected using anonymous surveys to gauge participants feelings before and after attending a Rising Stargirls workshop. The next two subsections describe how data were collected and analyzed to produce the results in Section 9.4.

9.3.1 Data Collection

The data discussed in this section were originally collected as part of anonymous, program-improvement surveys conducted by Rising Stargirls between 2015 and 2023. We discuss the collection strategies used for this purpose. Data was collected voluntarily with no adverse consequences for participants who chose not to fill out the survey. All subsequent analysis was done on de-identified data.

During the three in-person workshops, surveys were administered audibly and collected using a physical piece of paper. Data were compiled and saved to a spreadsheet. The same survey, detailed below, was administered on the first and last day of the workshop. During the virtual workshop in the summer of 2021, the initial survey was administered visually via slides at the beginning of the second day of the workshop. For the initial survey, no survey results were collected but the participants were asked to write their answers in their notes. The final survey was administered via Google Form at the end of the last day of the workshop. Responses for how participants felt before and after the workshop were collected via a Google Form on the last day of the workshop. During the virtual workshops in the summers of 2022 and 2023, the initial survey was administered via Google Form at the end of the first day of the workshop. For the initial survey, survey results were collected but not used for research purposes. The final survey was administered via Google Form at the end of the last day of the workshop. Responses for how participants felt before and after the workshop were collected via a Google Form on the last day of the workshop.

The survey items comprised four statements:

1. I talk to my family and friends about science.
2. I like my science classes. (Altered to: I am excited to take my science classes in school.)[13]
3. I believe I can do well in science.
4. I see myself as a scientist.

Participants were asked to rate each statement on a Likert scale of one to six. For the first statement, the scale read: Never (1), Very Rarely (2), Rarely (3), Occasionally (4), Frequently (5), Very Frequently (6). For the second, third, and fourth statements, the scale read: Disagree Very Strongly (1), Disagree Strongly (2), Disagree (3), Agree (4), Agree Strongly (5), Agree Very Strongly (6).

Evaluation items were developed in consultation with the Science Education Department at the Harvard-Smithsonian Center for Astrophysics. They were based on the *Partnerships in Education and Resilience* Common Instrument Suite[14] (Noam et al., 2020) and the Persistence Research in Science and Engineering project (Hazari et al., 2013). Survey items one and two were developed to assess participants' engagement in science, while items three and four were developed to assess participants' science identity.

[13]Statement 2 was changed for the virtual workshops to better reflect participants' attitudes towards future science classes.

[14]https://www.pearinc.org/common-instrument-suite

While the workshops conducted were focused on astronomy education, we study participants engagement and identity in science more broadly. Formal astronomy classes are often not offered in middle schools. This makes it difficult to ask participants about their experience in astronomy classes. Furthermore, our hypothesis applies across the sciences and is not confined to astronomy. Therefore, the assessment questions were intentionally designed to evaluate participants' engagement with science and science identity.

Data from the in-person workshops were saved as the number or percentage of participants who answered a question with each response. For example, at the beginning of one of the workshops, 50% of participants stated that they rarely talked to their families and friends about science. In Winter 2015, 10 participants filled out the before survey and about 12 filled out the after survey. In Summer 2015, seven participants filled out the before and after surveys for question 1, six participants filled out the before survey for questions 2, 3 and 4, seven participants filled out the after survey for questions 2 and 3, and nine participants filled out the after survey for question 4. In Fall 2016, 9 participants filled out the before survey and 5 participants filled out the after survey. Inconsistencies in the number of participants who filled out the survey is due to the change in number of participants who attended on the first and last day of the workshops.

The data-collection strategies used in the virtual workshops allowed for more details in saved data since surveys were administered with a Google Form. Data from these workshops were recorded verbatim in the manner each participant responded to respective survey questions before and after the workshop. For example, one participant stated that they talked to their families and friends about science occasionally (4) before the workshop and frequently (5) after the workshop. The 2022 and 2023 virtual workshops included several returning participants (see Section 9.2.1). Their responses may be included in the data. In Summer 2021, 30 participants filled out the before and after survey. In Summer 2022, 15 participants filled out the before and after survey. In Summer 2023, 21 participants filled out the before

Summer 2021	Summer 2022	Summer 2023
Draw a scientist	Draw a scientist	Draw a scientist
When I look at the sky I think of...	When I look at the sky I think of...	When I look at the sky I think of...
Freewriting on Astro(biology)	Freewriting on Astro(biology)	Freewriting on Astro(biology)
Why does representation matter?	Why does representation matter?	Why does representation matter?
Constellations and origin stories	Constellations and origin stories	Constellations and origin stories
Art and the Cosmic Connection	Art and the Cosmic Connection	Art and the Cosmic Connection
Planet mnemonics	Telescopes and Kaleidoscopes	Telescopes and Kaleidoscopes
Share a woman of color astronomer	Share a woman of color astronomer	Share a woman of color astronomer
Drawing distance in me	Dark matter and hidden messages	Galaxies and their diversity
Create your very own exoplanet	Create your very own exoplanet	Create your very own exoplanet
Life's must-haves	Life's must-haves	Life's must-haves
PSA for life	PSA for life	PSA for life
My universe	My universe	The expansion of the universe

Table 9.2: Titles of activities taught in each virtual workshop. The details of the corresponding activities can be found in the Rising Stargirls handbooks discussed in Section 9.2.2.

and after survey.

9.3.2 Analysis

The data was analyzed using a Python (version 3.10.12) script that read data from CSV files. The goal of our analysis is to report how participants' engagement in and self-identity towards science changed over the duration of the workshop. Section 9.4 presents figures that show how participants responded to the four statements. We also discuss how these observed changes support our claims that Rising Stargirls workshops improve engagement with science and science identity among participants.

Data is analyzed cumulatively: data from all three in-person workshops are shown together and data from all three virtual workshops are shown together. Our results should not be dependent on the details that varied from workshop to workshop since they were run with similar arts-based activities (see Table 9.2 for details). However, we also analyze each workshop individually to comment on the general trend from workshop to workshop.

To quantitatively analyze the data we convert the Likert scale responses (1 to 6) to a numeric scale (0 to 5),[15] and then convert these scores to percentages e.g. "Very Frequently" corresponds to a numeric score of 5 which is converted to 100% while "Never" corresponds to a numeric score of 0 which is converted to 0%.

We consider three different metrics to compare participants' responses before and after the workshops: Gain of averages (Hake's Gain), $\langle g \rangle$ (Hake, 1998), normalized change, c (Marx & Cummings, 2007), and a nonparametric effect size measure, d_{A_w} (Li, 2016; Ruscio, 2008).

The gain of averages (Hake's Gain), $\langle g \rangle$ (Hake, 1998), is defined as

$$\langle g \rangle \equiv \frac{A_{\text{ave}} - B_{\text{ave}}}{100\% - B_{\text{ave}}}, \tag{9.1}$$

where A_{ave} is the average percent response after the workshop and B_{ave} is the average percent response before the workshop.

Normalized change, c (Marx & Cummings, 2007), is similar to Hake's gain but has several beneficial features such as being able to account for score losses and being more robust for

[15]Given that the Likert scale is fundamentally a set of discrete ordered categories, and not a continuous variable, it technically violates assumptions used in standard parametric statistical metrics. Thus, nonparametric statistical analyses are necessary, although they are generally considered less powerful (Bishop & Herron, 2015). As a result, in this work, we report both parametric (equations 9.1 and 9.2) and nonparametric metrics (equation 9.4).

small class sizes. However, it is limited in that it requires matched data (i.e. that we can match a participant's responses before the workshop to their responses after). It is defined as

$$c \equiv \begin{cases} \frac{r_{\mathrm{A,i}} - r_{\mathrm{B,i}}}{100\% - r_{\mathrm{B,i}}} & r_{\mathrm{A,i}} > r_{\mathrm{B,i}} \\ \text{dropped from calculation} & r_{\mathrm{A,i}} = r_{\mathrm{B,i}} = 100\% \text{ or } 0\% \\ 0 & r_{\mathrm{A,i}} = r_{\mathrm{B,i}} \\ \frac{r_{\mathrm{A,i}} - r_{\mathrm{B,i}}}{r_{\mathrm{B,i}}} & r_{\mathrm{A,i}} < r_{\mathrm{B,i}} \end{cases}, \tag{9.2}$$

where $r_{\mathrm{A,i}}$ ($r_{\mathrm{B,i}}$) is the percent score after (before) the workshop of participant i. c is then averaged over all participants which were not dropped from the calculation to get c_{ave}.

Since our data is non-normal, we estimate our effect size with the nonparametric effect size measure, d_{A_w} (Li, 2016), derived from the nonparametric estimator for CL, A_w (Ruscio, 2008), which is defined as

$$A_w \equiv \frac{\#\left(r_{\mathrm{A}} > r_{\mathrm{B}}\right) + 0.5\#\left(r_{\mathrm{A}} = r_{\mathrm{B}}\right)}{N_{\mathrm{A}} N_{\mathrm{B}}}, \tag{9.3}$$

where N_{A} (N_{B}) is the number of responses after (before) the workshop and $\#\left(\cdot\right)$ is the count function. Namely, for each after response, $r_{\mathrm{A,i}}$, $\#\left(r_{\mathrm{A,i}} > r_{\mathrm{B}}\right)$ counts the number of before responses which are less than $r_{\mathrm{A,i}}$. To better interpret this result, A_w can be converted into a $d-$metric via

$$d_{A_w} \equiv \sqrt{2}\Phi^{-1}\left(A_w\right), \tag{9.4}$$

where $\Phi^{-1}\left(\cdot\right)$ is the inverse normal cumulative distribution function (Li, 2016).

We calculate $\langle g \rangle$ and d_{A_w} for all workshop data but can only calculate c_{ave} on the matched virtual workshop data. The in-person data was saved cumulatively and anonymously, as described in Section 9.3.1, so it was impossible to link a participants' responses before the workshop to those after the workshop. Because it is unmatched, calculating c_{ave} on the in-person workshop data is not possible.

9.4 Results

In Sections 9.4.1 and 9.4.2 we discuss the results using data from Rising Stargirls' in-person and virtual workshops, respectively. The data are split between in-person and virtual workshops to study each method individually. Each method was studied individually to investigate the impact of slight differences in instruction media and curriculum between workshops, which may have slightly impacted interactions between participants. Furthermore, the collection method differed between the two workshop types, allowing for different analyses, as described in Section 9.3.2.

9.4.1 In-Person

Figure 9.1a demonstrates that, overall, participants engaged in more frequent discussions about science with their families and friends after participating in one of Rising Stargirls' in-person workshops. Responses from before the workshop are shown in pink and are on the left side of each response, and responses from after the workshop are shown in purple and are on the right side. We assigned numbers to participant responses, such that 0 (or 0%) corresponds to "Never" and 5 (or 100%) corresponds to "Very Frequently". We then compare before and after responses by calculating Hake's gain, $\langle g \rangle$, and the effect size, d_{A_w}, which are reported in Table 9.3 (see Section 9.3.2 for definitions). Looking at each

Assessment Item	Metric with Number of Responses	Winter '15	Summer '15	Fall '16	Total
I talk to my family and friends about science.	(N_B, N_A)	(10, 12)	(7, 7)	(9, 5)	(26, 24)
	d_{A_w}	0.2524	0.7583	0.8336	0.4268
	$\langle g \rangle$	0.0885	0.5000	0.2909	0.2344
I like my science classes.	(N_B, N_A)	(10, 12)	(6, 7)	(9, 5)	(25, 24)
	d_{A_w}	0.3279	0.1268	0.8336	0.4258
	$\langle g \rangle$	0.3561	0.2381	0.7000	0.4048
I believe I can do well in science.	(N_B, N_A)	(10, 13)	(6, 7)	(9, 5)	(25, 25)
	d_{A_w}	-0.2744	-0.2546	0.5238	-0.0255
	$\langle g \rangle$	-0.3077	-0.7143	0.3571	-0.0714
I see myself as a science person.	(N_B, N_A)	(10, 12)	(6, 9)	(9, 5)	(25, 26)
	d_{A_w}	0.9354	-0.9955	0.8336	0.4463
	$\langle g \rangle$	0.3382	-2.1110	0.2909	0.2582

Table 9.3: Statistical analysis of in-person workshop responses. Since these data are unmatched we report two statistical metrics: d_{A_w} (equation 9.4) and $\langle g \rangle$ (equation 9.1). The number of before, N_B, and after, N_A, responses used in these calculations are also reported. The sign of the value indicates a gain (+) or loss (-). A small effect is indicated by $|\langle g \rangle| < 0.30$ or $|d_{A_w}| \sim 0.20$. A moderate effect is indicated by $0.30 \leq |\langle g \rangle| < 0.70$ or $|d_{A_w}| \sim 0.50$. A large effect is indicated by $0.70 \leq |\langle g \rangle|$ or $|d_{A_w}| \sim 0.80$.

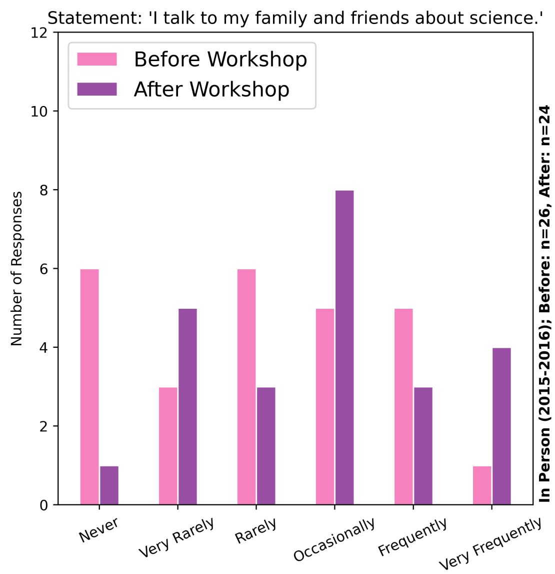

(a) "I talk to my family and friends about science." Responses range from "Never" with a numerical value of 0 (or 0%) to "Very Frequently" with a numerical value of 5 (or 100%).

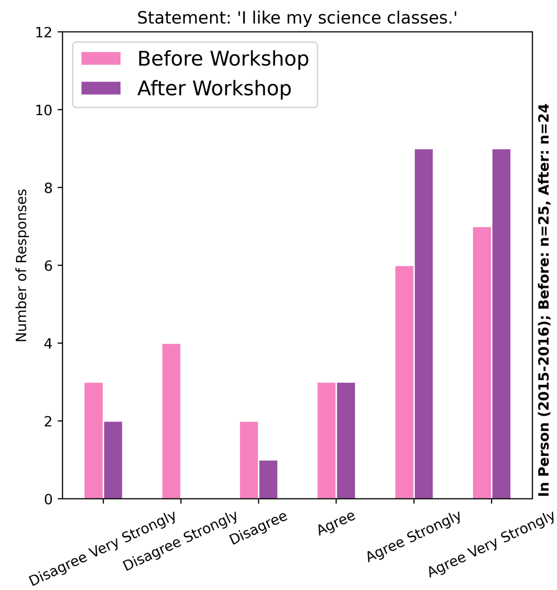

(b) "I like my science classes." Responses range from "Disagree very strongly" with a numerical value of 0 (or 0%) to "Agree very strongly" with a numerical value of 5 (or 100%).

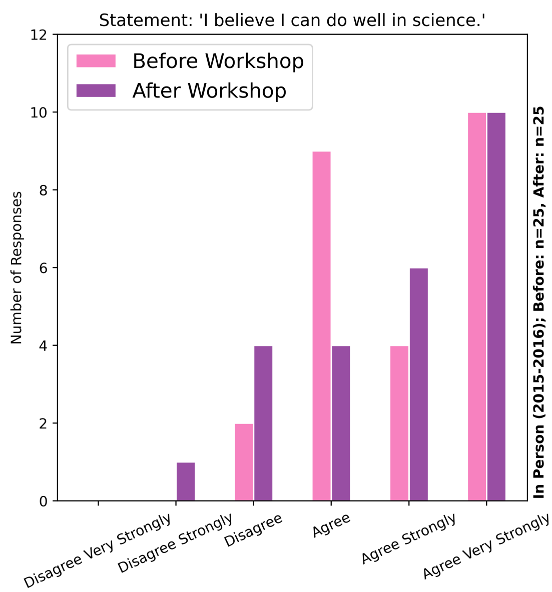

(c) "I believe I can do well in science." Responses range from "Disagree very strongly" with a numerical value of 0 (or 0%) to "Agree very strongly" with a numerical value of 5 (or 100%).

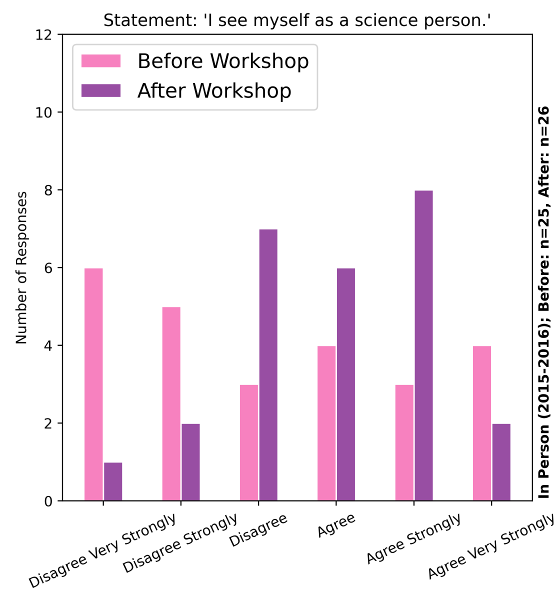

(d) "I see myself as a science person." Responses range from "Disagree very strongly" with a numerical value of 0 (or 0%) to "Agree very strongly" with a numerical value of 5 (or 100%).

Figure 9.1: Compiled data from three in-person workshops that took place in Winter 2015, Summer 2015, and Fall 2016. The y-axis shows how many participants responded to the statement for each response. Responses from before the workshop are shown in pink and are on the left side of each response, and responses from after the workshop are shown in purple and are on the right side.

workshop individually, there was a small to moderate increase in the frequency with which participants talked to their families and friends about science. Collectively analyzing all in-person workshop responses $(N_B, N_A) = (26, 24)$ showed a small gain $\langle g \rangle = 0.2344$ and small-to-moderate effect size of $d_{A_w} = 0.4268$.

Figure 9.1b demonstrates that, overall, participants stated that they liked their science classes with stronger agreement after participating in one of Rising Stargirls' in-person workshops. We assigned numbers to participant responses, such that 0 (or 0%) corresponds to "Disagree Very Strongly" and 5 (or 100%) corresponds to "Agree Very Strongly". We then compare before and after responses by calculating Hake's gain, $\langle g \rangle$, and the effect size, d_{A_w}, which are reported in Table 9.3 (see Section 9.3.2 for definitions). Looking at each workshop individually, there was a small to moderate increase in the degree to which participants liked their science classes. Collectively analyzing all in-person workshop responses $(N_B, N_A) = (25, 24)$ showed a moderate gain $\langle g \rangle = 0.4048$ and small-to-moderate effect size of $d_{A_w} = 0.4258$.

The increase in the frequency with which participants talked to their families and friends about science, as well as the increase in the agreement that they like their science classes, as shown in Figures 9.1a and 9.1b, indicates that participants' engagement in science increased over the course of Rising Stargirls' creative arts-based astronomy workshop.

Figure 9.1c demonstrates that, overall, participant's feelings of how well they believe they can do in science didn't change by a significant amount. Collectively analyzing all in-person workshop responses $(N_B, N_A) = (25, 25)$ showed a very slight decrease $\langle g \rangle = -0.0714$ and a very small effect size of $d_{A_w} = -0.0255$. While this is a slight decrease we note that this assessment item received the highest rated results of all items both before and after the in-person workshops. It is likely that their confidence in their ability to do well in science didn't increase because they came to the workshop already confident. Interestingly, the trend changed drastically between each individual workshop, ranging from large to moderate decreases to moderate increase. We note that the most recent in-person workshop, Fall 2016, had a moderate increase, potentially indicating that participants benefited from improved program implementation as the program facilitators gained experience.

Figure 9.1d demonstrates that, overall, participants saw themselves as a science person with stronger agreement after participating in one of Rising Stargirls' in-person workshops. Collectively analyzing all in-person workshop responses $(N_B, N_A) = (25, 26)$ showed a small increase $\langle g \rangle = 0.2582$ and a small-to-moderate effect size of $d_{A_w} = 0.4463$. Individually, this trend also changed somewhat between workshops. Both the Winter 2015 and Fall 2016 workshops aligned with the collective result, showing moderate to small increases, respectively. However, the Summer 2015 workshop strongly deviated, showing a large decrease. We note that this deviation may be partially due to the fact that this workshop had 3 more responses for the after survey ($(N_B, N_A) = (6, 9)$).

Overall, the increase in agreement that participants saw themselves as a science person, shown in Figure 9.1d, indicates that participants positively developed their science identities over the course of Rising Stargirls' creative arts-based astronomy workshop.

9.4.2 Virtual

The virtual workshops varied slightly from the in-person workshops due to their virtual nature. Fewer theater exercises were included since many such activities demand face-to-face interactions. While virtual workshop participants were encouraged to use cameras to engage in face-to-face interactions, not all participants had access to technology allowing for face-to-face interactions. In addition to impacting the curriculum, the virtual nature also impacted the level of interactions between participants. In the in-person workshops, participants often knew each other already, and were able to interact with each other throughout the workshop. In the virtual workshops, participants did not know any other participants before

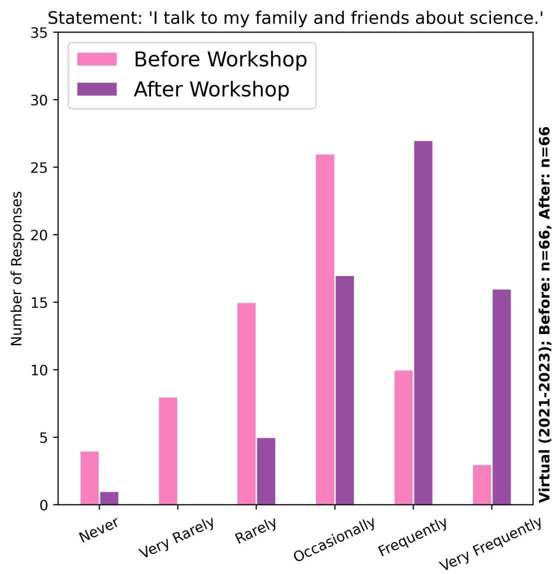

(a) "I talk to my family and friends about science." Responses range from "Never" with a numerical value of 0 (or 0%) to "Very Frequently" with a numerical value of 5 (or 100%).

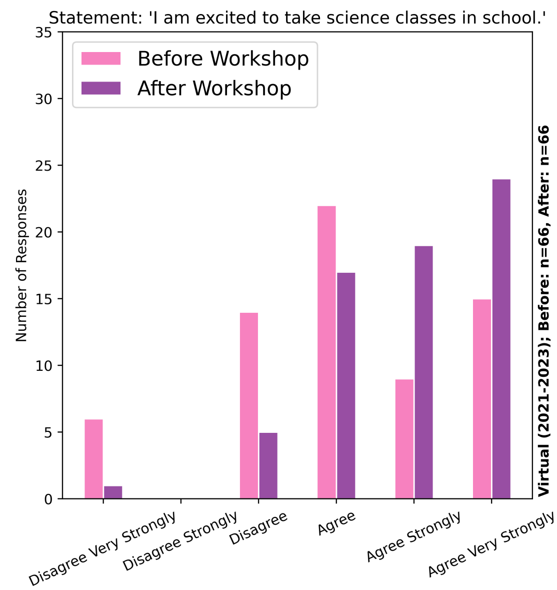

(b) "I am excited to take science classes in school." Responses range from "Disagree very strongly" with a numerical value of 0 (or 0%) to "Agree very strongly" with a numerical value of 5 (or 100%).

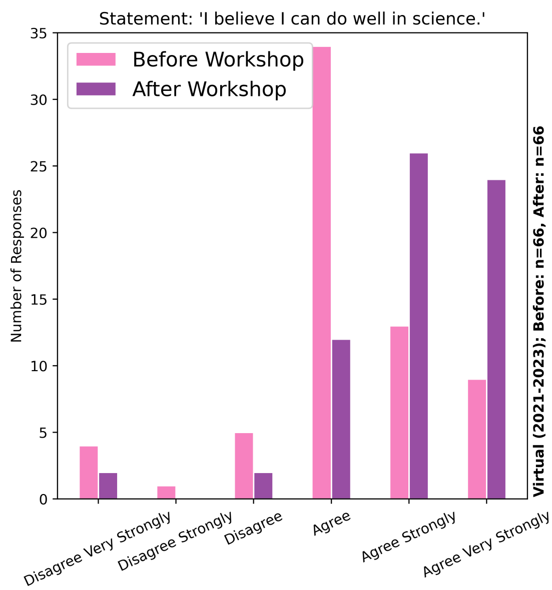

(c) "I believe I can do well in science." Responses range from "Disagree very strongly" with a numerical value of 0 (or 0%) to "Agree very strongly" with a numerical value of 5 (or 100%).

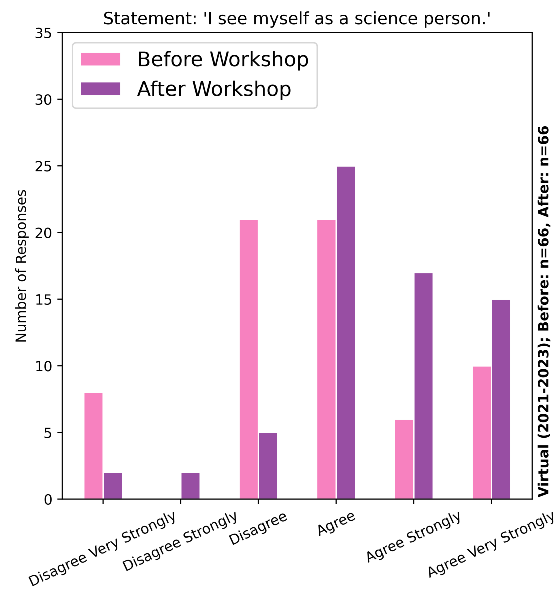

(d) "I see myself as a science person." Responses range from "Disagree very strongly" with a numerical value of 0 (or 0%) to "Agree very strongly" with a numerical value of 5 (or 100%).

Figure 9.2: Compiled data from three virtual workshops that took place in Summer 2021, Summer 2022, and Summer 2023. The y-axis shows how many participants responded to the statement for each response. Responses from before the workshop are shown in pink and are on the left side of each response, and responses from after the workshop are shown in purple and are on the right side.

Assessment Item	Metric with # of Responses	Summer '21	Summer '22	Summer '23	Total
I talk to my family and friends about science.	(N_B, N_A)	(30, 30)	(15, 15)	(21, 21)	(66, 66)
	d_{A_w}	1.3400	1.0500	0.8625	1.0700
	$\langle g \rangle$	0.5846	0.4186	0.4314	0.4906
	c_{ave} (# dropped)	0.6034 (1)	0.4189 (0)	0.3921 (2)	0.4958 (3)
I am excited to take science classes in school.	(N_B, N_A)	(30, 30)	(15, 15)	(21, 21)	(66, 66)
	d_{A_w}	0.8786	0.3909	0.4708	0.5900
	$\langle g \rangle$	0.5385	0.2667	0.3721	0.4160
	c_{ave} (# dropped)	0.5417 (6)	0.3091 (4)	0.3222 (6)	0.4247 (16)
I believe I can do well in science.	(N_B, N_A)	(30, 30)	(15, 15)	(21, 21)	(66, 66)
	d_{A_w}	1.1460	0.3016	0.9213	0.8201
	$\langle g \rangle$	0.5472	0.2593	0.4500	0.4500
	c_{ave} (# dropped)	0.5617 (3)	0.4875 (7)	0.4450 (1)	0.5085 (11)
I see myself as a science person.	(N_B, N_A)	(30, 30)	(15, 15)	(21, 21)	(66, 66)
	d_{A_w}	1.0710	0.3097	0.4285	0.6235
	$\langle g \rangle$	0.4545	0.2105	0.2766	0.3377
	c_{ave} (# dropped)	0.5000 (4)	0.2242 (4)	0.2314 (4)	0.3593 (12)

Table 9.4: Statistical analysis of virtual workshop responses. Since these data are matched we report three statistical metrics: d_{A_w} (equation 9.4), $\langle g \rangle$ (equation 9.1), and c_{ave} (equation 9.2). For c_{ave}, the number of responses dropped from the calculation are indicated in parentheses. The number of before, N_B, and after, N_A, responses used in these calculations are also reported. The sign of the value indicates a gain (+) or loss (-). A small effect is indicated by c_{ave} or $|\langle g \rangle| < 0.30$ or $|d_{A_w}| \sim 0.20$. A moderate effect is indicated by $0.30 \leq c_{ave}$ or $|\langle g \rangle| < 0.70$ or $|d_{A_w}| \sim 0.50$. A large effect is indicated by $0.70 \leq c_{ave}$ or $|\langle g \rangle|$ or $|d_{A_w}| \sim 0.80$.

the workshop, and interacted with each other via chat, voice, and occasionally with video. Additionally, as described in Section 9.3.1, the data collection strategy changed for virtual workshops. These differences may have impacted the following results.

To quantitatively analyze responses, we assigned numbers to each response such that 0 (or 0%) corresponds to "Never" and 5 (or 100%) corresponds to "Very Frequently". We then compare before and after responses by calculating Hake's gain, $\langle g \rangle$, and the effect size, d_{A_w}. Additionally, due to differences in collection strategies, the before and after virtual workshop responses are matched. This allows us to also calculate the normalized change, c_{ave}. These metrics are reported in Table 9.4 (see Section 9.3.2 for definitions).

Figure 9.2a demonstrates that, overall, participants engaged in more frequent discussions about science with their families and friends after taking part in one of Rising Stargirls' virtual workshops. Collectively analyzing all virtual workshop responses $(N_B, N_A) = (66, 66)$ to the question 'I talk to my family and friends about science' showed a moderate increase $\langle g \rangle = 0.4906$ and $c_{ave} = 0.4958$ (with 3 responses dropped from the calculation), as well as a large effect size $d_{A_w} = 1.0700$. The same trends hold for each individual virtual workshop.

Figure 9.2b demonstrates that, overall, participants were more excited to take science classes in school after participating in one of Rising Stargirls' virtual workshop. Collectively analyzing all virtual workshop responses $(N_B, N_A) = (66, 66)$ to the question 'I am excited to take science classes in school' showed a moderate increase $\langle g \rangle = 0.4160$ and $c_{ave} = 0.4247$ (with 16 responses dropped from the calculation), as well as a moderate-to-large effect size $d_{A_w} = 0.5900$. Each individual workshop shows similar trends with the Summer 2022 and Summer 2023 workshops showing slightly less increase across all metrics and the Summer 2021 workshop showing slightly more increase across all metrics.

The increase in the frequency with which participants talked to their families and friends about science, as well as the increase in their excitement to take science classes in school, as shown *in Figures 9.2a and 9.2b, indicates that participants' engagement with science increased over the course of Rising Stargirls' virtual creative arts-based astronomy workshop.*

Figure 9.2c demonstrates that, overall, participants believed that they could do well in science more strongly after participating in one of Rising Stargirls' virtual workshops. Collectively analyzing all virtual workshop responses $(N_B, N_A) = (66, 66)$ to the question 'I believe I can do well in science' showed a moderate increase $\langle g \rangle = 0.4500$ and $c_{ave} = 0.5085$ (with 11 responses dropped from the calculation), as well as a large effect size $d_{A_w} = 0.8201$. Individually, the Summer 2021 and Summer 2023 workshops show the same increase and the Summer 2022 workshop shows slightly less increase across all metrics.

Figure 9.2d demonstrates that, overall, participants saw themselves as a science person with stronger agreement after participating in one of Rising Stargirls' virtual workshops. Collectively analyzing all virtual workshop responses $(N_B, N_A) = (66, 66)$ to the question 'I see myself as a science person' showed a moderate increase $\langle g \rangle = 0.3377$ and $c_{ave} = 0.3593$ (with 12 responses dropped from the calculation), as well as a large effect size $d_{A_w} = 0.6235$. Each individual workshop shows similar trends with the Summer 2022 and Summer 2023 workshops showing slightly less increase across all metrics and the Summer 2021 workshop showing slightly more increase across all metrics.

The increase in participants' belief in their capability to succeed in science, as well as the increase in agreement with which participants saw themselves as a science person, shown in Figures 9.2c and 9.2d, indicates that participants positively developed their science identities over the course of Rising Stargirls' virtual creative arts-based astronomy workshop.

We conducted an equivalent analysis on each of the virtual workshops individually to discuss any anomalies and trends. Table 9.4, shows that there is no clear trend from the earlier to later workshops across all four survey items on average. Rising Stargirls will continue tracking this trend for future workshops with the hope to produce more conclusive results on how the average percentage increase in participants' answers changes as the workshop progresses.

Additionally, for these workshops, since data was collected for each participant, we were able to track how a participant's response to each statement changed over the course of the workshop. Therefore, Table 9.4 also shows the normalized change, c_{ave}, calculated using matched before and after responses from each participant for each individual workshop. In general, this largely agrees with the results of calculating Hake's gain, $\langle g \rangle$ on this dataset.

9.5 Discussion

This study emphasizes the advantages of fostering creativity in informal science education for middle-school girls from underrepresented groups in the sciences. By analyzing participants' sentiments before and after taking part in a creative arts-based astronomy workshop run by Rising Stargirls, our results illustrate how encouraging middle-school girls to infuse the creative arts into science cultivates their science identity and encourages increased engagement with science. Science identity is assessed by asking participants whether they believe they can do well in science and if they see themselves as scientists. Engagement with science is evaluated by asking participants if they talk about science and if they enjoy their science classes.

Across all six workshops studied in this work, our results show that participants' engagement with science and science identity increased over the course of Rising Stargirls' creative arts-based astronomy workshops. Participants both talked to their families and friends about science more frequently and were more excited to take science classes in school after participating in one of Rising Stargirls' workshops. This indicates that participants' engagement with science increased over the course of Rising Stargirls' in-person and virtual workshops. Participants reported an increased belief in their ability to succeed in science and also in their identity as a science person. This indicates that participants' science identities increased over the course of Rising Stargirls' in-person and virtual workshops.

The workshop that took place in Summer 2015 has anomalously low gain and effect size. At one week long, this was Rising Stargirls' shortest workshop. We suspect this low improvement in confidence and enthusiasm towards their perceived science abilities is due to the lower relative amount of time available to change their opinions. Alternatively, this could indicate that Rising Stargirls workshops improved over time and participants were positively impacted. These could be reasons why it is deviating from the trend seen in other in person workshops. However, the low gain and effect size in this workshop does not change the overall trend seen in Figure 9.1 and Table 9.3.

9.5.1 Limitations

We acknowledge the limitations of retrospective pre- and post-surveys, where participants were asked to measure how they felt before and after the workshop on the final day. This depends on a participant's memory recall, and the potential for participants to exhibit self enhancement bias (Miller et al., 2023). Alternatively, a pre-survey administered on the first day of the workshop, followed by a post-survey administered on the final day, would provide measurements not subject to inconsistencies within memory recall and allows educators to track participant engagement from the onset of the workshop (Miller et al., 2023). However, prior to the workshop, participants are likely to mischaracterize their comfort level with topics based on lack of exposure to overarching concepts (Miller et al., 2023). Once participants are introduced to the topics, in an active learning environment, they are more accurately able to describe the scope of what they did not know in comparison to what they have now learned (Miller et al., 2023). The workshop experience changes the metric by which participants assess themselves relative to what they thought they knew prior to the experience.

While our in-person workshops administered surveys on the first and last days of the workshop, ultimately, retrospective pre- and post-surveys were selected for the virtual workshops to decrease this response shift bias. The difference in survey administration over in-person and virtual workshops may lead to biases in our analysis and conclusions.

While our overall goal is to highlight the benefits of creative arts-based astronomy activities specifically for girls from URM groups, this study emphasizes the impacts on middle-school girls of *all* colors and backgrounds. This choice was made to protect participant anonymity by ensuring that demographic information was not linked to survey responses. However, Rising Stargirls outreach efforts were designed to increase the participation of URM groups. As a result, URM individuals made up 60% of the total workshop attendees. We acknowledge the value of understanding the impact on specific URM groups and will analyze this trend in future studies. This will allow us to explore which URM group benefited the most from creative arts-based astronomy workshops.

This study is limited by the number of workshops run, both in-person and virtually. With three in-person workshops and three virtual workshops, we are able to show conclusive evidence that participants' engagement with science and their science identity increased over the duration of Rising Stargirls' creative arts-based astronomy workshop. However, data from more workshops would allow us to make robust conclusions on how the increase in participants' responses changes across workshops. Rising Stargirls will continue to collect data as it runs future in-person and virtual workshops and we plan to conduct this analysis in more detail as soon as the data are available.

This study is also limited by the time spent with each group of participants. Rising Stargirls' workshops were about two weeks long on average, totalling about 20 hours. Participants would further benefit from creative arts-based astronomy activities sustained over a longer period of time. Developing confidence and enthusiasm for their science ability is not a one-and-done process. In the future, Rising Stargirls plans to run both in-person and virtual workshops over a longer period of time and develop specific programming for returning participants. Specific programming for returning participants would allow for the development of girls' science identities to be tracked over multiple years, as they continue to engage in creative arts-based astronomy activities.

The final limitation that we identify with regards to this work is that we do not have a control group. An example control group would consist of middle-school students who do not participate in a Rising Stargirls workshop.

9.5.2 Conclusion

In conclusion, this work demonstrates how encouraging middle-school girls to bring their own personal creativity, as expressed through the arts, to the study of astronomy promotes engagement with science and development of a science identity. The data from six separate creative arts-based astronomy workshops exhibits the progression of girls' science identities and their engagement with science. These outcomes underscore the value of nurturing creativity and integrating the arts into astronomy education.

9.6 Availability of source code and requirements

Code used to analyze data presented in this work is available upon reasonable request to the authors.

9.7 Declarations

9.7.1 List of abbreviations

- COVID-19 - coronavirus disease of 2019
- CSV - comma-separated values
- NASA - National Aeronautics and Space Administration
- NSF - National Science Foundation
- PhD - Doctor of Philosophy
- STEAM - science, technology, engineering, arts, and math
- STEM - science, technology, engineering, and math
- URM - underrepresented minorities, defined in this work as American Indian or Alaska Native, Black or African-American, Hispanic or Latinx, Native Hawaiian or other Pacific Islander.
- YWCA - Young Women's Christian Association

9.7.2 Ethical Approval

This research project has received ethical approval from the University of California, Irvine Institutional Review Board (IRB) under Protocol Number 2550 with University of California, Santa Barbara as a relying institution. The ethical approval granted by the IRB signifies that this research complies with established ethical standards, ensuring the protection of the rights, well-being, and confidentiality of all human participants involved in the study.

9.7.3 Competing Interests

AS and JNH declare a non-financial conflict of interest in relation to the current study. AS holds the copyrighted *Rising Stargirls Teaching and Activity Handbook* and JNH holds the copyrighted *Rising Stargirls Teaching Activity Supplement*. These handbooks have been developed for educational purposes and provide resources to support the learning and engagement of participants in Rising Stargirls' programs. The content of the handbooks are referenced in the context of the study, but this conflict of interest does not involve any financial considerations.

MS, VV, and KW disclose a non-financial conflict of interest in connection with the current study. They have each been actively engaged in organizing and conducting Rising Stargirls workshops. Their involvement includes planning, facilitating, and developing curricula for these workshops. The knowledge and insights gained from their experience with Rising Stargirls may influence the interpretation of findings or discussions related to the workshops in this study. However, this conflict of interest does not involve any financial interests or considerations.

9.7.4 Acknowledgements

This material is based upon work supported by the National Science Foundation, under Award 1753373, by the Heising-Simons Fondation under Award 2023-4634, and by a Clare Boothe Luce Professorship, supported by the Henry Luce Foundation. JNH acknowledges support by the National Science Foundation under Grant No. DGE-1839285 and NSF PHY-1748958, and by the Gordon and Betty Moore Foundation through Grant No. GBMF7392. We give our deepest gratitude to everyone involved in running the six Rising Stargirls workshops discussed in this work. In particular, we thank Loraine Sandoval Ascencio, Christina Dinh, Helena Garcia Escuerdo, Max Fieg, Patricia Fofie, Daniela Gonzalez, and Mei Lin for their instrumental help in running Rising Stargirls' virtual workshops. MS thanks Professor Laura Tucker for her early guidance in conducting science education research. AS thanks Mary Dussault at the Science Education Department at the Harvard-Smithsonian Center for Astrophysics for science education mentoring and help implementing pre- and post-survey assessment strategies into Rising Stargirls program workshops.

Bibliography

Ade, P. A. R., Aghanim, N., Armitage-Caplan, C., et al. 2014, Astronomy &; Astrophysics, 571, A16, doi: 10.1051/0004-6361/201321591

Adhikari, S., Dalal, N., & Chamberlain, R. T. 2014, Journal of Cosmology and Astroparticle Physics, 2014, 019–019, doi: 10.1088/1475-7516/2014/11/019

Aghanim, N., Akrami, Y., Ashdown, M., et al. 2020, Astronomy & Astrophysics, 641, A6, doi: 10.1051/0004-6361/201833910

Alam, S., Aubert, M., Avila, S., et al. 2021, Physical Review D, 103, doi: 10.1103/physrevd.103.083533

Alexander, W. 2005, Astronomy Education Review, 3, 179

Andrade, K. E., Minor, Q., Nierenberg, A., & Kaplinghat, M. 2019, Monthly Notices of the Royal Astronomical Society, 487, 1905–1926, doi: 10.1093/mnras/stz1360

Arkani-Hamed, N., Finkbeiner, D. P., Slatyer, T. R., & Weiner, N. 2009, Physical Review D, 79, doi: 10.1103/physrevd.79.015014

Arora, A., Sanderson, R. E., Chakrabarti, S., et al. 2024, The Astrophysical Journal, 974, 223, doi: 10.3847/1538-4357/ad71c4

Bahcall, N. A., Ostriker, J. P., Perlmutter, S., & Steinhardt, P. J. 1999, Science, 284, 1481, doi: 10.1126/science.284.5419.1481

Balberg, S., & Shapiro, S. L. 2002, Physical Review Letters, 88, doi: 10.1103/physrevlett.88.101301

Balberg, S., Shapiro, S. L., & Inagaki, S. 2002, Astrophys. J., 568, 475, doi: 10.1086/339038

Baptista, J., Sanderson, R., Huber, D., et al. 2023, The Astrophysical Journal, 958, 44, doi: 10.3847/1538-4357/acea79

Behroozi, P. S., Wechsler, R. H., & Wu, H.-Y. 2013, The Astrophysical Journal, 762, 109

Behroozi, P. S., Wechsler, R. H., Wu, H.-Y., et al. 2013, , 763, 18, doi: 10.1088/0004-637X/763/1/18

Benson, A. J., Frenk, C. S., Lacey, C. G., Baugh, C. M., & Cole, S. 2002, Mon. Not. Roy. Astron. Soc., 333, 177, doi: 10.1046/j.1365-8711.2002.05388.x

Bishop, P., & Herron, R. 2015, International Journal of Exercise Science, 8, Article 10

Boddy, K. K., Feng, J. L., Kaplinghat, M., & Tait, T. M. 2014, Physical Review D, 89, doi: 10.1103/physrevd.89.115017

Bose, S., Deason, A. J., Belokurov, V., & Frenk, C. S. 2020, Monthly Notices of the Royal Astronomical Society, 495, 743, doi: 10.1093/mnras/staa1199

Boylan-Kolchin, M., Bullock, J. S., & Kaplinghat, M. 2011, Mon. Not. Roy. Astron. Soc., 415, L40, doi: 10.1111/j.1745-3933.2011.01074.x

—. 2012, Mon. Not. Roy. Astron. Soc., 422, 1203, doi: 10.1111/j.1365-2966.2012.20695.x

Brooks, A. M., & Zolotov, A. 2014, Astrophys. J., 786, 87, doi: 10.1088/0004-637X/786/2/87

Bullock, J. S., & Boylan-Kolchin, M. 2017, Ann. Rev. Astron. Astrophys., 55, 343, doi: 10.1146/annurev-astro-091916-055313

Bullock, J. S., Kravtsov, A. V., & Weinberg, D. H. 2000, The Astrophysical Journal, 539, 517–521, doi: 10.1086/309279

Chakrabarti, S., Chang, P., Price-Whelan, A. M., et al. 2019, The Astrophysical Journal, 886, 67, doi: 10.3847/1538-4357/ab4659

Chakrabarti, S., Wright, J., Chang, P., et al. 2020, The Astrophysical Journal Letters, 902, L28, doi: 10.3847/2041-8213/abb9b5

Chan, T. K., Kereš, D., Oñorbe, J., et al. 2015, Monthly Notices of the Royal Astronomical Society, 454, 2981–3001, doi: 10.1093/mnras/stv2165

Colin, P., Avila-Reese, V., Valenzuela, O., & Firmani, C. 2002, The Astrophysical Journal, 581, 777–793, doi: 10.1086/344259

Correa, C. A. 2021, Monthly Notices of the Royal Astronomical Society, 503, 920–937, doi: 10.1093/mnras/stab506

Crider, A., & Weston, A. 2012, Astronomy Education Review, 11, 010202

Dave, R., Spergel, D. N., Steinhardt, P. J., & Wandelt, B. D. 2001, The Astrophysical Journal, 547, 574–589, doi: 10.1086/318417

Diemand, J., Kuhlen, M., & Madau, P. 2007, The Astrophysical Journal, 667, 859–877, doi: 10.1086/520573

Diemer, B. 2018, The Astrophysical Journal Supplement Series, 239, 35, doi: 10.3847/1538-4365/aaee8c

Diemer, B., & Kravtsov, A. V. 2014, The Astrophysical Journal, 789, 1, doi: 10.1088/0004-637x/789/1/1

Dooley, G. A., Peter, A. H. G., Yang, T., et al. 2017, Monthly Notices of the Royal Astronomical Society, 471, 4894–4909, doi: 10.1093/mnras/stx1900

Driver, S. P., Hill, D. T., Kelvin, L. S., et al. 2011, Monthly Notices of the Royal Astronomical Society, 413, 971–995, doi: 10.1111/j.1365-2966.2010.18188.x

Drlica-Wagner, A., et al. 2015, Astrophys. J., 813, 109, doi: 10.1088/0004-637X/813/2/109

Drlica-Wagner, A., Bechtol, K., Mau, S., et al. 2020, The Astrophysical Journal, 893, 47, doi: 10.3847/1538-4357/ab7eb9

Dubinski, J., & Carlberg, R. G. 1991, Astrophys. J., 378, 496, doi: 10.1086/170451

D'Onghia, E., & Burkert, A. 2003, The Astrophysical Journal, 586, 12–16, doi: 10.1086/367606

Ebisu, T., Ishiyama, T., & Hayashi, K. 2022, Phys. Rev. D, 105, 023016, doi: 10.1103/PhysRevD.105.023016

Elbert, O. D., Bullock, J. S., Kaplinghat, M., et al. 2018, "The Astrophysical Journal", 853, 109, doi: 10.3847/1538-4357/aa9710

Essig, R., Mcdermott, S. D., Yu, H.-B., & Zhong, Y.-M. 2019, Phys. Rev. Lett., 123, 121102, doi: 10.1103/PhysRevLett.123.121102

Feldmann, R., Quataert, E., Faucher-Giguère, C.-A., et al. 2023, Monthly Notices of the Royal Astronomical Society, 522, 3831–3860, doi: 10.1093/mnras/stad1205

Feng, J. L., Kaplinghat, M., Tu, H., & Yu, H.-B. 2009, Journal of Cosmology and Astroparticle Physics, 2009, 004–004, doi: 10.1088/1475-7516/2009/07/004

Firmani, C., D'Onghia, E., Avila-Reese, V., Chincarini, G., & Hernandez, X. 2000, Monthly Notices of the Royal Astronomical Society, 315, L29–L32, doi: 10.1046/j.1365-8711.2000.03555.x

Fischer, M. S., Brüggen, M., Schmidt-Hoberg, K., et al. 2021, Monthly Notices of the Royal Astronomical Society, 505, 851–868, doi: 10.1093/mnras/stab1198

—. 2022, Monthly Notices of the Royal Astronomical Society, 516, 1923–1940, doi: 10.1093/mnras/stac2207

Fitts, A., et al. 2017, Mon. Not. Roy. Astron. Soc., 471, 3547, doi: 10.1093/mnras/stx1757

Fitts, A., Boylan-Kolchin, M., Bozek, B., et al. 2019, Monthly Notices of the Royal Astronomical Society, 490, 962–977, doi: 10.1093/mnras/stz2613

Flores, R. A., & Primack, J. R. 1994, The Astrophysical Journal, 427, L1, doi: 10.1086/187350

Freeman, K. C. 1970, , 160, 811, doi: 10.1086/150474

Fritz, T. K., Battaglia, G., Pawlowski, M. S., et al. 2018, Astronomy & Astrophysics, 619, A103, doi: 10.1051/0004-6361/201833343

Gad-Nasr, S., Boddy, K. K., Kaplinghat, M., Outmezguine, N. J., & Sagunski, L. 2023, On the Late-Time Evolution of Velocity-Dependent Self-Interacting Dark Matter Halos. https://arxiv.org/abs/2312.09296

Garland, C., & Ratay, D. 2007, Astronomy Education Review, 6, 59

Garrison-Kimmel, S., Boylan-Kolchin, M., Bullock, J. S., & Kirby, E. N. 2014, Mon. Not. Roy. Astron. Soc., 444, 222, doi: 10.1093/mnras/stu1477

Garrison-Kimmel, S., Wetzel, A., Bullock, J. S., et al. 2017, Monthly Notices of the Royal Astronomical Society, 471, 1709–1727, doi: 10.1093/mnras/stx1710

Gelato, S., & Sommer-Larsen, J. 1999, Monthly Notices of the Royal Astronomical Society, 303, 321–328, doi: 10.1046/j.1365-8711.1999.02223.x

Governato, F., Brook, C., Mayer, L., et al. 2010, Nature, 463, 203, doi: 10.1038/nature08640

Grand, R. J. J., Marinacci, F., Pakmor, R., et al. 2021, Monthly Notices of the Royal Astronomical Society, 507, 4953–4967, doi: 10.1093/mnras/stab2492

Graus, A. S., Bullock, J. S., Kelley, T., et al. 2019, , 488, 4585, doi: 10.1093/mnras/stz1992

Green, S. B., van den Bosch, F. C., & Jiang, F. 2021, Monthly Notices of the Royal Astronomical Society, 503, 4075, doi: 10.1093/mnras/stab696

Guo, Q., White, S., Boylan-Kolchin, M., et al. 2011, Monthly Notices of the Royal Astronomical Society, 413, 101–131, doi: 10.1111/j.1365-2966.2010.18114.x

Gurian, A. 2012, NYU Child Study Center. http://www.education.com

Hachisu, I., Nakada, Y., Nomoto, K., & Sugimoto, D. 1978, Progress of Theoretical Physics, 60, 393, doi: 10.1143/PTP.60.393

Hahn, O., & Abel, T. 2011, Monthly Notices of the Royal Astronomical Society, 415, 2101, doi: 10.1111/j.1365-2966.2011.18820.x

Hake, R. 1998, Am. J. Phys., 66, 64

Hayashi, K., Chiba, M., & Ishiyama, T. 2020, Astrophys. J., 904, 45, doi: 10.3847/1538-4357/abbe0a

Hazari, Z., Sadler, P. M., & Sonnert, G. 2013, The Journal of College Science Teaching, 42, 82. https://api.semanticscholar.org/CorpusID:150221716

Hopkins, P. F. 2015, Monthly Notices of the Royal Astronomical Society, 450, 53, doi: 10.1093/mnras/stv195

Hopkins, P. F., Kereš, D., Oñorbe, J., et al. 2014, Monthly Notices of the Royal Astronomical Society, 445, 581–603, doi: 10.1093/mnras/stu1738

Hopkins, P. F., Wetzel, A., Kereš, D., et al. 2018a, , 480, 800–863, doi: 10.1093/mnras/sty1690

—. 2018b, Monthly Notices of the Royal Astronomical Society, 480, 800–863, doi: 10.1093/mnras/sty1690

Hu, W., Barkana, R., & Gruzinov, A. 2000, Phys. Rev. Lett., 85, 1158, doi: 10.1103/PhysRevLett.85.1158

Jackson, R. A., Kaviraj, S., Yi, S. K., et al. 2024, The formation of cores in galaxies across cosmic time – the existence of cores is not in tension with the LCDM paradigm. https://arxiv.org/abs/2310.13055

Jethwa, P., Erkal, D., & Belokurov, V. 2017, Monthly Notices of the Royal Astronomical Society, 473, 2060, doi: 10.1093/mnras/stx2330

Jiang, F., Dekel, A., Freundlich, J., et al. 2021a, Monthly Notices of the Royal Astronomical Society, 502, 621, doi: 10.1093/mnras/staa4034

Jiang, F., Kaplinghat, M., Lisanti, M., & Slone, O. 2021b, arXiv:2108.03243. http://arxiv.org/abs/2108.03243

Jiang, F., Benson, A., Hopkins, P. F., et al. 2023, Monthly Notices of the Royal Astronomical Society, 521, 4630–4644, doi: 10.1093/mnras/stad705

Kahlhoefer, F., Kaplinghat, M., Slatyer, T. R., & Wu, C.-L. 2019, , 2019, 010, doi: 10.1088/1475-7516/2019/12/010

Kahlhoefer, F., Schmidt-Hoberg, K., Frandsen, M. T., & Sarkar, S. 2013, Monthly Notices of the Royal Astronomical Society, 437, 2865–2881, doi: 10.1093/mnras/stt2097

Kamada, A., Kaplinghat, M., Pace, A. B., & Yu, H.-B. 2017, Phys. Rev. Lett., 119, 111102, doi: 10.1103/PhysRevLett.119.111102

Kaplinghat, M., Keeley, R. E., Linden, T., & Yu, H.-B. 2014, Phys. Rev. Lett., 113, 021302, doi: 10.1103/PhysRevLett.113.021302

Kaplinghat, M., Tulin, S., & Yu, H.-B. 2016, Phys. Rev. Lett., 116, 041302, doi: 10.1103/PhysRevLett.116.041302

Kaplinghat, M., Valli, M., & Yu, H.-B. 2019, Mon. Not. Roy. Astron. Soc., 490, 231, doi: 10.1093/mnras/stz2511

Katz, N., & White, S. D. M. 1993, , 412, 455, doi: 10.1086/172935

Kauffmann, G., White, S. D. M., & Guiderdoni, B. 1993, Monthly Notices of the Royal Astronomical Society, 264, 201–218, doi: 10.1093/mnras/264.1.201

Kelley, T., Bullock, J. S., Garrison-Kimmel, S., et al. 2019, Mon. Not. Roy. Astron. Soc., 487, 4409, doi: 10.1093/mnras/stz1553

Kim, J.-h., Abel, T., Agertz, O., et al. 2013, The Astrophysical Journal Supplement Series, 210, 14, doi: 10.1088/0067-0049/210/1/14

Kim, S. Y., Peter, A. H., & Hargis, J. R. 2018, Physical Review Letters, 121, doi: 10.1103/physrevlett.121.211302

Kim, S. Y., & Peter, A. H. G. 2021, arXiv:2106.09050. http://arxiv.org/abs/2106.09050

Klein, C., Bullock, J. S., Xia, L., et al. 2025, The shape of FIREbox galaxies and a potential tension with low-mass disks. https://arxiv.org/abs/2503.05612

Klypin, A. A., Kravtsov, A. V., Valenzuela, O., & Prada, F. 1999, Astrophys. J., 522, 82, doi: 10.1086/307643

Klypin, A. A., Trujillo-Gomez, S., & Primack, J. 2011, The Astrophysical Journal, 740, 102, doi: 10.1088/0004-637x/740/2/102

Knollmann, S. R., & Knebe, A. 2009, The Astrophysical Journal Supplement Series, 182, 608–624, doi: 10.1088/0067-0049/182/2/608

Koda, J., & Shapiro, P. R. 2011, , 415, 1125, doi: 10.1111/j.1365-2966.2011.18684.x

Komatsu, E., Smith, K. M., Dunkley, J., et al. 2011, The Astrophysical Journal Supplement Series, 192, 18, doi: 10.1088/0067-0049/192/2/18

Kong, D., Kaplinghat, M., Yu, H.-B., Fraternali, F., & Mancera Piña, P. E. 2022, The Astrophysical Journal, 936, 166, doi: 10.3847/1538-4357/ac8875

Koposov, S. E., et al. 2011, Astrophys. J., 736, 146, doi: 10.1088/0004-637X/736/2/146

Koudmani, S., Rennehan, D., Somerville, R. S., et al. 2025, Monthly Notices of the Royal Astronomical Society, 540, 1928–1950, doi: 10.1093/mnras/staf778

Kummer, J., Kahlhoefer, F., & Schmidt-Hoberg, K. 2017, Monthly Notices of the Royal Astronomical Society, 474, 388–399, doi: 10.1093/mnras/stx2715

Kuzio de Naray, R., & McGaugh, S. S. 2014, The Astrophysical Journal, 782, L12, doi: 10.1088/2041-8205/782/1/l12

Larson, R. B. 1970, Monthly Notices of the Royal Astronomical Society, 147, 323, doi: 10.1093/mnras/147.4.323

Lelli, F., McGaugh, S. S., & Schombert, J. M. 2016, The Astronomical Journal, 152, 157, doi: 10.3847/0004-6256/152/6/157

Li, J. C.-H. 2016, Behavior Research Methods, 48, 1560

Libeskind, N. I., Carlesi, E., Grand, R. J. J., et al. 2020, Monthly Notices of the Royal Astronomical Society, 498, 2968–2983, doi: 10.1093/mnras/staa2541

Lightman, A. P., & Shapiro, S. L. 1978, Rev. Mod. Phys., 50, 437, doi: 10.1103/RevModPhys.50.437

Loeb, A., & Weiner, N. 2011, Physical Review Letters, 106, doi: 10.1103/physrevlett.106.171302

Lovell, M. R., Gonzalez-Perez, V., Bose, S., et al. 2017, Mon. Not. Roy. Astron. Soc., 468, 2836, doi: 10.1093/mnras/stx621

Lynden-Bell, D., & Eggleton, P. P. 1980, Monthly Notices of the Royal Astronomical Society, 191, 483, doi: 10.1093/mnras/191.3.483

Lynden-Bell, D., & Wood, R. 1968, Monthly Notices of the Royal Astronomical Society, 138, 495, doi: 10.1093/mnras/138.4.495

Mace, C., Zeng, Z. C., Peter, A. H. G., et al. 2024, Phys. Rev. D, 110, 123024, doi: 10.1103/PhysRevD.110.123024

Manwadkar, V., & Kravtsov, A. 2021, Forward-modelling the Luminosity, Distance, and Size distributions of the Milky Way Satellites, arXiv, doi: 10.48550/ARXIV.2112.04511

Martinez, G. D., Bullock, J. S., Kaplinghat, M., Strigari, L. E., & Trotta, R. 2009, JCAP, 0906, 014, doi: 10.1088/1475-7516/2009/06/014

Marx, J., & Cummings, K. 2007, Am. J. Phys., 75, 87

McConnachie, A. W. 2012, Astron. J., 144, 4, doi: 10.1088/0004-6256/144/1/4

McConnachie, A. W., & Côté, P. 2010, The Astrophysical Journal, 722, L209–L214, doi: 10.1088/2041-8205/722/2/l209

Meneghetti, M., Yoshida, N., Bartelmann, M., et al. 2001, Monthly Notices of the Royal Astronomical Society, 325, 435–442, doi: 10.1046/j.1365-8711.2001.04477.x

Miller, K., Espinosa, T., Araujo, I., & Gallegos, I. 2023, Phys. Rev. Phys. Educ. Res., 19, 020167, doi: 10.1103/PhysRevPhysEducRes.19.020167

Minor, Q. E. 2013, The Astrophysical Journal, 779, 116, doi: 10.1088/0004-637x/779/2/116

Minor, Q. E., Martinez, G., Bullock, J., Kaplinghat, M., & Trainor, R. 2010, The Astrophysical Journal, 721, 1142–1157, doi: 10.1088/0004-637x/721/2/1142

Miralda-Escude, J. 2002, The Astrophysical Journal, 564, 60–64, doi: 10.1086/324138

Moore, B. 1994, , 370, 629, doi: 10.1038/370629a0

Moore, B., Ghigna, S., Governato, F., et al. 1999, Astrophys. J., 524, L19, doi: 10.1086/312287

More, S., Diemer, B., & Kravtsov, A. V. 2015, The Astrophysical Journal, 810, 36, doi: 10.1088/0004-637x/810/1/36

Mulvey, P. J., & Nicholson, S. 2020, Physics Bachelor's Degrees: 2018, AIP Statistical Research Center. https://www.aip.org/statistics/reports/physics-bachelors-degrees-2018

Muñoz, R. R., Côté, P., Santana, F. A., et al. 2018, The Astrophysical Journal, 860, 66, doi: 10.3847/1538-4357/aac16b

Nadler, E. O., Banerjee, A., Adhikari, S., Mao, Y.-Y., & Wechsler, R. H. 2020a, Astrophys. J., 896, 112, doi: 10.3847/1538-4357/ab94b0

—. 2021, The Astrophysical Journal Letters, 920, L11, doi: 10.3847/2041-8213/ac29c1

Nadler, E. O., Kong, D., Yang, D., & Yu, H.-B. 2025, SIDM Concerto: Compilation and Data Release of Self-interacting Dark Matter Zoom-in Simulations. https://arxiv.org/abs/2503.10748

Nadler, E. O., Yang, D., & Yu, H.-B. 2023, The Astrophysical Journal Letters, 958, L39, doi: 10.3847/2041-8213/ad0e09

Nadler, E. O., Wechsler, R. H., Bechtol, K., et al. 2020b, The Astrophysical Journal, 893, 48, doi: 10.3847/1538-4357/ab846a

Natarajan, P., Williams, L. L., Bradac, M., et al. 2024, Strong Lensing by Galaxy Clusters. https://arxiv.org/abs/2403.06245

National Academies of Sciences, Engineering, and Medicine. 2022, Origins, Worlds, and Life: A Decadal Strategy for Planetary Science and Astrobiology 2023-2032 (Washington, DC: The National Academies Press), doi: 10.17226/26522

National Center for Science and Engineering Statistics (NCSES). 2023, Diversity and STEM: Women, Minorities, and Persons with Disabilities 2023, National Science Foundation. https://ncses.nsf.gov/pubs/nsf23315/report

National Research Council. 2009, Learning Science in Informal Environments: People, Places, and Pursuits (Washington, DC: The National Academies Press), doi: 10.17226/12190

Navarro, J. F., Eke, V. R., & Frenk, C. S. 1996a, Monthly Notices of the Royal Astronomical Society, 283, L72–L78, doi: 10.1093/mnras/283.3.l72

Navarro, J. F., Frenk, C. S., & White, S. D. M. 1996b, The Astrophysical Journal, 462, 563, doi: 10.1086/177173

—. 1997, Astrophys. J., 490, 493, doi: 10.1086/304888

Nelson, D., Springel, V., Pillepich, A., et al. 2019, Computational Astrophysics and Cosmology, 6, 2, doi: 10.1186/s40668-019-0028-x

Nishikawa, H., Boddy, K. K., & Kaplinghat, M. 2020, Phys. Rev. D, 101, 063009, doi: 10.1103/PhysRevD.101.063009

Noam, G. G., Allen, P. J., Sonnert, G., & Sadler, P. M. 2020, International Journal of Science Education, Part B, 10, 295 . https://api.semanticscholar.org/CorpusID:229305804

Ocvirk, P., Gillet, N., Shapiro, P. R., et al. 2016, Monthly Notices of the Royal Astronomical Society, 463, 1462–1485, doi: 10.1093/mnras/stw2036

Oh, S.-H., Brook, C., Governato, F., et al. 2011, The Astronomical Journal, 142, 24, doi: 10.1088/0004-6256/142/1/24

Okamoto, T., Gao, L., & Theuns, T. 2008, Monthly Notices of the Royal Astronomical Society, 390, 920–928, doi: 10.1111/j.1365-2966.2008.13830.x

Oman, K. A., et al. 2015, Mon. Not. Roy. Astron. Soc., 452, 3650, doi: 10.1093/mnras/stv1504

Onorbe, J., Garrison-Kimmel, S., Maller, A. H., et al. 2013, Monthly Notices of the Royal Astronomical Society, 437, 1894–1908, doi: 10.1093/mnras/stt2020

Outmezguine, N. J., Boddy, K. K., Gad-Nasr, S., Kaplinghat, M., & Sagunski, L. 2023, Monthly Notices of the Royal Astronomical Society, 523, 4786–4800, doi: 10.1093/mnras/stad1705

Oñorbe, J., Boylan-Kolchin, M., Bullock, J. S., et al. 2015, Monthly Notices of the Royal Astronomical Society, 454, 2092–2106, doi: 10.1093/mnras/stv2072

Palubski, I., Slone, O., Kaplinghat, M., Lisanti, M., & Jiang, F. 2024, Numerical Challenges in Modeling Gravothermal Collapse in Self-Interacting Dark Matter Halos. https://arxiv.org/abs/2402.12452

Patel, E., Kallivayalil, N., Garavito-Camargo, N., et al. 2020, The Astrophysical Journal, 893, 121, doi: 10.3847/1538-4357/ab7b75

Percival, W. J., Nichol, R. C., Eisenstein, D. J., et al. 2007, , 657, 645, doi: 10.1086/510615

Peter, A. H. G., Rocha, M., Bullock, J. S., & Kaplinghat, M. 2013, Monthly Notices of the Royal Astronomical Society, 430, 105–120, doi: 10.1093/mnras/sts535

Planck Collaboration, Ade, P. A. R., Aghanim, N., et al. 2016, A&A, 594, A13, doi: 10.1051/0004-6361/201525830

Pontzen, A., & Governato, F. 2012, , 421, 3464, doi: 10.1111/j.1365-2966.2012.20571.x

Porter, A. M., & Ivie, R. 2019, AIP Statistics Report

Power, C., Navarro, J. F., Jenkins, A., et al. 2003, , 338, 14, doi: 10.1046/j.1365-8711.2003.05925.x

Ragagnin, A., Meneghetti, M., Calura, F., et al. 2024, Astronomy amp; Astrophysics, 687, A270, doi: 10.1051/0004-6361/202449872

Rakow, S. 2009, National Association for Gifted Children. http://www.education.com

Read, J. I., & Gilmore, G. 2005, Monthly Notices of the Royal Astronomical Society, 356, 107–124, doi: 10.1111/j.1365-2966.2004.08424.x

Read, J. I., Walker, M. G., & Steger, P. 2018, Mon. Not. Roy. Astron. Soc., 481, 860, doi: 10.1093/mnras/sty2286

—. 2019, Mon. Not. Roy. Astron. Soc., 484, 1401, doi: 10.1093/mnras/sty3404

Relatores, N. C., Newman, A. B., Simon, J. D., et al. 2019, The Astrophysical Journal, 887, 94, doi: 10.3847/1538-4357/ab5305

Ren, T., Kwa, A., Kaplinghat, M., & Yu, H.-B. 2019, Phys. Rev. X, 9, 031020, doi: 10.1103/PhysRevX.9.031020

Robertson, A., Harvey, D., Massey, R., et al. 2019, Monthly Notices of the Royal Astronomical Society, 488, 3646–3662, doi: 10.1093/mnras/stz1815

Robertson, A., Massey, R., & Eke, V. 2017, Monthly Notices of the Royal Astronomical Society, 467, 4719–4730, doi: 10.1093/mnras/stx463

Robertson, A., Massey, R., Eke, V., Schaye, J., & Theuns, T. 2020, Monthly Notices of the Royal Astronomical Society, 501, 4610–4634, doi: 10.1093/mnras/staa3954

Robertson, B., Bullock, J. S., Cox, T. J., et al. 2006, The Astrophysical Journal, 645, 986–1000, doi: 10.1086/504412

Robles, V. H., & Bullock, J. S. 2021, Monthly Notices of the Royal Astronomical Society, 503, 5232, doi: 10.1093/mnras/stab829

Robles, V. H., Kelley, T., Bullock, J. S., & Kaplinghat, M. 2019, Mon. Not. Roy. Astron. Soc., 490, 2117, doi: 10.1093/mnras/stz2345

Robles, V. H., Bullock, J. S., Elbert, O. D., et al. 2017, Monthly Notices of the Royal Astronomical Society, 472, 2945–2954, doi: 10.1093/mnras/stx2253

Rocha, M., Peter, A. H. G., Bullock, J. S., et al. 2013, Mon. Not. Roy. Astron. Soc., 430, 81, doi: 10.1093/mnras/sts514

Rubin, V. C., & Ford, Jr., W. K. 1970, The Astrophysical Journal, 159, 379, doi: 10.1086/150317

Rudolph, A., Gonzaga, V., Prather, E., Brissenden, G., & Consiglio, D. 2010, Astronomy Education Review, 9, 010107

Ruscio, J. 2008, Psychological Methods, 13, 19, doi: 10.1037/1082-989X.13.1.19.PMID:18331151

Sales, L. V., Wetzel, A., & Fattahi, A. 2022, Nature Astronomy, 6, 897, doi: 10.1038/s41550-022-01689-w

Sameie, O., Chakrabarti, S., Yu, H.-B., et al. 2020a, Simulating the "hidden giant" in cold and self-interacting dark matter models, arXiv. https://arxiv.org/abs/2006.06681

Sameie, O., Creasey, P., Yu, H.-B., et al. 2018, Mon. Not. Roy. Astron. Soc., 479, 359, doi: 10.1093/mnras/sty1516

Sameie, O., Yu, H.-B., Sales, L. V., Vogelsberger, M., & Zavala, J. 2020b, Phys. Rev. Lett., 124, 141102, doi: 10.1103/PhysRevLett.124.141102

Sameie, O., Boylan-Kolchin, M., Sanderson, R., et al. 2021, Monthly Notices of the Royal Astronomical Society, 507, 720, doi: 10.1093/mnras/stab2173

Samuel, J., Wetzel, A., Tollerud, E., et al. 2019, Monthly Notices of the Royal Astronomical Society, 491, 1471–1490, doi: 10.1093/mnras/stz3054

Sands, I. S., Hopkins, P. F., Shen, X., et al. 2024, Confronting the Diversity Problem: The Limits of Galaxy Rotation Curves as a tool to Understand Dark Matter Profiles. https://arxiv.org/abs/2404.16247

Santos-Santos, I. M., Di Cintio, A., Brook, C. B., et al. 2018, , 473, 4392, doi: 10.1093/mnras/stx2660

Santos-Santos, I. M. E., Navarro, J. F., Robertson, A., et al. 2020, Monthly Notices of the Royal Astronomical Society, 495, 58–77, doi: 10.1093/mnras/staa1072

Sawala, T., Guo, Q., Scannapieco, C., Jenkins, A., & White, S. 2011, Monthly Notices of the Royal Astronomical Society, 413, 659–668, doi: 10.1111/j.1365-2966.2010.18163.x

Sawala, T., Scannapieco, C., Maio, U., & White, S. 2010, Monthly Notices of the Royal Astronomical Society, 402, 1599, doi: 10.1111/j.1365-2966.2009.16035.x

Sawala, T., Frenk, C. S., Fattahi, A., et al. 2015, Monthly Notices of the Royal Astronomical Society, 456, 85–97, doi: 10.1093/mnras/stv2597

Schutz, K., & Slatyer, T. R. 2015, Journal of Cosmology and Astroparticle Physics, 2015, 021–021, doi: 10.1088/1475-7516/2015/01/021

Shapiro, S. L., & Teukolsky, S. A. 1985, , 292, L41, doi: 10.1086/184469

Shen, X., Hopkins, P. F., Necib, L., et al. 2021, Monthly Notices of the Royal Astronomical Society, 506, 4421–4445, doi: 10.1093/mnras/stab2042

—. 2024, The Astrophysical Journal, 966, 131, doi: 10.3847/1538-4357/ad2fb1

Simon, J. D. 2019, Annual Review of Astronomy and Astrophysics, 57, 375–415, doi: 10.1146/annurev-astro-091918-104453

Simpson, C. M., Grand, R. J. J., Gómez, F. A., et al. 2018, Monthly Notices of the Royal Astronomical Society, 478, 548–567, doi: 10.1093/mnras/sty774

Slone, O., Jiang, F., Lisanti, M., & Kaplinghat, M. 2023, Phys. Rev. D, 107, 043014, doi: 10.1103/PhysRevD.107.043014

Somerville, R. S. 2002, The Astrophysical Journal, 572, L23–L26, doi: 10.1086/341444

Sparre, M., & Springel, V. 2017, Monthly Notices of the Royal Astronomical Society, 470, 3946–3958, doi: 10.1093/mnras/stx1516

Spencer, M. E., Mateo, M., Walker, M. G., et al. 2017, The Astronomical Journal, 153, 254, doi: 10.3847/1538-3881/aa6d51

Spergel, D. N., & Steinhardt, P. J. 2000, Phys. Rev. Lett., 84, 3760, doi: 10.1103/PhysRevLett.84.3760

Springel, V. 2005, Monthly Notices of the Royal Astronomical Society, 364, 1105–1134, doi: 10.1111/j.1365-2966.2005.09655.x

Springel, V., Frenk, C. S., & White, S. D. M. 2006, , 440, 1137, doi: 10.1038/nature04805

Springel, V., Wang, J., Vogelsberger, M., et al. 2008, Mon. Not. Roy. Astron. Soc., 391, 1685, doi: 10.1111/j.1365-2966.2008.14066.x

Tegmark, M., Blanton, M. R., Strauss, M. A., et al. 2004, The Astrophysical Journal, 606, 702–740, doi: 10.1086/382125

The AIP National Task Force to Elevate the Representation of African Americans in Undergraduate Physics and Astronomy (TEAM-UP). 2020, The Time Is Now: Systemic Changes to Increase African Americans with Bachelor's Degrees in Physics and Astronomy (The American Institute of Physics). https://www.aip.org/sites/default/files/aipcorp/files/teamup-full-report.pdf

The American Institute of Physics. 2022, The Number of Doctorates Earned in Physics, 2014-15 to 2018-19. https://www.aip.org/statistics/resources/number-doctorates-earned-physics-2014-15-2018-19

Thoul, A. A., & Weinberg, D. H. 1996, The Astrophysical Journal, 465, 608, doi: 10.1086/177446

Torrealba, G., Belokurov, V., Koposov, S. E., et al. 2019, Monthly Notices of the Royal Astronomical Society, 488, 2743–2766, doi: 10.1093/mnras/stz1624

Tulin, S., & Yu, H.-B. 2018, Physics Reports, 730, 1–57, doi: 10.1016/j.physrep.2017.11.004

Tulin, S., Yu, H.-B., & Zurek, K. M. 2013, Physical Review D, 87, doi: 10.1103/physrevd.87.115007

Turner, H. C., Lovell, M. R., Zavala, J., & Vogelsberger, M. 2021, Monthly Notices of the Royal Astronomical Society, 505, 5327–5339, doi: 10.1093/mnras/stab1725

Valli, M., & Yu, H.-B. 2018, Nat. Astron., 2, 907, doi: 10.1038/s41550-018-0560-7

van den Bosch, F. C., & Ogiya, G. 2018, Monthly Notices of the Royal Astronomical Society, 475, 4066–4087, doi: 10.1093/mnras/sty084

Vargya, D., Sanderson, R., Sameie, O., et al. 2021, Shapes of Milky-Way-Mass Galaxies with Self-Interacting Dark Matter, arXiv, doi: 10.48550/ARXIV.2104.14069

Vogelsberger, M., Zavala, J., & Loeb, A. 2012, Mon. Not. Roy. Astron. Soc., 423, 3740, doi: 10.1111/j.1365-2966.2012.21182.x

Vogelsberger, M., Zavala, J., Simpson, C., & Jenkins, A. 2014, Monthly Notices of the Royal Astronomical Society, 444, 3684–3698, doi: 10.1093/mnras/stu1713

Wang, L., Xu, D., Gao, L., et al. 2019, Monthly Notices of the Royal Astronomical Society, 485, 2083–2091, doi: 10.1093/mnras/stz529

Weir, K. 2007, Spectrum, 35. http://csma.aas.org/spectrum.html

Wetzel, A., Hayward, C. C., Sanderson, R. E., et al. 2023, The Astrophysical Journal Supplement Series, 265, 44, doi: 10.3847/1538-4365/acb99a

Wetzel, A. R., Hopkins, P. F., Kim, J.-h., et al. 2016, The Astrophysical Journal, Letters, 827, L23, doi: 10.3847/2041-8205/827/2/L23

Wheeler, C., Hopkins, P. F., Pace, A. B., et al. 2019, Monthly Notices of the Royal Astronomical Society, 490, 4447–4463, doi: 10.1093/mnras/stz2887

Wolf, J., Martinez, G. D., Bullock, J. S., et al. 2010, Mon. Not. Roy. Astron. Soc., 406, 1220, doi: 10.1111/j.1365-2966.2010.16753.x

Wulf, R., Hinko, K., & Finkelstein, N. 2013, AIP Conference Proceedings, 1513, 430, doi: 10.1063/1.4789744

Yang, D., Nadler, E. O., & Yu, H.-B. 2023a, The Astrophysical Journal, 949, 67, doi: 10.3847/1538-4357/acc73e

—. 2025, Physics of the Dark Universe, 47, 101807, doi: 10.1016/j.dark.2025.101807

Yang, D., Nadler, E. O., Yu, H.-B., & Zhong, Y.-M. 2024, Journal of Cosmology and Astroparticle Physics, 2024, 032, doi: 10.1088/1475-7516/2024/02/032

Yang, D., & Yu, H.-B. 2022, Journal of Cosmology and Astroparticle Physics, 2022, 077, doi: 10.1088/1475-7516/2022/09/077

Yang, S., Du, X., Zeng, Z. C., et al. 2023b, The Astrophysical Journal, 946, 47, doi: 10.3847/1538-4357/acbd49

Yukawa, H. 1955, Progress of Theoretical Physics Supplement, 1, 1, doi: 10.1143/PTPS.1.1

Zavala, J., Lovell, M. R., Vogelsberger, M., & Burger, J. D. 2019, Physical Review D, 100, doi: 10.1103/physrevd.100.063007

Zavala, J., Vogelsberger, M., & Walker, M. G. 2013, Mon. Not. Roy. Astron. Soc., 431, L20, doi: 10.1093/mnrasl/sls053

Zel'dovich, Y. B., & Podurets, M. A. 1966, , 9, 742

Zeng, Z. C., Peter, A. H. G., Du, X., et al. 2021, Core-collapse, evaporation and tidal effects: the life story of a self-interacting dark matter subhalo. https://arxiv.org/abs/2110.00259

Zhang, X., Yu, H.-B., Yang, D., & An, H. 2024, The Astrophysical Journal Letters, 968, L13, doi: 10.3847/2041-8213/ad50cd

Zwicky, F. 1933, Helvetica Physica Acta, 6, 110. https://ui.adsabs.harvard.edu/abs/1933AcHPh...6..110Z

—. 1937, The Astrophysical Journal, 86, 217, doi: 10.1086/143864

Appendix A

List of Variables and Abbreviations

The variables used throughout this thesis are defined in Table A.1. The abbreviations used throughout this work are listed below.

- DM: Dark matter
- SM: Standard model
- CDM: Cold dark matter
- CMB: Cosmic Microwave Background
- SIDM: Self-interacting dark matter
- vdSIDM: velocity-dependent self-interacting dark matter
- NFW: Navarro-Frenk-White
- SPARC: Spitzer Photometry and Accurate Rotation Curves
- MW: Milky Way Galaxy
- dSphs: dwarf spheroidal galaxies

- TBTF: Too-big-to-fail
- MS: Missing satellites
- DMO: Dark matter-only

Variable	Description
σ/m	Cross-section: DM self-interaction cross-section over the DM particle mass.
V_{circ}	Circular velocity: calculated according to Newtonian dynamics.
V_{max}	Time evolving maximum circular velocity as a function of radius.
R_{max}	Radius at which V_{circ} reaches V_{max}.
r_{vir}	Virial radius: radius that encloses a density that is 200 times the background matter density.
M_{host}	Host mass: mass within r_{vir} that is gravitationally bound to the host halo.
m_{sub}	Subhalo mass: mass within r_{vir} that is gravitationally bound to the subhalo.
V_{tan}	Tangential velocity: magnitude of the velocity of a subhalo tangential to the host halo.
V_{tot}	Total velocity: magnitude of the velocity of the subhalo with respect to the host halo.
t_{infall}	Infall time: time when subhalo first falls into host halo r_{vir}. Exact infall time is calculated as the intersection between the linear interpolated subhalo-host distance and the time evolving host r_{vir}. Quantities at infall are calculated using the snapshot after the interpolated infall time.
ρ_c	Core density: the core density of a cored density profile (equation 7.1) fit to the inner region of each halo.
r_{core}	Core radius: radius where the isothermal density profile falls to $\rho_c/2$.
r_0	Characteristic radius: radius at which the slope of the log density profile becomes -3.
v_c	Core velocity dispersion: average velocity dispersion within r_{core}.
$\rho_{c,0}$	Minimum ρ_c across time.
t_{core}	Time of $\rho_{c,0}$.
$r_{core,0}$	Maximum core radius: r_{core} at t_{core}.
$v_{c,0}$	Core 1D velocity dispersion at t_{core}.

Table A.1: Definition of variables used throughout this work.